Power Transfer by Near-Field Coupling

Dominik Huwig

© Dominik Huwig

dominik.huwig@etatronix.de

Master's thesis (German original) of September 30, 2013
Energieübertragung durch Nahfeldkopplung

Revised and abridged edition, English translation of November 25, 2026

Abstract

The number of developments and publications on power transfer by near-field coupling has risen significantly in recent years. The focus is increasingly on inductive transfer, often with very different designs and circuit topologies. As a result, analytical approaches are becoming ever more specialized, and alternative transfer methods receive less attention.

This thesis treats the transmission system in general form, independent of the type of coupling, and focuses on the essentials: transferring high power at maximum efficiency. The characteristic quantities derived for this purpose make it possible to characterize a wide variety of transmission systems and to quantify their transfer quality, which allows an objective comparison of very different transfer methods.

Since transferring high power at maximum efficiency imposes requirements on the connected load impedance and on the source, the thesis shows how matching networks can meet these requirements. Thus, in addition to characterizing the transmission system, it presents a way to implement it in practice.

Contents

Notation **7**

1 Introduction **11**

2 Fundamentals **15**

3 Transmission Systems **22**
3.1 Power Extraction . . . 24
3.1.1 Transfer Quality Factor . . . 28
3.1.2 Transfer Bandwidth . . . 30
3.2 Power Injection . . . 33
3.2.1 Transfer Functions . . . 33
3.2.2 Voltage Feed . . . 35
3.2.3 Current Feed . . . 36
3.3 Equivalent Circuits . . . 37
3.3.1 Transformer-Based Equivalent Circuits . . . 37
Complex Transformer . . . 38
Equivalent Circuits . . . 40
3.3.2 Gyrator-Based Equivalent Circuit . . . 42
Complex Gyrator . . . 43
Equivalent Circuit . . . 44
3.4 Application Examples . . . 46
3.4.1 Example Systems . . . 46
3.4.2 Multi-Coil System . . . 48

4 Matching **51**
4.1 Transmission System Matching . . . 52
4.1.1 Voltage Feed . . . 52
4.1.2 Current Feed . . . 55
4.2 Load Matching . . . 57
4.2.1 Transformer-Based Series Load Matching . . . 58
4.2.2 Gyrator-Based Series Load Matching . . . 59
4.2.3 Transformer-Based Parallel Load Matching . . . 61

4.2.4 Gyrator-Based Parallel Load Matching . . . 63
4.3 Source Matching . . . 64
4.3.1 Transformer-Based Voltage Feed . . . 65
4.3.2 Gyrator-Based Voltage Feed . . . 66
4.3.3 Transformer-Based Current Feed . . . 68
4.3.4 Gyrator-Based Current Feed . . . 69
4.4 Transfer Quality Factor and Transfer Bandwidth . . . 71
4.5 Application Examples . . . 73
4.5.1 Transmission System Matching . . . 74
4.5.2 Load Matching . . . 75
4.5.3 Source Matching . . . 77
4.5.4 Multi-Coil System . . . 79

5 Summary and Outlook **83**

Appendix

A Example Systems **87**
A.1 Inductive System . . . 88
A.1.1 Magnetic Vector Field of a Concentric Conductor Loop . . . 89
A.1.2 Magnetic Coupling . . . 94
A.1.3 Losses . . . 98
A.1.4 Impedance Matrix . . . 98
A.2 Capacitive System . . . 101
A.2.1 Coupling Capacitors . . . 102
A.2.2 Leakage Capacitors . . . 103
Surface Leakage Capacitor . . . 105
Lateral Leakage Capacitor . . . 108
A.2.3 Losses . . . 113
A.2.4 Impedance Matrix . . . 114

B Two-Port Parameters **117**
B.1 Measurement of the Two-Port Parameters . . . 120
B.2 Synthesis of the Reciprocal System Matrix . . . 122
B.2.1 T Network . . . 122
B.2.2 Π Network . . . 122

List of Figures **125**

Bibliography **128**

Notation

Mathematical Notation

Notation	Meaning
x	Real quantity
$\boldsymbol{x}$	Complex quantity or complex amplitude
$\boldsymbol{x}^*$	Complex conjugate of $\boldsymbol{x}$
$\mathrm{Re}\,\boldsymbol{x}$	Real part of $\boldsymbol{x}$
$\mathrm{Im}\,\boldsymbol{x}$	Imaginary part of $\boldsymbol{x}$
$\lvert\boldsymbol{x}\rvert$	Magnitude of $\boldsymbol{x}$
φ_x	Phase of $\boldsymbol{x}$
x_a	Quantity with attribute or position a
x'_a	Upstream or opposing quantity with respect to x_a
x_{ab}	Quantity occurring at a but caused by b
$\vec{x}$	Vector with three components
$\mathcal{X}$	Matrix $\mathcal{X}$
$\mathcal{X}_{ab}$	System matrix between a and b
$x_{a,b}$	Element of matrix $\mathcal{X}$ in row a and column b
$\det\mathcal{X}$	Determinant of matrix $\mathcal{X}$
$\mathbb{X}$	Mathematical set
j	Imaginary unit, $\sqrt{-1}$
$\vec{x} \times \vec{y}$	Cross product of $\vec{x}$ and $\vec{y}$
$\vec{x} \circ \vec{y}$	Dot product of $\vec{x}$ and $\vec{y}$

Symbols

Symbol	Unit	Description
A	m^2	Surface area
a	m	Distance between two electrodes
$\mathcal{A}$	–	Chain (ABCD) matrix
B	T, $\frac{\mathrm{V\,s}}{\mathrm{m}^2}$	Magnetic flux density
B_k	–	Transfer bandwidth
C	F, $\frac{\mathrm{A\,s}}{\mathrm{V}}$	Capacitance
d	m	Diameter
DF	–	Dissipation factor
E	$\frac{\mathrm{V}}{\mathrm{m}}$	Electric field strength
ESR	Ω	Equivalent series resistance
f	Hz	Frequency of an alternating quantity
FOM	–	Figure of merit, $FOM = \sqrt{Q_k^2 - 1}$
g	m	Distance between transmitter and receiver
H	–	Transfer function
$\mathcal{H}$	–	Hessian matrix
I	A	Electric current
k	–	Coupling factor
L	H, $\frac{\mathrm{V\,s}}{\mathrm{A}}$	Inductance
l	m	Current-carrying conductor
M	H, $\frac{\mathrm{V\,s}}{\mathrm{A}}$	Mutual inductance
n	–	Turns ratio of a transformer
P	W	Active power
Q	–	Quality factor
Q_k	–	Transfer quality factor
r	m	Radius
R	Ω	Resistance, real part of $\boldsymbol{Z}$
R	m	Distance between two points
R_G	Ω	Gyration resistance
S	V A	Apparent power

t	s	Time
V	V	Voltage or potential difference
x	–	General auxiliary variable
X	Ω	Reactance, imaginary part of $\boldsymbol{Z}$
$\boldsymbol{Y}$	S	Complex admittance, $Y = \frac{1}{Z}$
$\mathcal{Y}$	S	Admittance matrix
$\boldsymbol{Z}$	Ω	Complex impedance
Z_G	Ω	Gyration impedance of the complex gyrator
$\mathcal{Z}$	Ω	Impedance matrix
α	Ω	Auxiliary variable for system description
β	Ω	Auxiliary variable for system description
ϵ_0	$\frac{\mathrm{A\,s}}{\mathrm{V\,m}}$	Vacuum permittivity, $\epsilon_0 \approx 8.8542 \times 10^{-12}$
ϵ_r	–	Relative permittivity
γ	Ω	Auxiliary variable for system description
η	–	Efficiency
κ	–	See coupling factor k
λ	–	Power factor
μ_0	$\frac{\mathrm{V\,s}}{\mathrm{A\,m}}$	Vacuum permeability, $\mu_0 = 4\pi \times 10^{-7}$
μ_r	–	Relative permeability
ϕ	V	Potential or potential function
ω	rad/s	Angular frequency of an alternating quantity, $\omega = 2\pi f$
χ	–	See FOM
ψ	A	Stream function

1. Introduction

At the beginning of electrification, from 1884 to 1896, the companies *Westinghouse Electric*, founded by George Westinghouse (* 1846, † 1914), and *Edison General Electric*, founded by Thomas Alva Edison (* 1847, † 1931), were engaged in a dispute over the best way to distribute electrical power through wired networks [1]. Edison favored local power plants supplying nearby areas with direct current, whereas Westinghouse favored alternating current because it could easily be transformed. Not least thanks to the involvement of Nikola Tesla (* 1856, † 1943), *Westinghouse Electric* and the distribution of power via an alternating-current grid prevailed.

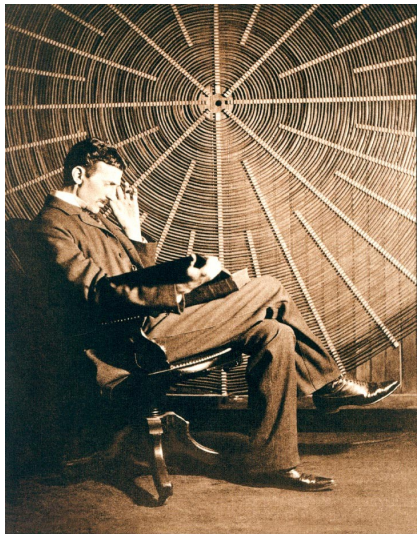

Figure 1.1.: *Nikola Tesla in front of a coil, photographer unknown (public domain),*
image source: www.teslasociety.com

Since expanding the wired power supply involved considerable effort and cost, Nikola Tesla, presumably inspired by Guglielmo Marconi's (* 1874 , † 1937) wireless signal transmission in 1896 [2], soon turned to the idea of transmitting energy without contacts or wires as well. Tesla filed his first patent on wireless power transmission as early as 1900 [3]. In 1905, he filed for a method which, in his opinion, should make it possible to transmit both data and electrical energy wirelessly to large parts of the

earth [4]. Between these two filings, the Wardenclyffe Tower [5, 6] was built, a large Tesla transformer on Long Island (USA) intended to enable wireless power distribution. Due to technical difficulties and a lack of funding, however, the facility was never completed. Nevertheless, the first work on and visions of contactless power transfer go back to Nikola Tesla.

After Tesla's unsuccessful attempt to introduce it, wireless power transfer was pursued and applied only sporadically in highly specialized fields. In 1958, for example, the first fully implantable pacemaker was used; because of the low capacity of the batteries available at the time, it could already be charged inductively from outside the body [7]. As industrial automation advanced, however, interest in wireless power transfer grew again toward the end of the 20th century. The aim was to replace maintenance-intensive slip rings and to power automated guided vehicles.

Driven by the ongoing miniaturization of electrical engineering and mechanics, the number of implantable medical assist devices, mobile communication devices, and consumer electronics is growing very rapidly today. At the same time, electromobility is becoming increasingly important. With contactless power transfer entering these lucrative markets, current market research expects the market volume of wireless power transfer to grow to 15 billion US dollars as early as 2020 [8].

Contactless power transfer can be divided into two basic methods: power transfer in the near field and power transfer in the far field [6, 9]. In the far field, energy is transferred by propagating waves. In many cases these are electromagnetic waves [10], although acoustic waves are also used for power transfer [11]. To increase efficiency, the waves must be strongly focused into a beam. Such a beam requires an unobstructed path between transmitter and receiver and, in addition, a very precise alignment of the transmitting and receiving units. One example is the power supply of aircraft by a steerable laser beam sent from the ground [12, 13, 14]. Another example is the idea, conceived by Peter Edward Glaser as early as 1968, of collecting energy outside the earth's atmosphere with solar collectors and transporting it to earth via a directed microwave beam [15, 16]. The advantage of directed electromagnetic power transfer in the far field is that the range is limited only by attenuation in the propagation medium, so that very long distances can be bridged in air or even in vacuum.

If efficiency, i.e., the ratio of received to transmitted active power, is of secondary importance, the energy does not need to be focused into a beam at the transmitter. This makes it possible, for example, to supply very-low-power receivers over a wide area. High-frequency RFID variants are an example of this. [17] presents such a system for patient monitoring in a care environment.

Far-field transfer methods always have the disadvantage that either the waves must be focused into a beam or the efficiency of the power transfer remains very low. Near-field coupling avoids this trade-off. Here, the energy is transferred directly in the electric

[18, 19] or magnetic [20, 21, 22] field. Ideally, no electromagnetic wave propagates. However, since the receiver is fed directly by the field generated by the transmitter, the distances that can be bridged are severely limited compared to far-field transfer. On the other hand, high efficiency can be achieved even without precise alignment of transmitter and receiver.

Most of the systems available today transfer energy in the near field, predominantly by inductive transfer. The growing number of these systems, especially in the consumer market, has created a demand for interoperability between manufacturers. In the future, it should be possible to supply or charge a wide variety of power receivers with a single standardized power transmitter. This demand led to the founding of several consortia, namely the *Wireless Power Consortium (WPC)*, founded in 2009, the *Power Matters Alliance (PMA)*, founded in 2012, and the *Alliance for Wireless Power (A4WP)*, established in the same year [23].

The mobile communications sector is currently a particularly successful market. Many manufacturers now use a standardized inductive near-field transfer method to charge their mobile phones. This eliminates failure-prone charging contacts and connectors while increasing user convenience. As mentioned at the beginning, there are also many interesting and lucrative fields of application in medical technology. For example, implanted assist systems can be supplied with energy transcutaneously. For the patient, the major advantage is that the implant can be powered without cables passing through the skin, which minimizes the risk of infection. Furthermore, many devices and tools in the medical field benefit from wireless power transfer because charging or supply connectors can be omitted entirely. This simplifies disinfection and chemical sterilization, since even electronic devices can be fully immersed in an appropriate solution.

In industrial environments, in addition to replacing slip rings and powering automated guided vehicles, power transfer into closed containers and tanks or to moving and rotating applications is also of interest. At the same time, eliminating electrical contacts rules out contact sparks. This allows wireless devices to be charged or powered even in hazardous (explosion-protected) areas such as mining, refineries, or offshore platforms.

Because of the many possible applications, this thesis deals exclusively with near-field transmission systems. It is assumed that neither the power transmitter nor the power receiver emits electromagnetic waves. This makes it possible to describe a linear time-invariant near-field transmission system by two-port parameters, independent of the type of coupling [24]. The examples shown are inductive and capacitive transmission systems, although this is not meant as a restriction.

This thesis focuses on determining how best to utilize an existing or given transmission system. Additional external circuitry is intended to make it possible both to maximize the efficiency of the power transfer and to transfer as much power as possible. Losses

in the power amplifier or in a rectifier that may be required are neglected. Knowing the optimal operating point of a transmission system makes it possible to characterize very different methods and, among other things, to compare them objectively.

The next chapter provides an initial overview of the fundamentals and practical challenges of near-field transmission systems. Since most of the transmission systems available today transfer energy in the magnetic field, an inductive transmission system is considered here as a representative example. Using selected examples and a lossless representation, it illustrates how high power levels have so far been transferred despite poor magnetic coupling between transmitter and receiver. For this purpose, resonant compensation is introduced.

Chapter 3 describes general transmission systems by two-port parameters and shows what additional information these parameters provide at a given frequency. It determines the load impedance at the output of the transmission system that maximizes the efficiency of the power transfer, as well as the source reactance at the input that maximizes the active power delivered to the output. Simple relationships are then used to show how transmission systems can be characterized by the newly introduced transfer quality factor. This factor indicates the achievable efficiency and also shows how much the connected load resistance may vary while maintaining high efficiency. At the end of the chapter, equivalent circuits of general transmission systems are presented. For this purpose, a complex transformer and a complex gyrator are introduced. The chapter concludes with several application examples.

In practice, the optimal load impedance and source reactance rarely match the actual load and source. Chapter 4 shows how suitable matching can address this. If the transmission system itself can be modified, the first section describes how it should be designed for the connected load resistance and the available source. If the transmission system cannot be modified, the subsequent sections show how additional matching networks at the input and output terminals can be used to match the actual quantities to the optimal ones. Application examples are again given at the end. Some of these matching options were also identified in [25] and [26] while this thesis was being written.

In addition to summarizing the thesis, Chapter 5 gives an outlook on future work. In particular, it discusses the different types of matching from the preceding chapter and a possible control concept.

The appendix presents the theoretical determination of the two-port parameters of an inductive and a capacitive transmission system. For this purpose, the Biot-Savart law, the Schwarz-Christoffel polygon mapping, and conformal mapping are applied. The resulting two-port parameters are used, among other things, in the application examples of the preceding chapters.

2. Fundamentals

Although contactless power transfer remains the focus of many research groups, the number of applications available on the market has been rising steadily for several years. Most of these contactless transmission systems are based on inductive near-field coupling between two or more coils. The number of publications on alternative near-field transfer methods, such as capacitive power transfer, is considerably smaller. Although a few applications based on capacitive coupling are already available on the market, they currently play only a minor role.

Taking inductive systems as representative of near-field transmission systems in general, this section first presents the fundamentals, challenges, and known solutions of contactless inductive power transfer. For simplicity, losses are neglected in this first section. The literature contains several methods for describing near-field transmission systems [27, 28]. Following the terminology of [27], these methods can be divided into three groups. *Coupled-mode theory* describes the transmission system by an approximation in the form of first-order differential equations [29, 30, 31]. In the likewise widespread *reflected load theory*, all components on the output or receiver side are reflected to the input circuit and represented there by a reflected impedance. *Lumped circuit theory*, finally, assumes discrete components. This thesis describes many relationships using *lumped circuit theory* and makes only limited use of *reflected load theory*.

In the lossless case with sinusoidal excitation, inductively coupled coils can be described by the well-known transformer equations

$$\begin{aligned} \boldsymbol{V}_1 &= j\omega L_1 \boldsymbol{I}_1 - j\omega M \boldsymbol{I}_2 \\ \boldsymbol{V}_2 &= j\omega M \boldsymbol{I}_1 - j\omega L_2 \boldsymbol{I}_2 \end{aligned} \tag{2.1}$$

[32]. The voltages $\boldsymbol{V}_1$ and $\boldsymbol{V}_2$ can be measured at the input and output terminals, respectively. The same applies to the currents $\boldsymbol{I}_1$ and $\boldsymbol{I}_2$. L_1 and L_2 are the self-inductances of the respective windings, M is the mutual inductance, and ω is the angular frequency of the excitation.

With the system of equations (2.1) and a resistive load at the output terminals, the equivalent circuit in Figure 2.1 from [22, 33], or, in the more general case, the one in Figure 3.12(b) of this thesis, follows directly. Here, k_X is the reactive coupling factor,

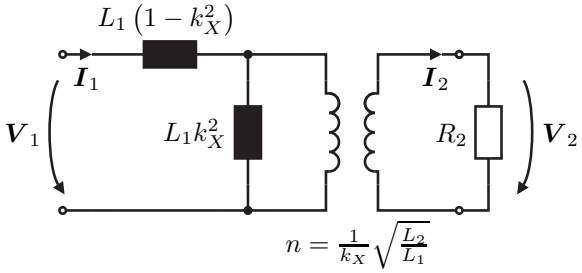

Figure 2.1.: Γ_1 *equivalent circuit of the lossless transformer equations*

which in the case of inductive coupling is given by

$$k_X = \frac{M}{\sqrt{L_1 L_2}}\,. \tag{2.2}$$

This coupling factor depends on the distance and orientation of the transmitting and receiving coils. Its range of values is

$$D \coloneqq \{k_X \in \mathbb{R}\,|\,-1 \leq k_X \leq 1\}\,. \tag{2.3}$$

Because the coupled coils are spatially separated, the magnitude of the reactive coupling factor in practical systems is considerably smaller than 1. Depending on the distance, coupling factors of $|k_X| < 0.1$ can occur. Under these conditions, Figure 2.1 directly shows that, without load, most of the input voltage drops across the inductance $L_1(1-k_X^2)$ and only a small fraction of this voltage is available at the output. The open-circuit voltage therefore decreases with the magnitude of the coupling factor. It is also apparent that, with large load resistances, most of the injected current flows through the inductance $L_1 k_X^2$ rather than, as desired, through the resistor R_2. With small load resistances, the output current is again limited by $L_1(1-k_X^2)$, and the short-circuit current available at the output decreases with the reactive coupling factor.

Besides the decrease in open-circuit voltage and short-circuit current, the equivalent circuit in Figure 2.1 shows that, at a small magnitude of the coupling factor, a many times higher apparent power must be supplied to transfer an active power P_2. The relationship

$$\frac{\boldsymbol{S}_1}{P_2} = 1 + j\frac{1}{k_X^2}\left[\frac{\omega L_2}{R_2}\left(1-k_X^2\right) + \frac{R_2}{\omega L_2}\right] \tag{2.4}$$

holds, according to which the imaginary part of the input apparent power rises sharply as the coupling factor decreases. Figure 2.2 shows the magnitude of (2.4) as a function of the reactive coupling factor and the normalized load resistance R_2. With large coupling factors, the apparent power drawn is generally lower. Furthermore, Figure 2.2 shows that the apparent power drawn by the system varies with the connected load resistance and that, depending on the coupling factor, there is a load resistance at which

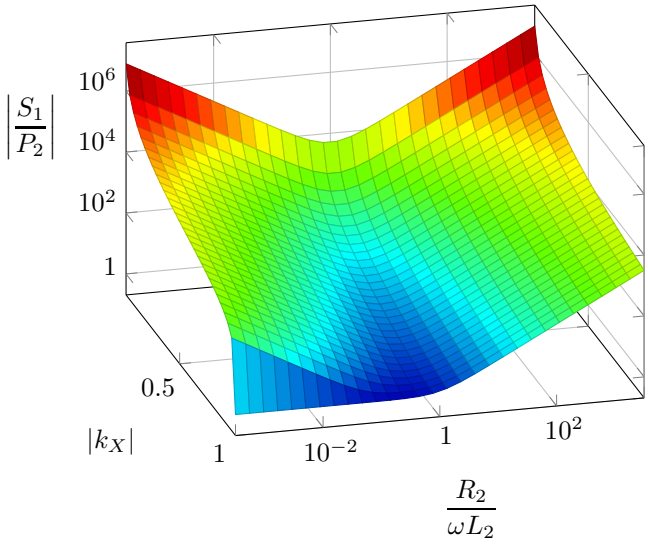

Figure 2.2.: *Normalized magnitude of the input apparent power (2.4) as a function of the coupling factor k_X and the normalized load resistance*

the apparent power drawn reaches a minimum. Differentiating (2.4) immediately yields, for the lossless case,

$$R_{2,S_{1min}} = \omega L_2 \sqrt{1 - k_X^2} \; . \tag{2.5}$$

For very large coupling factors, the load resistance that minimizes the apparent power drawn tends toward zero. For small coupling factors, this load resistance converges to ωL_2.

Even though the apparent power drawn can generally be reduced by choosing the load resistance according to (2.5), it still rises very sharply at small magnitudes of the coupling factor. As a result, to transfer a given output power, the source must supply, in addition to active power, a reactive power that increases as the coupling factor decreases. This reactive power causes losses in the internal resistance of the source and also means that the source must be rated for a higher apparent power.

As the input apparent power increases, so does the reactive component of the input current $\boldsymbol{I}_1$ in Figure 2.1. In a lossy system, this increases the voltage drops across the unavoidable loss resistances. Consequently, as the coupling factor decreases, it becomes increasingly difficult to transfer power with sufficiently high efficiency.

Because of these limitations, power transfer with inductively coupled coils without additional measures appears practical only at large reactive coupling factors. As the coupling factor decreases, the inductances in the equivalent circuit of Figure 2.1 increasingly impede the power transfer. To overcome these difficulties, additional circuitry at the input and output of the transmission system is usually employed to minimize the

reactive power drawn while maximizing the efficiency [34, 35, 36]. For this purpose, resonant converters are used, which compensate the undesired inductances with resonant capacitors [37]. For example, for power and data transfer via coupled auxiliary windings, [22] uses a series capacitor at the input terminals and a parallel capacitor at the output terminals of the transmission system. This is shown in Figure 2.3. [38]

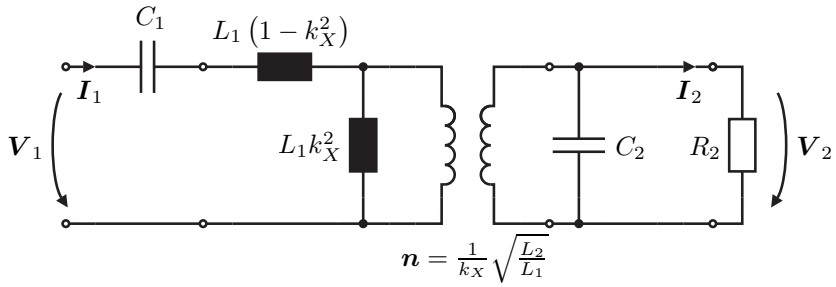

Figure 2.3.: *Example resonant circuitry of the lossless transmission system*

and [39] also use this circuitry for the inductively coupled windings, although [39] addresses not contactless power transfer but the design of an integrated resonant tank for conventional resonant converters.

For the uncompensated case, Figure 2.1 showed that, at small coupling factors k_X, most of the voltage applied to the input is not available at the output. If the capacitor C_1 in Figure 2.3 is now chosen such that the magnitude of its reactance at the desired frequency equals the reactance of the series inductance $L_1\,(1-k_X^2)$, these two reactances cancel, as in any series resonant circuit. As a result, the open-circuit voltage is considerably higher than in Figure 2.1. At this operating point, the open-circuit voltage depends on the coupling factor via the turns ratio $\boldsymbol{n}$, but is independent of the load resistance. Consequently, in the lossless case the short-circuit current tends toward infinity.

In Figure 2.1, most of an injected current flows through the shunt inductance $L_1 k_X^2$ rather than through the connected load resistance. This reactive current causes losses in the internal resistance of a source and in the loss resistances neglected here. If the resonant capacitor C_2 in Figure 2.3 is chosen such that the magnitude of its susceptance, after transformation by the ideal transformer, equals the magnitude of the susceptance of the shunt inductance $L_1 k_X^2$, these susceptances also cancel. As in any parallel resonant circuit excited at its resonant frequency, the total impedance then tends toward infinity. At resonance, the current in the inductance $L_1 k_X^2$ is supplied by the capacitor C_2 rather than by the source. Hence, taking into account the turns ratio of the ideal transformer, the input current flows directly to the output terminals.

Using Figure 2.3, the ratio of input apparent power to output active power can be

determined analogously to (2.4). With the definitions

$$\omega_1 = \sqrt{\frac{1}{L_1\left(1-k_X^2\right)C_1}}\,, \tag{2.6}$$

$$\omega_2 = \sqrt{\frac{1}{L_1 k_X^2 C_2}\underbrace{k_X^2\frac{L_1}{L_2}}_{\frac{1}{n^2}}} = \sqrt{\frac{1}{L_2 C_2}} \tag{2.7}$$

$$\tag{2.8}$$

and

$$Q_{R_2} = \frac{\omega L_2}{R_2}\,, \tag{2.9}$$

the relationship

$$\begin{aligned}\frac{\boldsymbol{S}_1}{P_2} = 1 &+ j\frac{1-k_X^2}{k_X^2 Q_{R_2}}\left[\frac{\omega^4}{\omega_2^4} + Q_{R_2}^2 - \frac{\omega_1^2}{\omega^2}\left(1+Q_{R_2}^2\right)\right] \\ &+ j\frac{2}{k_X^2 Q_{R_2}}\frac{\omega_1^2}{\omega_2^2}\left(1-k_X^2\right)\left[1-\frac{\omega^2}{\omega_1^2}\right] \\ &+ j\frac{1}{k_X^2 Q_{R_2}}\left[1-\frac{\omega^2}{\omega_2^2}\left(\frac{\omega_1^2}{\omega_2^2}\left(1-k_X^2\right)+k_X^2\right)\right]\end{aligned} \tag{2.10}$$

follows. Notably, the factors in square brackets vanish for the design choice $\omega_1 = \omega_2 = \omega$. In this case, the input apparent power equals the output active power, and the input reactive power is therefore zero. Consequently, unlike in Figure 2.2, no reactive power is drawn from the source even at very small coupling factors. Together with the properties mentioned above, this enables power transfer at small coupling factors and thus also over large distances.

In recent years, series capacitors on both sides, as shown in Figure 2.4, have become increasingly common. This topology is also used by the industry consortia mentioned in the introduction. In this representation, the windings coupled according to (2.1) are represented by a symmetrical T equivalent circuit. This circuit is also presented in [22, 33] and, in the general case, can be derived from Figure 3.12(a) of this thesis. There are many different ways to dimension the resonant capacitors. For example, [40] presents a way of minimizing the dependence of the transfer characteristics on the coupling factor, and thus on the positioning of the coupled coils, by choosing the resonant capacitors C_1 and C_2. [41] describes how, by choosing the resonant capacitors together with an additional zero-phase control of the input impedance, the output voltage can be stabilized to a defined value independent of the coupling factor.

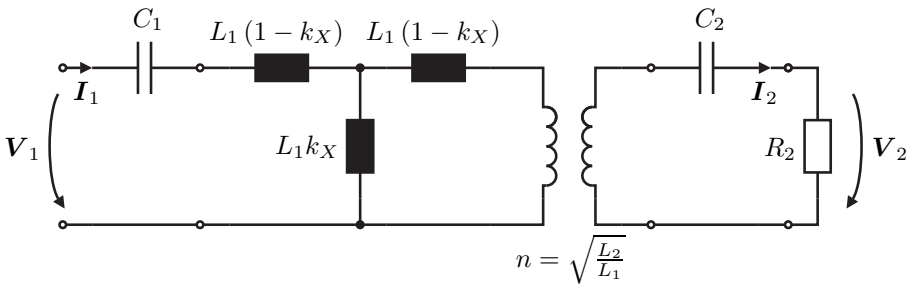

Figure 2.4.: *Further example resonant circuitry of the lossless transmission system*

Many previous publications assume that the resonant capacitor C_1 together with the self-inductance L_1 has the same resonant frequency as the resonant circuit consisting of the capacitor C_2 and the inductance L_2 [35, 36, 42, 43]. In these cases,

$$\omega_1 = \frac{1}{\sqrt{L_1 C_1}} = \frac{1}{\sqrt{L_2 C_2}} = \omega_2 \,. \tag{2.11}$$

The advantages of this dimensioning become particularly clear when the transmission system is voltage-fed. Figure 2.5 shows the normalized magnitude of the voltage transfer function of Figure 2.4, taking (2.11) into account, as a function of the frequency of the input voltage. Three different load resistances R_2 are shown. Notably, there are

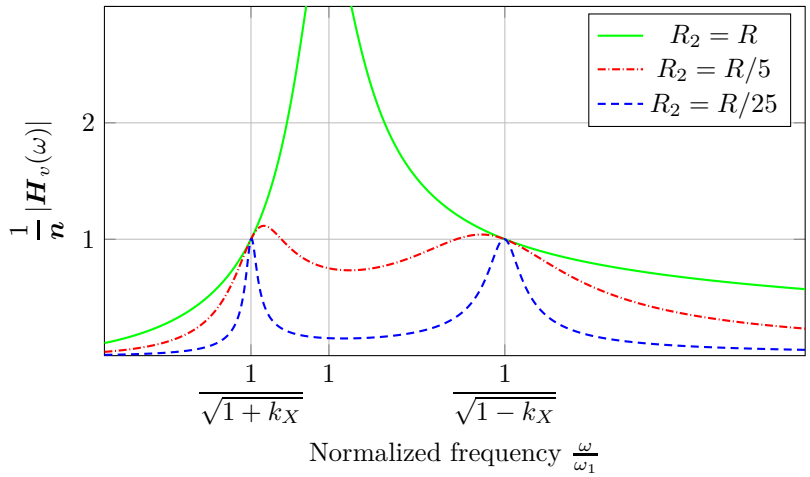

Figure 2.5.: *Normalized magnitude of the voltage transfer function, plotted versus normalized frequency*

two frequencies at which the magnitude of the voltage transfer function is independent of the connected load resistance. If the transmission system in Figure 2.4 is excited at such a frequency, the output voltage at constant input voltage depends only on

the turns ratio of the ideal transformer, and thus on the self-inductances of the two windings, but not on the coupling factor. These are referred to as the load-independent points of the voltage transfer function.

Since the self-inductances of inductive transmission systems are subject to tolerances, condition (2.11) is difficult to meet, and loss resistances are unavoidable, the magnitude of the voltage transfer function at the load-independent points also varies in real transmission systems. If a constant, load-independent output voltage is nevertheless required, it must be controlled. Here, too, the magnitude of the voltage transfer function in Figure 2.5 reveals an interesting relationship. Starting from the right load-independent point, the magnitude of the transfer function decreases monotonically with increasing frequency for every load resistance. The same applies, in the opposite direction, to the left load-independent point. This property makes it possible to control the output voltage via the frequency. With an additional feedback path, a control loop can then be implemented easily. The transmission systems of the industry consortia *WPC* and *PMA*, for example, use this method and close the control loop via an additional digital data link from the power receiver back to the power transmitter. Both systems use the range above the right load-independent point, because there the input impedance of the transmission system is inductive. This makes it possible to feed the system with the square-wave voltage of a simple class-D amplifier, i.e., a half or full bridge. Furthermore, the inductive input impedance allows the amplifier to operate with low losses under ZVS conditions [22, 37], i.e., zero-voltage switching.

Once loss resistances and tolerances are taken into account, it becomes increasingly difficult to transfer energy with acceptable efficiency as the coupling factor decreases. It can be shown that, for inductive systems according to Figure 2.5, the maximum possible efficiency is achieved approximately at the frequency ω_2 [30, 31], and the maximum power is transferred approximately at the frequency ω_1 [35]. In Figure 2.5, this would correspond to excitation at the frequency ω_1. It can be seen that, at this frequency, the magnitude of the voltage transfer function can vary widely depending on the load resistance. This makes controlling a constant output voltage at constant input voltage and variable load resistance considerably more difficult than, for example, above the right load-independent point. Nevertheless, because of the high efficiency, the industry consortium *A4WP* mentioned in the introduction operates at this frequency. In general, systems with very small coupling factors are mostly operated at this point. The output quantity is then often controlled by adjusting the input voltage.

This brief overview already shows that many, often very different, ways of connecting inductively coupled coils have been presented in recent years. The goal of this thesis is to focus on the essentials and to show, using a general transmission system, which measures enable high power transfer at maximum efficiency.

3. Transmission Systems

A transmission system describes the connection or coupling between a transmitter and a receiver. In general, it conveys physical quantities and can be used for power transfer as well as for signal or data transmission. This thesis focuses on the transfer of electrical energy from a power transmitter to a power receiver. The transmission systems considered in this thesis are assumed to be passive, linear, time-invariant, and reciprocal. Consequently, the systems described can be represented by an arbitrary interconnection of frequency-dependent resistances, inductances, and capacitances [44].

A transmitter feeds electrical energy into the transmission system, and a receiver draws part of this energy from it. Figure 3.1 illustrates this. The subscript t denotes transmitter quantities, and r denotes receiver quantities.

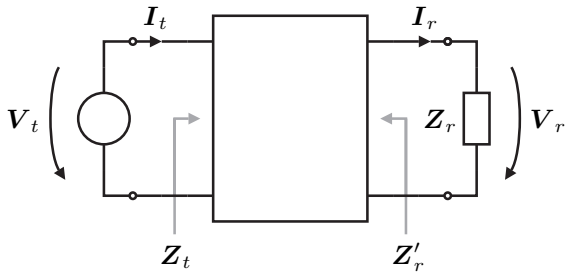

Figure 3.1.: *Transmission system as a two-port loaded by the impedance* Z_r

The source shown in Figure 3.1 can be either a current source or a voltage source. It is defined as an ideal source. If this idealization is not possible, the source impedance can be included as part of the transmission system. In this way, a source with internal impedance can also be modeled by an ideal source. In Figure 3.1, the sink is represented by the load impedance $\boldsymbol{Z}_r$. In the simplest case, it is a resistor, but it can also be the possibly complex input impedance of a downstream two-port.

The impedance $\boldsymbol{Z}_t$ is the input impedance of the transmission system loaded by $\boldsymbol{Z}_r$. It can be measured at the input port of the loaded two-port. The impedance $\boldsymbol{Z}'_r$ is the impedance that can be measured at the output port without a load impedance connected.

When analyzing an electrical transmission system, it is convenient to describe the transfer characteristics in the frequency domain. The bold type of all quantities in Figure 3.1 indicates that they are described by complex amplitudes. Below, the frequency dependence of the complex amplitudes is not stated explicitly where it is clear from the context.

The transmission systems considered here have two input terminals and two output terminals. Consequently, the transmission system can be described by a two-port [45]. Unlike the convention commonly used in communications engineering, the load (passive) sign convention is defined at the transmitter port and the generator (active) sign convention at the receiver port, as described in Appendix B. Transmission systems with more than two ports are not considered in this thesis. In principle, however, many of the relationships described below can be shown to apply to them as well.

Every linear time-invariant two-port can be described in the frequency domain by two linear equations [45, 46]. For example, the input voltage is given by the superposition

$$\boldsymbol{V}_t = \underbrace{\boldsymbol{Z}_{tt}\boldsymbol{I}_t}_{\boldsymbol{V}_{tt}} - \underbrace{\boldsymbol{Z}_{tr}\boldsymbol{I}_r}_{\boldsymbol{V}_{tr}} \ . \tag{3.1}$$

Accordingly, the voltage at the input port $\boldsymbol{V}_t$ depends not only on the input current but also on the current drawn at the output. An analogous equation applies to the voltage at the output port,

$$\boldsymbol{V}_r = \underbrace{\boldsymbol{Z}_{rt}\boldsymbol{I}_t}_{\boldsymbol{V}_{rt}} - \underbrace{\boldsymbol{Z}_{rr}\boldsymbol{I}_r}_{\boldsymbol{V}_{rr}} \ , \tag{3.2}$$

from which the system of equations

$$\begin{bmatrix} \boldsymbol{V}_t \\ \boldsymbol{V}_r \end{bmatrix} = \underbrace{\begin{bmatrix} \boldsymbol{Z}_{tt} & -\boldsymbol{Z}_{tr} \\ \boldsymbol{Z}_{rt} & -\boldsymbol{Z}_{rr} \end{bmatrix}}_{\text{Impedance matrix } \mathcal{Z}_{tr}} \begin{bmatrix} \boldsymbol{I}_t \\ \boldsymbol{I}_r \end{bmatrix} \tag{3.3}$$

follows. The impedance or Z matrix $\mathcal{Z}_{tr}$ in (3.3) fully characterizes the linear transmission system in the frequency domain. The elements of the Z matrix are frequency-dependent impedances. Figure 3.1 together with (3.1) and (3.2) yields the relationships

$$\boldsymbol{Z}_{tt} = \boldsymbol{Z}_t\big|_{\boldsymbol{I}_r=0} \tag{3.4}$$

and

$$\boldsymbol{Z}_{rr} = \boldsymbol{Z}'_r\big|_{\boldsymbol{I}_t=0} \ . \tag{3.5}$$

Because reciprocity is assumed, the two impedances $\boldsymbol{Z}_{tr}$ and $\boldsymbol{Z}_{rt}$ in (3.3) are identical:

$$\boldsymbol{Z}_{rt} = \boldsymbol{Z}_{tr} \ . \tag{3.6}$$

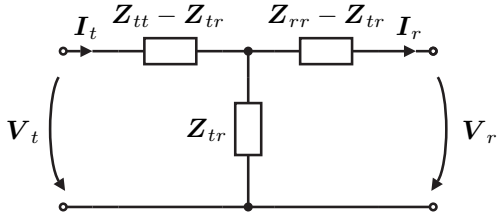

Figure 3.2.: *T impedance model*

From (3.3) and the reciprocity (3.6), the electrical equivalent circuit in Figure 3.2 follows directly. It is referred to as the T impedance model.

Sections A.1 and A.2 of the appendix derive the impedance matrices of an inductive and a capacitive transmission system. The results can be found in (A.35) on page 100 and in (A.77) on page 116, respectively.

3.1. Power Extraction

This section determines the requirements on the load impedance $\boldsymbol{Z}_r$ in Figure 3.1 that maximize the power-transfer efficiency of a given transmission system. In addition to the load impedance, a transfer quality factor is derived that indicates the maximum possible efficiency of a power transfer. Using this transfer quality factor, a transfer bandwidth is then introduced, which indicates how far a variable load resistance may deviate from its optimum. This makes the transfer quality factor a characteristic quantity that allows a wide variety of transmission systems to be compared.

If an arbitrary transmission system is fed by an ideal source, its efficiency depends not only on the system parameters but also on the operating frequency and on the load impedance $\boldsymbol{Z}_r$ in Figure 3.3. If the system and the frequency are given, only the dependence on the load remains. Since the output power drops to zero with both short-circuited and open output terminals, there must be a load impedance at which energy is transferred with a system-dependent maximum efficiency.

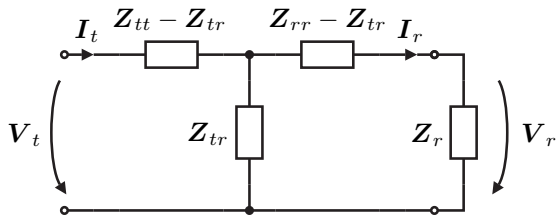

Figure 3.3.: *Loaded T impedance model*

The goal of this first section is to maximize the efficiency of the power transfer of a known transmission system by choosing a suitable load impedance $\boldsymbol{Z}_r$. How this load impedance is realized in practice is of secondary importance. In the simplest case, it consists of a discrete resistor and a discrete reactance, but it can also be the input impedance of any downstream network.

Appendix equation (B.11) shows that the efficiency depends on the magnitude of the current transfer function and on the real part of the input impedance. This makes it clear that an upstream impedance or the internal resistance of a source cannot affect the efficiency between the input and output terminals. The current transfer function and the input impedance of the two-port remain unchanged in both cases. Consequently, the efficiency can only be optimized by choosing a suitable load impedance.

Of course, this does not mean that the overall efficiency is independent of the internal resistance of a source. If, for example, an internal source resistance is taken into account, the overall efficiency can be improved further by minimizing the reactive current supplied by the source. The efficiency of the actual transmission system according to Figure 3.3, however, remains unaffected.

The current transfer function and the input impedance in (B.11) must be calculated according to (B.6) and (B.10). Using the impedance matrix $\mathcal{Z}_{tr}$ (3.3) and the reciprocity (3.6), the current transfer function

$$\boldsymbol{H}_i = \frac{\boldsymbol{Z}_{tr}}{\boldsymbol{Z}_r + \boldsymbol{Z}_{rr}} \tag{3.7}$$

and the input impedance

$$\boldsymbol{Z}_t = \frac{\boldsymbol{Z}_{tt}\boldsymbol{Z}_r + \det\mathcal{Z}_{tr}}{\boldsymbol{Z}_r + \boldsymbol{Z}_{rr}} \tag{3.8}$$

follow. Even though the magnitudes of (3.7) and (3.8) can be derived analytically without major difficulty, the resulting expressions are cumbersome and are omitted here. Only the further derivation of the ideal load impedance and the overall result of the optimization are presented here.

If all impedances of the model in Figure 3.3 are expressed by a real and an imaginary part according to $\boldsymbol{Z} = R + jX$, the efficiency of an arbitrary transmission system according to (B.11) can be described by

$$\eta = \frac{R_r\,(\alpha - \beta)}{(X_r - \gamma)^2 + (R_r + \alpha)\,(R_r + \beta)}\,, \tag{3.9}$$

with the substitutions

$$\alpha = R_{rr} + \frac{X_{tr}^2}{R_{tt}}\,, \tag{3.10}$$

$$\beta = R_{rr} - \frac{R_{tr}^2}{R_{tt}} \tag{3.11}$$

and

$$\gamma = \frac{X_{tr} R_{tr}}{R_{tt}} - X_{rr} \ . \tag{3.12}$$

Since a fraction with positive terms reaches its maximum when its denominator is minimal, (3.9) immediately shows that, to achieve the maximum efficiency, the imaginary part of the load impedance X_r must be chosen equal to γ:

$$X_{r,\eta} = \gamma = \frac{X_{tr} R_{tr}}{R_{tt}} - X_{rr} \ . \tag{3.13}$$

If the transmission system is loaded by an impedance whose reactive part equals $X_{r,\eta}$, the quadratic term in the denominator of (3.9) vanishes. What remains is a relationship which, after partial fraction decomposition, can be expressed as

$$\eta = \frac{\alpha}{\alpha + R_r} - \frac{\beta}{\beta + R_r} \ . \tag{3.14}$$

This expression shows that the efficiency tends toward zero for both very small and very large real parts of the load impedance R_r. This confirms the initial assumption that there is a load at which the efficiency is maximal. Its real part follows from setting the derivative of (3.14) to zero:

$$R_{r,\eta} = \sqrt{\alpha\beta} \ . \tag{3.15}$$

With (3.13) and (3.15), the load impedance $\boldsymbol{Z}_{r,\eta}$ that enables power transfer with maximum efficiency has been found. Ideally, the load equals the optimal impedance

$$\boldsymbol{Z}_{r,\eta} = R_{r,\eta} + jX_{r,\eta} \ . \tag{3.16}$$

Alternatively, (3.16) can be derived by partially differentiating (B.11) directly:

$$\frac{\partial}{\partial R_r}\eta = 0 \tag{3.17}$$

and

$$\frac{\partial}{\partial X_r}\eta = 0 \ . \tag{3.18}$$

Here, too, it can be shown that (3.18) is always satisfied for (3.13). Substituting (3.13) into (3.17) yields the real part:

$$R_{r,\eta} = \sqrt{\left(R_{rr} - \frac{R_{tr}^2}{R_{tt}}\right)\left(R_{rr} + \frac{X_{tr}^2}{R_{tt}}\right)} \ , \tag{3.19}$$

which also agrees with (3.15). Thus, the load impedance that optimizes the efficiency has also been found with an alternative approach.

To confirm that the point found is a maximum, the Hessian matrix is calculated. It can be shown that

$$\mathcal{H}(\eta) = \begin{bmatrix} \dfrac{\partial^2 \eta}{\partial R_{r,\eta}^2} & \dfrac{\partial^2 \eta}{\partial R_{r,\eta} \partial X_{r,\eta}} \\ \dfrac{\partial^2 \eta}{\partial X_{r,\eta} \partial R_{r,\eta}} & \dfrac{\partial^2 \eta}{\partial X_{r,\eta}^2} \end{bmatrix} = x \begin{bmatrix} -1 & 0 \\ 0 & -1 \end{bmatrix}, \tag{3.20}$$

where x is always positive, so that the Hessian matrix is negative definite. This proves that the point is a local maximum.

In the simplest case, the ideal load impedance (3.16) can be realized by a series connection of a resistor R and a reactance X according to

$$\boldsymbol{Z}_{r,\eta} = R_{r,\eta} + jX_{r,\eta} = R + jX \tag{3.21}$$

or, alternatively, by a parallel connection of R and X:

$$\boldsymbol{Z}_{r,\eta} = R_{r,\eta} + jX_{r,\eta} = \left(\frac{1}{R} + \frac{1}{jX} \right)^{-1} = \frac{RX^2}{R^2 + X^2} + j \frac{R^2 X}{R^2 + X^2} \,. \tag{3.22}$$

Comparing coefficients shows that, for the series connection (3.21), both the optimal resistance and the optimal reactance are already known from (3.15) and (3.13). In contrast, for the parallel connection (3.22), both the real part and the imaginary part depend on the resistance and the reactance. From (3.22) it follows that

$$R = \frac{R_{r,\eta}^2 + X_{r,\eta}^2}{R_{r,\eta}} \tag{3.23}$$

and

$$X = \frac{R_{r,\eta}^2 + X_{r,\eta}^2}{X_{r,\eta}} \,. \tag{3.24}$$

The preceding section has shown that, to optimize the efficiency, the load impedance must be matched to the transmission system. For the inductive transmission system presented in the appendix, for example, (3.10)–(3.15) and (A.35) yield an optimal load impedance of $\boldsymbol{Z}_{r,\eta} = 85.71\,\mathrm{m\Omega} - j124.99\,\mathrm{m\Omega}$. With a negative imaginary part, the impedance must have a resistive and a capacitive component. Since the example systems are specified at a frequency of 150 kHz, this results in a capacitance of 8.49 µF. By comparison, the capacitive transmission system requires, according to (A.77), an optimal impedance of $\boldsymbol{Z}_{r,\eta} = 239.18\,\mathrm{k\Omega} + j90.69\,\mathrm{k\Omega}$. The positive imaginary part means

that here the impedance must have an inductive component in addition to the resistive one. At a frequency of 150 kHz, an inductance of 96.23 mH results. The magnitudes of the optimal load impedances of the two example systems differ by several orders of magnitude.

Conversely, if the load impedance is fixed, the transmission system itself can sometimes be matched to it. For inductive transfer, this means adapting the inductances of the transmission system to the load resistance. Some matching options are presented in Chapter 4 of this thesis.

3.1.1. Transfer Quality Factor

Substituting (3.13) and (3.15) into (3.9) yields the maximum possible efficiency. Defining a transfer quality factor Q_k as

$$Q_k = \sqrt{\frac{\alpha}{\beta}} = \sqrt{\frac{1 + \frac{X_{tr}^2}{R_{tt} R_{rr}}}{1 - \frac{R_{tr}^2}{R_{tt} R_{rr}}}} \,, \tag{3.25}$$

the maximum possible efficiency of an arbitrary transmission system is

$$\eta_{max} = \frac{Q_k - 1}{Q_k + 1} \,. \tag{3.26}$$

For completeness, (3.15) can also be expressed in terms of the transfer quality factor. With (3.10) and (3.11),

$$R_{r,\eta} = Q_k \beta = \frac{\alpha}{Q_k} \,. \tag{3.27}$$

(3.26) shows that there is a simple relationship between the maximum possible efficiency and the transfer quality factor. Figure 3.4 illustrates this relationship graphically.

If the two-port parameters of an existing system are calculated or measured according to Appendix B.1, the maximum achievable efficiency can be determined directly with (3.25) and (3.26). For example, a system with a transfer quality factor of $Q_k = 10$ can, under optimal conditions, achieve an efficiency of just under 82%. This allows a wide variety of transmission systems to be evaluated and compared.

In [25] and in much of the literature on inductive power transfer [47, 48], the quantity χ or FOM is used. Even though the loss resistance R_{tr} is often neglected in the cited

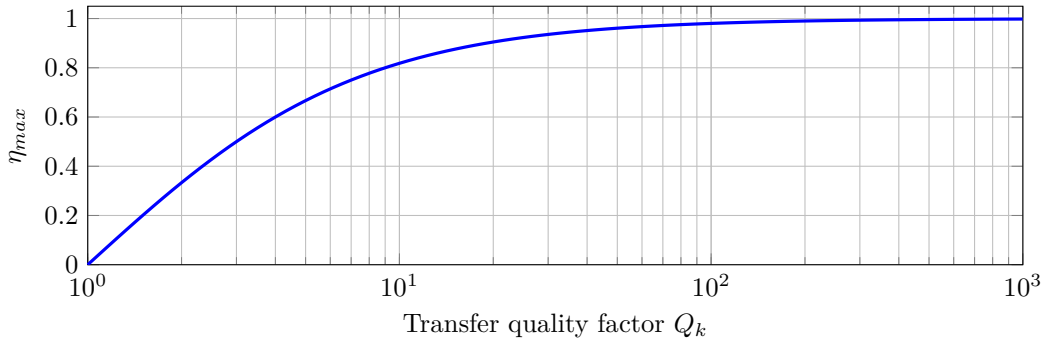

Figure 3.4.: *Efficiency versus transfer quality factor*

publications, the "**f**igure **o**f **m**erit" given there can be extended to

$$\chi = FOM = \sqrt{\frac{R_{tr}^2 + X_{tr}^2}{R_{tt}R_{rr} - R_{tr}^2}} \,. \tag{3.28}$$

This value also indicates the maximum achievable efficiency. The relationship between (3.25) and (3.28) is

$$Q_k = \sqrt{1 + FOM^2} \,. \tag{3.29}$$

Furthermore, for inductive coupling, [49] introduces a quality factor of the mutual inductance, Q_m. It corresponds to the quantity FOM when the loss resistance R_{tr} is neglected.

Because the FOM makes the expressions for the maximum possible efficiency (3.26) and the ideal load resistance (3.27) less convenient, it is not used further in this thesis.

The transfer quality factors of the example systems presented in Appendix A can be determined from their impedance matrices (A.35) and (A.77). Substituting (3.10) and (3.11) into (3.25) yields a transfer quality factor of $Q_k = 7.14$ for the inductive system and $Q_k = 260.49$ for the capacitive system. The capacitive example system thus has considerably better transfer characteristics than the inductive one. According to (3.26), the inductive system achieves a maximum efficiency of 75.44% under the best conditions. The capacitive system is considerably better: with the stated transfer quality factor, it can achieve a maximum efficiency of 99.2%. Since the two example systems were defined arbitrarily, it should not be concluded here that capacitive coupling is always better suited for power transfer than inductive coupling. For these two example systems, however, the capacitive one is clearly preferable.

3.1.2. Transfer Bandwidth

The preceding section considered the transmission system with optimal load impedance and thus at maximum efficiency. It assumed that both the real part and the imaginary part of the load impedance have the values defined by (3.15) and (3.13). In practice, however, this condition often cannot be met over the entire operating range. In particular, the real part of the load impedance depends on the active power drawn at the receiver and, depending on the application, can vary over a wide range.

Figure 3.5 shows the efficiency of two different systems versus the normalized real part of the load impedance on a logarithmic scale. The maximum at $R_r = R_{r,\eta}$ corresponds to the efficiency determined in (3.26). The imaginary part of the load impedance X_r is constant and corresponds to (3.13). It can be clearly seen that the efficiency decreases

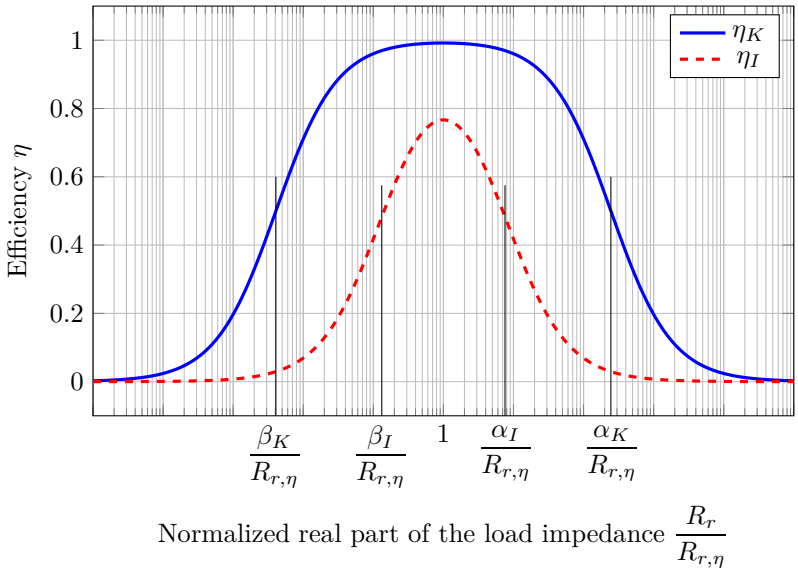

Figure 3.5.: *Efficiency of two different transmission systems according to (3.14), plotted versus the variable real part of the load impedance Z_r*

monotonically when the load resistance is increased or decreased starting from $R_{r,\eta}$. At the same time, system K maintains comparatively high efficiency over a wider range of load resistance than system I. It therefore makes sense to define a transfer bandwidth that describes the width of the high-efficiency range and, like the transfer quality factor, allows different transmission systems to be compared.

(3.14) already showed the influence of the two quantities α and β from (3.10) and (3.11) on the efficiency. They are also marked in Figure 3.5. Because of the symmetry of (3.14), the efficiency of a system at the abscissa value α equals that at the abscissa

value β. The relationships

$$\log\left(\frac{\alpha}{R_{r,\eta}}\right) = -\log\left(\frac{\beta}{R_{r,\eta}}\right) \tag{3.30}$$

and

$$\eta_\alpha = \eta_\beta = \frac{1}{2}\frac{Q_k^2 - 1}{Q_k^2 + 1} \tag{3.31}$$

hold.

If the range between α and β, normalized to the load resistance $R_{r,\eta}$ according to

$$B_k = \frac{\alpha - \beta}{R_{r,\eta}}\,, \tag{3.32}$$

is defined as the transfer bandwidth, this quantity characterizes the efficiency for a variable resistance R_r. By this definition, α is the maximum permissible and β the minimum permissible load resistance.

Using (3.25) and (3.27), the transfer bandwidth (3.32) can also be expressed in terms of the known transfer quality factor:

$$B_k = Q_k - \frac{1}{Q_k}\,, \tag{3.33}$$

according to which the transfer bandwidth asymptotically approaches the value of the transfer quality factor as the latter increases:

$$B_k \approx Q_k\big|_{Q_k \gg 1}\,. \tag{3.34}$$

Consequently, both the efficiency and the permissible variation of the load resistance increase with the transfer quality factor.

If only the transfer bandwidth B_k of a transmission system is known, the transfer quality factor can be determined by

$$Q_k = \frac{1}{2}\left(B_k + \sqrt{B_k^2 + 4}\right)\,. \tag{3.35}$$

Furthermore, substituting (3.35) into (3.27) allows the previously defined limiting resistances α and β to be determined solely from the transfer bandwidth and the optimal real part of the load impedance $R_{r,\eta}$.

Another interesting quantity is the ratio of the maximum permissible load resistance α to the minimum permissible load resistance β. It follows directly from (3.25):

$$\frac{\alpha}{\beta} = Q_k^2\,. \tag{3.36}$$

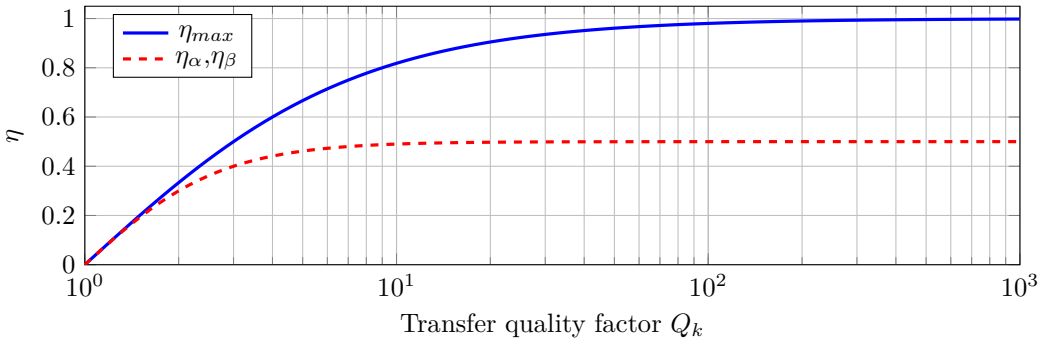

Figure 3.6.: *Maximum efficiency and efficiency at the band limit, plotted versus the transfer quality factor*

At high transfer quality factors, the efficiency at the band limit (3.31) is approximately 50%. As the transfer quality factor decreases, the efficiency at the band limit decreases as well, which further reduces the transfer bandwidth at low transfer quality factors. Figure 3.6 shows the maximum efficiency already known from Figure 3.4 together with the efficiency at the band limit (3.31), plotted versus the transfer quality factor.

Since the efficiency at the band limit is often too low for practical transmission systems, the load resistance range is also determined here for an arbitrarily specified limiting efficiency η_g instead of (3.31). From (3.14), the two limiting resistances

$$R_{r_{1,2}} = \frac{1}{2\eta_g}\left[\alpha\left(1-\eta_g\right) - \beta\left(1+\eta_g\right) \pm \sqrt{\left(\beta-\alpha\right)\left[\beta\left(1+\eta_g\right)^2 - \alpha\left(1-\eta_g\right)^2\right]}\right] \tag{3.37}$$

follow. The limiting efficiency η_g must be chosen smaller than η_{max} according to (3.26); otherwise, (3.37) does not yield a usable result.

The transfer bandwidths of the example systems from Appendix A follow from their transfer quality factors (Section 3.1.1) with (3.33). For the inductive transmission system, this results in a transfer bandwidth of $B_k = 7$. With (3.35) and (3.27), this value yields a permissible variation of the load resistance of $12\,\mathrm{m\Omega} \leq R_r \leq 612.25\,\mathrm{m\Omega}$. This range is therefore very narrow. The capacitive transmission system behaves differently: with $B_k = 260.49$, the load resistance can vary over a much wider range while maintaining efficient power transfer: $918.2\,\Omega \leq R_r \leq 62.3\,\mathrm{M\Omega}$. Figure 3.5 already showed the efficiency of the example systems versus the normalized load resistance R_r. The index K denotes the capacitive and the index I the inductive system.

3.2. Power Injection

Section 3.1 showed that, for every lossy transmission system, there is a load impedance $\boldsymbol{Z}_{r,\eta}$ according to (3.16) at which the system transfers energy with maximum efficiency. It also became clear that a source impedance cannot increase the efficiency. A suitable source impedance can, however, influence and ideally maximize the available output power. Since a resistive component would reduce the efficiency, the source impedance is restricted to a pure reactance, whose value is determined below.

This section identifies the requirements that the source must meet. For this purpose, the transfer characteristics of the system are first determined from its transfer functions.

3.2.1. Transfer Functions

The general input impedance and the general current transfer function were already found in (3.7) and (3.8). If a transmission system is terminated with the ideal load reactance but an arbitrary resistance R_r, the input impedance $\boldsymbol{Z}_t$ according to Figure 3.1 can be described, using (3.10), (3.11), and (B.10), by its real part

$$R_t = R_{tt}\frac{(R_r+\alpha)(R_r+\beta)}{(R_r+R_{rr})^2+R_{rr}(\alpha+\beta-R_{rr})-\alpha\beta} \tag{3.38}$$

and its imaginary part

$$X_t = X_{tt} - \frac{X_{tr}R_{tr}}{R_{rr}}\frac{R_{rr}(2R_r+\alpha+\beta)}{(R_r+R_{rr})^2+R_{rr}(\alpha+\beta-R_{rr})-\alpha\beta}\,. \tag{3.39}$$

If, in addition, the system is loaded with the ideal load resistance $R_{r,\eta}$, (3.38) and (3.39) simplify to

$$R_t = \frac{R_{tt}}{R_{rr}}\sqrt{\alpha\beta} = \frac{R_{tt}}{R_{rr}}R_{r,\eta} \tag{3.40}$$

and

$$X_t = X_{tt} - \frac{X_{tr}R_{tr}}{R_{rr}}\,. \tag{3.41}$$

The similarity between (3.41) and the ideal load reactance (3.13) is evident.

The current transfer function can be calculated according to (B.6). With an arbitrary load resistance and the ideal load reactance,

$$\operatorname{Re}\boldsymbol{H}_i = R_{tr}\frac{R_r+\alpha}{(\alpha-R_{rr})(R_{rr}-\beta)+(R_r+R_{rr})^2} \tag{3.42}$$

and

$$\operatorname{Im} \boldsymbol{H}_i = X_{tr} \frac{R_r + \beta}{(\alpha - R_{rr})(R_{rr} - \beta) + (R_r + R_{rr})^2} \tag{3.43}$$

follow. Here, too, (3.42) and (3.43) can be simplified if the ideal load resistance is connected in addition to the ideal load reactance:

$$\operatorname{Re} \boldsymbol{H}_i = \frac{R_{tr}}{R_{rr}} \frac{\sqrt{\alpha}}{\sqrt{\alpha} + \sqrt{\beta}} \tag{3.44}$$

and

$$\operatorname{Im} \boldsymbol{H}_i = \frac{X_{tr}}{R_{rr}} \frac{\sqrt{\beta}}{\sqrt{\alpha} + \sqrt{\beta}} \,. \tag{3.45}$$

Using (B.8), the voltage transfer function $\boldsymbol{H}_v$ of the transmission system can be calculated from (3.38)–(3.45). For simplicity, only its magnitude for termination with the ideal load reactance is given:

$$|\boldsymbol{H}_v| = \frac{\sqrt{R_r^2 + \gamma^2}\,|\boldsymbol{H}_i|}{|\boldsymbol{Z}_t|} \tag{3.46}$$

$$|\boldsymbol{H}_v| = \sqrt{\frac{(R_r^2 + \gamma^2)\left[\dfrac{R_{tr}^2}{(R_r + \beta)^2} + \dfrac{X_{tr}^2}{(R_r + \alpha)^2}\right]}{\left[\dfrac{R_{tr}X_{tr} - (R_r + R_{rr})\,X_{tt}}{R_r + \beta} + \dfrac{R_{tr}X_{tr} - (R_{rr} - \alpha)\,X_{tt}}{R_r + \alpha}\right]^2 + R_{tt}^2}} \,. \tag{3.47}$$

With additional termination by the optimal load resistance $R_{r,\eta}$, this simplifies to

$$|\boldsymbol{H}_v| = \sqrt{\frac{(\alpha\beta + \gamma^2)\,(\alpha R_{tr}^2 + \beta X_{tr}^2)}{\left(\sqrt{\alpha} + \sqrt{\beta}\right)^2 \left[(R_{tr}X_{tr} - R_{rr}X_{tt})^2 + \alpha\beta R_{tt}^2\right]}} \,. \tag{3.48}$$

The voltage transfer function describes the ratio of the voltage across the output impedance to the input voltage. If only the voltage across the load resistance at the output is required, it can be determined from (3.47) or (3.48) according to

$$\left|\frac{\boldsymbol{V}_{R_r}}{\boldsymbol{V}_t}\right| = \frac{R_r\,|\boldsymbol{H}_i|}{|\boldsymbol{Z}_t|} = |\boldsymbol{H}_v|\,\big|_{\gamma=0} \,. \tag{3.49}$$

With the input impedance known from (3.38) and (3.39), the behavior at the input terminals is described as a function of the load impedance at the output. The source driving this input impedance therefore represents the source driving the overall system. A distinction must be made between a voltage source and a current source.

3.2.2. Voltage Feed

If the transmission system is fed by a constant input voltage, a source reactance connected in parallel with the input impedance has no effect on the power transfer. Only a series reactance, as shown in Figure 3.7, has an effect.

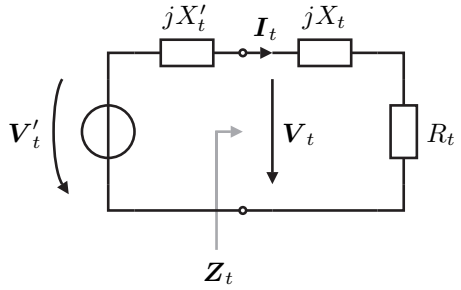

Figure 3.7.: *Voltage source with series reactance*

The active power fed into the system is dissipated entirely in the real part of the input impedance R_t. It is calculated as

$$P_t = |\boldsymbol{V}'_t|^2 \frac{R_t}{2\left[R_t^2 + (X'_t + X_t)^2\right]} . \tag{3.50}$$

(3.50) shows directly that the maximum active power is fed into the system when

$$X'_t = -X_t . \tag{3.51}$$

This can be explained intuitively: a positive and a negative reactance in series compensate each other. The reactances cancel, and the input voltage $\boldsymbol{V}'_t$ in Figure 3.7 drops entirely across the real part of the input impedance.

If the transmission system is terminated with the ideal load impedance according to Section 3.1, the transferred power is determined solely by the source amplitude. With (3.40), (3.41), and (3.51), it follows from (3.49) for voltage feed according to Figure 3.7 that, to transfer a given output power P_r, the system must be fed by an input voltage $\boldsymbol{V}'_t$ with an amplitude of

$$|\boldsymbol{V}'_t| = R_{tt} \frac{\sqrt{\alpha} + \sqrt{\beta}}{\sqrt{\alpha R_{tr}^2 + \beta X_{tr}^2}} \sqrt{2P_r\sqrt{\alpha}\sqrt{\beta}} . \tag{3.52}$$

Assuming that the capacitive example system from Appendix A.2 is loaded with the optimal load impedance $Z_{r,\eta}$, a source reactance of $j90.69\,\mathrm{k\Omega}$ is required according to (3.51) to maximize the output power. At a frequency of 150 kHz, this corresponds to an inductance of 96.23 mH. If, for example, a power of 10 W is to be delivered to the real part of the load impedance, (3.52) yields a required input voltage amplitude of 2.2 kV.

3.2.3. Current Feed

When the system is fed by a current source, the series reactance from Figure 3.7 has no effect. However, if a parallel reactance is taken into account, as shown in Figure 3.8,

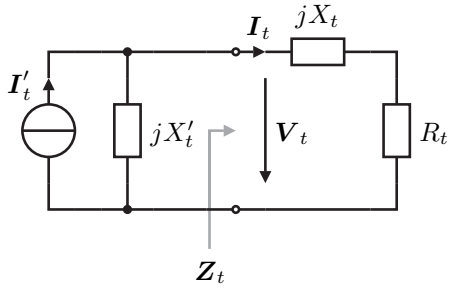

Figure 3.8.: *Current source with parallel reactance*

the power dissipated in the resistance R_t can be calculated as

$$P_t = |\boldsymbol{I}'_t|^2 \frac{R_t X_t'^2}{2\left[R_t^2 + (X'_t + X_t)^2\right]} . \tag{3.53}$$

Differentiation and subsequent root finding show that the maximum active power is delivered with the parallel reactance

$$X'_t = -X_t - \frac{R_t^2}{X_t} . \tag{3.54}$$

Here, too, with the load chosen according to Section 3.1, the transferred output power is determined by the amplitude of the input current. From (3.44), (3.45), and (3.54) it follows that, to transfer an active power P_r, the system must be fed by an input current $\boldsymbol{I}'_t$ with the amplitude

$$|\boldsymbol{I}'_t| = R_{tt} R_{rr} \frac{\sqrt{\alpha} + \sqrt{\beta}}{\sqrt{\alpha R_{tr}^2 + \beta X_{tr}^2}} \sqrt{\frac{2P_r\sqrt{\alpha}\sqrt{\beta}}{(R_{tr}X_{tr} - R_{rr}X_{tt})^2 + \alpha\beta R_{tt}^2}} . \tag{3.55}$$

Similar to (3.21) and (3.22), comparing (3.51) and (3.54) shows that, for voltage feed, the source reactance can be chosen independently of the real part of the input impedance and thus, according to (3.40), also independently of the load resistance. In contrast, for current feed, the source reactance depends on the real part of the input impedance and thus, according to (3.40), also on the load resistance.

For the inductive example system loaded with the optimal load impedance $Z_{r,\eta}$, a source reactance of $-183.77\,\mathrm{m\Omega}$ is required according to (3.54). At the chosen frequency, this corresponds to a capacitance of $5.77\,\mu\mathrm{F}$. If an active power of $10\,\mathrm{W}$ is to be delivered at the output, (3.55) yields a required input current amplitude of $9.95\,\mathrm{A}$.

3.3. Equivalent Circuits

Suitable equivalent circuits help explain the behavior of electromagnetic systems. This section introduces several equivalent circuits of the transmission system. Depending on the aspect of interest, one of them illustrates a given relationship particularly clearly, so the equivalent circuit should be chosen to suit the task at hand.

Several transformer-based equivalent circuits are presented below. [33, 22] already derived these equivalent circuits for the special case of lossless inductive coupling. In contrast, the circuits presented here describe the general case.

In addition to the transformer-based equivalent circuits, a new gyrator-based equivalent circuit is introduced in Section 3.3.2.

3.3.1. Transformer-Based Equivalent Circuits

A first equivalent circuit of the transmission system (3.3) was already presented in Figure 3.2. According to this equivalent circuit, every reciprocal system can be described by at most three impedances.

In a general two-port, by definition, the current flowing into one terminal of a port flows out of the other terminal of the same port. No current ever flows directly from the input to the output. Consequently, the two ports appear galvanically isolated when viewed from outside. Purely formally, this galvanic isolation can be made explicit by adding an ideal transformer with a turns ratio of $n = 1$.

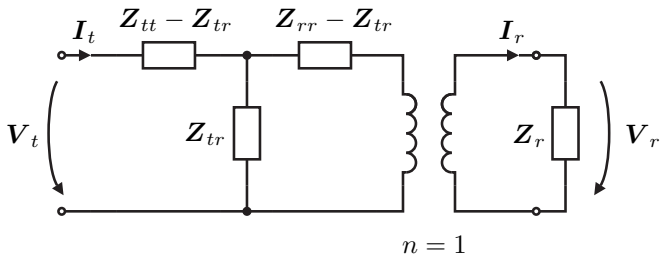

Figure 3.9.: *T impedance model from Figure 3.1 extended by an ideal transformer*

By definition [32], the ideal transformer converts a sinusoidal input voltage into a proportional sinusoidal output voltage of the same phase, with $\boldsymbol{V}_2 = n\boldsymbol{V}_1$ and $\boldsymbol{I}_1 = n\,\boldsymbol{I}_2$. For the conventional ideal transformer, the turns ratio n is a real quantity. The ideal transformer is lossless.

Complex Transformer

If, purely formally, the usual definition of the ideal transformer is relaxed to allow a complex turns ratio $\boldsymbol{n}$, the transformer in Figure 3.10 results.

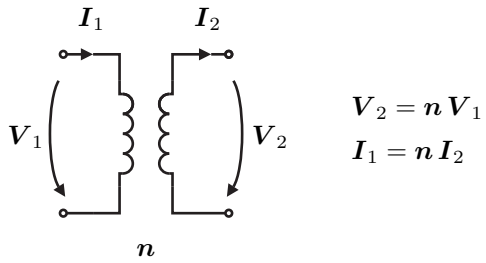

Figure 3.10.: *Transformer with complex turns ratio*

Analogous to the transfer functions of an ideal transformer, the relationships

$$\boldsymbol{V}_2 = \boldsymbol{n}\,\boldsymbol{V}_1 \tag{3.56}$$

$$\boldsymbol{I}_1 = \boldsymbol{n}\,\boldsymbol{I}_2 \tag{3.57}$$

can be defined. As the complex turns ratio $\boldsymbol{n}$ already suggests, the complex transformer is a purely AC element. If both the voltages and the turns ratio in (3.56) are regarded as phasors in the complex plane $\mathbb{C}$, it becomes clear that the input voltage can be represented according to

$$\boldsymbol{V}_1 = \frac{1}{\boldsymbol{n}}\,\boldsymbol{V}_2 = \frac{|\boldsymbol{V}_2|}{|\boldsymbol{n}|} e^{j(\varphi_{\boldsymbol{V}_2} - \varphi_{\boldsymbol{n}})} \tag{3.58}$$

by a phasor that is generally phase-shifted with respect to the phasor of the output voltage $\boldsymbol{V}_2$. Analogously, according to (3.57), the phasor of the input current is

$$\boldsymbol{I}_1 = \boldsymbol{n}\,\boldsymbol{I}_2 = |\boldsymbol{n}||\boldsymbol{I}_2| e^{j(\varphi_{\boldsymbol{I}_2} + \varphi_{\boldsymbol{n}})}\ . \tag{3.59}$$

(3.58) and (3.59) show that the two phasors are rotated by the same angle, but in opposite directions. This difference in the direction of rotation affects the transfer of apparent power. From (3.56) and (3.57), together with the definition of apparent power

$$\boldsymbol{S}_1 = \boldsymbol{V}_1 \boldsymbol{I}_1^* \tag{3.60}$$

$$\boldsymbol{S}_2 = \boldsymbol{V}_2 \boldsymbol{I}_2^*\,, \tag{3.61}$$

it immediately follows that

$$\boldsymbol{S}_1 = \frac{\boldsymbol{n}^*}{\boldsymbol{n}} \boldsymbol{V}_2 \boldsymbol{I}_2^* = \frac{\boldsymbol{n}^*}{\boldsymbol{n}} \boldsymbol{S}_2 \quad \Rightarrow \quad \frac{\boldsymbol{S}_2}{\boldsymbol{S}_1} = \underbrace{\frac{\boldsymbol{n}}{\boldsymbol{n}^*}}_{e^{j(2\varphi_{\boldsymbol{n}})}}\ . \tag{3.62}$$

Consequently, the complex input power $\boldsymbol{S}_1$ and the complex output power $\boldsymbol{S}_2$ have the same magnitude but different phase angles. For a known output apparent power, this means that the complex input power $\boldsymbol{S}_1$ lies on a circle of radius $|\boldsymbol{S}_2|$ around the origin. This is shown in Figure 3.11.

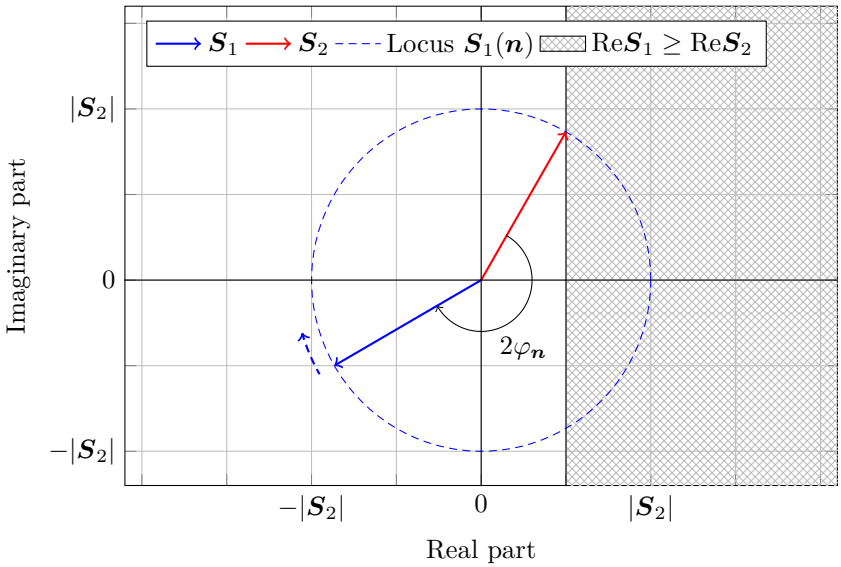

Figure 3.11.: *Relationship between input and output apparent power of the complex transformer*

The position of the input apparent power $\boldsymbol{S}_1$ depends on the phase of the complex turns ratio. If the phase of the turns ratio rotates clockwise, $\boldsymbol{S}_1$ also rotates clockwise about the origin of the complex plane, at twice the angular rate. This is shown by a locus in Figure 3.11.

The possibility of rotating the input apparent power about the origin has an interesting consequence. Depending on the rotation angle $\varphi_{\boldsymbol{n}}$, a system can be described in which the input active power is smaller than the output active power. This corresponds to a theoretical efficiency of the complex transformer greater than one:

$$\eta \leq 1 \quad \text{if} \quad \varphi_{\boldsymbol{n}} \geq 0 \quad \text{and} \quad \varphi_{\boldsymbol{n}} \leq \varphi_{\boldsymbol{S}_2} \tag{3.63}$$

$$\eta \leq 1 \quad \text{if} \quad \varphi_{\boldsymbol{n}} \geq \pi \quad \text{and} \quad \varphi_{\boldsymbol{n}} \leq \pi + \varphi_{\boldsymbol{S}_2} \tag{3.64}$$

$$\eta > 1 \quad \text{otherwise .} \tag{3.65}$$

Because of the law of conservation of energy, however, the complex transformer can only be realized in practice under certain boundary conditions. In an equivalent circuit with additional external circuitry, on the other hand, individual parts of the circuit can be interpreted as a complex transformer. It must then merely be ensured that the

losses unavoidable in practice are dissipated in an additional component that is taken into account.

As with an ideal transformer, an impedance $\boldsymbol{Z}_2$ connected at the output of a complex transformer is reflected to the input as $\boldsymbol{Z}_1$:

$$\boldsymbol{Z}_1 = \frac{\boldsymbol{V}_1}{\boldsymbol{I}_1} = \frac{1}{\boldsymbol{n}^2}\frac{\boldsymbol{V}_2}{\boldsymbol{I}_2} = \frac{1}{\boldsymbol{n}^2}\boldsymbol{Z}_2 \ . \tag{3.66}$$

Here, too, the possibility of phase rotation becomes apparent. Any impedance $\boldsymbol{Z}_2$ connected at the output can be transformed into any desired input impedance $\boldsymbol{Z}_1$.

To simplify calculations with the complex transformer, a two-port description proves particularly helpful. Since, as for the ideal transformer, no impedance matrix exists [46], only a chain matrix can be given. From (3.56) and (3.57) it follows directly that

$$\mathcal{A}_T = \begin{bmatrix} \dfrac{1}{\boldsymbol{n}} & 0 \\ 0 & \boldsymbol{n} \end{bmatrix} \ . \tag{3.67}$$

The complex transformer is reciprocal. This can be confirmed with (3.67) by $\det\mathcal{A}_T = 1$. Furthermore, a complex transformer with a real turns ratio behaves identically to an ideal transformer.

Equivalent Circuits

If the equivalent circuit in Figure 3.9 is drawn with a complex transformer instead of an ideal transformer, the complex turns ratio provides a fourth system quantity in addition to the three impedances. This extra degree of freedom allows one of the three complex quantities $\boldsymbol{Z}_{tt}$, $\boldsymbol{Z}_{rr}$, $\boldsymbol{Z}_{tr}$ or the complex turns ratio $\boldsymbol{n}$ of the equivalent circuit to be specified arbitrarily. The three remaining quantities are then recalculated accordingly.

With the specification $\boldsymbol{Z}_{rr} = \boldsymbol{Z}_{tt}$, using the complex transformer and the coupling factor defined in (B.13), the symmetrical T impedance model in Figure 3.12(a) follows from Figure 3.9. This equivalent circuit shows clearly that the complex transformer, via (3.66), transforms the impedance $\boldsymbol{Z}_{tt}$, which can be measured at the output of the T network with the input terminals open, into the impedance $\boldsymbol{Z}'_r = \boldsymbol{Z}_{rr}$ actually present according to (3.5), and thus corrects it. In the general case, this transformation is only possible with a complex transformer, since only it can perform an arbitrary impedance transformation according to (3.66). Conversion to an ideal transformer would only be possible in the case described here if $\boldsymbol{Z}_{tt}$ could be transformed into $\boldsymbol{Z}_{rr}$ by a real factor.

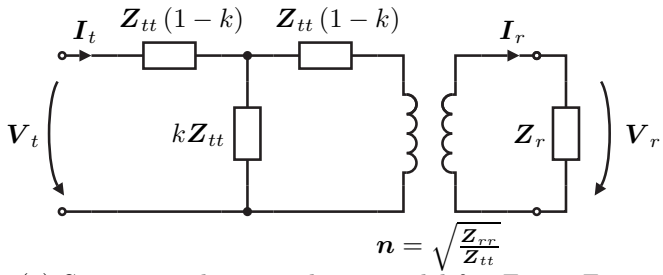

(a) Symmetrical T impedance model for $\boldsymbol{Z}_{rr} = \boldsymbol{Z}_{tt}$

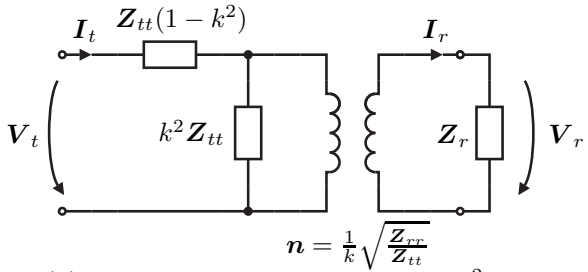

(b) Γ_1 impedance model for $\boldsymbol{Z}_{tr} = k^2\boldsymbol{Z}_{tt}$

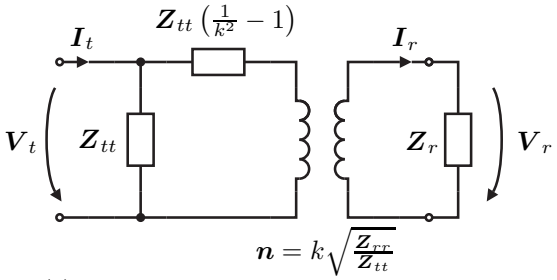

(c) Γ_2 impedance model for $\boldsymbol{Z}_{tr} = \boldsymbol{Z}_{tt}$

Figure 3.12.: *Equivalent circuits of the impedance model with complex transformer*

Further equivalent circuits can be derived in the same way. A selection is shown in Figure 3.12. Figure 3.12(b) is based on the assumption $\boldsymbol{Z}_{tr} = k^2\boldsymbol{Z}_{tt}$. Figure 3.12(c) assumes by definition that $\boldsymbol{Z}_{tr} = \boldsymbol{Z}_{tt}$. In each case, the turns ratio $\boldsymbol{n}$ of the complex transformer accounts for the difference between the assumed relationship and the actual system.

Viewed from the input or output port, the equivalent circuits shown are identical. This is easily checked using the open-circuit output voltage for an injected current $\boldsymbol{I}_t$. In

the three cases, it is given by

$$\text{Figure 3.12(a)} \Rightarrow \boldsymbol{V}_{r_O} = \boldsymbol{I}_t \, k \boldsymbol{Z}_{tt} \sqrt{\frac{\boldsymbol{Z}_{rr}}{\boldsymbol{Z}_{tt}}} = \boldsymbol{I}_t \boldsymbol{Z}_{tr} \tag{3.68}$$

$$\text{Figure 3.12(b)} \Rightarrow \boldsymbol{V}_{r_O} = \boldsymbol{I}_t \, k^2 \boldsymbol{Z}_{tt} \frac{1}{k} \sqrt{\frac{\boldsymbol{Z}_{rr}}{\boldsymbol{Z}_{tt}}} = \boldsymbol{I}_t \boldsymbol{Z}_{tr} \tag{3.69}$$

$$\text{Figure 3.12(c)} \Rightarrow \boldsymbol{V}_{r_O} = \boldsymbol{I}_t \, \boldsymbol{Z}_{tt} \, k \sqrt{\frac{\boldsymbol{Z}_{rr}}{\boldsymbol{Z}_{tt}}} = \boldsymbol{I}_t \boldsymbol{Z}_{tr} \tag{3.70}$$

and is thus identical to the open-circuit voltage of the equivalent circuit in Figure 3.9. The same can be shown for all other transfer quantities and states.

3.3.2. Gyrator-Based Equivalent Circuit

Another equivalent circuit can be derived directly from the system equations. Because of reciprocity, (3.3) and (3.6) yield the system of equations

$$\begin{bmatrix} \boldsymbol{V}_t \\ \boldsymbol{V}_r \end{bmatrix} = \begin{bmatrix} \boldsymbol{Z}_{tt} & -\boldsymbol{Z}_{tr} \\ \boldsymbol{Z}_{tr} & -\boldsymbol{Z}_{rr} \end{bmatrix} \begin{bmatrix} \boldsymbol{I}_t \\ \boldsymbol{I}_r \end{bmatrix}, \tag{3.71}$$

restated here for convenience. (3.71) shows that both the input and the output current, each multiplied by an impedance, contribute to the voltage at both ports. Thus, the transmitter-side current $\boldsymbol{I}_t$ multiplied by the impedance $\boldsymbol{Z}_{tt}$ yields the transmitter-side voltage $\boldsymbol{V}_{tt}$. In this case, both the current and the voltage occur at the transmitter. The same applies to $\boldsymbol{I}_r$, $\boldsymbol{Z}_{rr}$, and $\boldsymbol{V}_{rr}$ on the receiver side, where these quantities occur exclusively at the receiver.

The impedance $\boldsymbol{Z}_{tr}$ behaves differently: the voltages across it are caused by the current on the opposite side. From (3.71), or from (3.1) and (3.2), the relationships

$$-\boldsymbol{V}_{tr} = \boldsymbol{Z}_{tr} \boldsymbol{I}_r \tag{3.72}$$

$$\boldsymbol{V}_{rt} = \boldsymbol{Z}_{tr} \boldsymbol{I}_t \tag{3.73}$$

follow. These closely resemble the description of the gyrator shown in Figure 3.13(a) according to [50], although here an impedance $\boldsymbol{Z}_{tr}$ appears instead of a gyration resistance, and the voltage $\boldsymbol{V}_{tr}$ has a negative sign. To account for this difference, a new element modeled on the conventional ideal gyrator is introduced, referred to below as the complex gyrator.

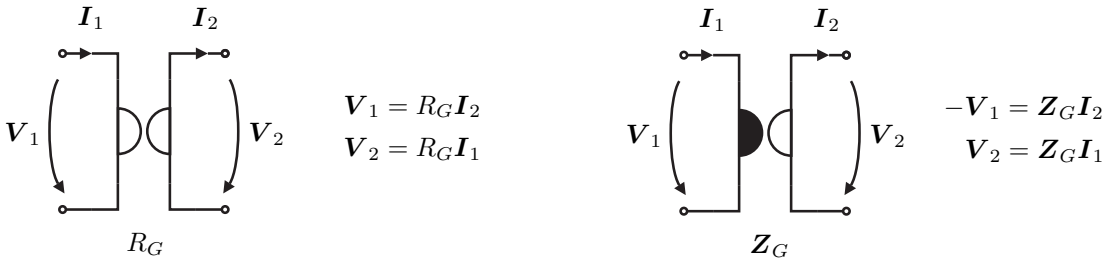

(a) Ideal gyrator (b) Complex gyrator

Figure 3.13.: *Comparison of ideal gyrator and complex gyrator*

Complex Gyrator

Figure 3.13(b) shows the chosen symbol of the complex gyrator with the complex gyration impedance $\boldsymbol{Z}_G$. The shading of the input, compared to the conventional ideal gyrator in Figure 3.13(a), reflects the negation of the input voltage according to (3.72). As can be seen from Figure 3.13(b), the proportionalities

$$-\boldsymbol{V}_1 = \boldsymbol{Z}_G \boldsymbol{I}_2 \tag{3.74}$$

$$\boldsymbol{V}_2 = \boldsymbol{Z}_G \boldsymbol{I}_1 \tag{3.75}$$

apply here.

$\boldsymbol{Z}_G$ is the complex gyration impedance. Like the complex transformer, the complex gyrator is a purely AC element. From Figure 3.13(b), (3.74), and (3.75), together with

$$\boldsymbol{S}_1 = \boldsymbol{V}_1 \boldsymbol{I}_1^* \tag{3.76}$$

$$\boldsymbol{S}_2 = \boldsymbol{V}_2 \boldsymbol{I}_2^* \,, \tag{3.77}$$

the relationship

$$\boldsymbol{S}_1 = -\frac{\boldsymbol{Z}_G}{\boldsymbol{Z}_G^*} \boldsymbol{V}_2^* \boldsymbol{I}_2 = -\frac{\boldsymbol{Z}_G}{\boldsymbol{Z}_G^*} \boldsymbol{S}_2^* \quad \Rightarrow \quad \frac{\boldsymbol{S}_2^*}{\boldsymbol{S}_1} = \underbrace{-\frac{\boldsymbol{Z}_G^*}{\boldsymbol{Z}_G}}_{e^{j\left(\pi - 2\varphi_{Z_G}\right)}} \tag{3.78}$$

follows. (3.78) shows that the relationship between input and output apparent power is similar to that of the complex transformer according to (3.62). Depending on the gyration impedance, the complex output power is likewise rotated about the origin of the complex plane. Consequently, analogous to Figure 3.11, a state can be realized in which the efficiency of the complex gyrator is greater than one. The same reasoning applies as for the complex transformer (Section 3.3.1, page 38), although the phase conditions are different.

The relationship between input and output apparent power is identical for the complex transformer and the complex gyrator if

$$\varphi_{\boldsymbol{Z}_G} = \frac{\pi}{2} - \varphi_{\boldsymbol{n}} - \varphi_{\boldsymbol{s}_2} \,. \tag{3.79}$$

This does not mean, however, that the complex gyrator can be converted into a complex transformer, because their defining proportionalities differ fundamentally; compare (3.56), (3.57) and (3.74), (3.75).

As with a conventional gyrator, an impedance $\boldsymbol{Z}_2$ connected at the output is reflected to the input as its inverse, $\boldsymbol{Z}_1$. Here, however, the relationship

$$\boldsymbol{Z}_1 = \frac{\boldsymbol{V}_1}{\boldsymbol{I}_1} = -\boldsymbol{Z}_G^2 \frac{\boldsymbol{I}_2}{\boldsymbol{V}_2} = -\boldsymbol{Z}_G^2 \frac{1}{\boldsymbol{Z}_2} \tag{3.80}$$

applies, where the negative sign is related to the definition of the generator sign convention at the input.

Here, too, two-port parameters are particularly convenient. From (3.74) and (3.75), according to Figure 3.13(b),

$$\mathcal{A}_G = \begin{bmatrix} 0 & -\boldsymbol{Z}_G \\ \dfrac{1}{\boldsymbol{Z}_G} & 0 \end{bmatrix} \tag{3.81}$$

and, using (B.4),

$$\mathcal{Z}_G = \begin{bmatrix} 0 & -\boldsymbol{Z}_G \\ \boldsymbol{Z}_G & 0 \end{bmatrix} \,. \tag{3.82}$$

Unlike the complex transformer, the complex gyrator cannot be converted into a conventional gyrator by choosing a suitable gyration impedance. This, too, results from the negation of the input voltage in the generator sign convention.

The conventional gyrator is not reciprocal [44]. The complex gyrator defined here, however, is reciprocal owing to the negation, as $\det \mathcal{A}_G = 1$ confirms directly.

Equivalent Circuit

Using the complex gyrator according to Figure 3.13(b), the equivalent circuit in Figure 3.14(a) follows directly from (3.3).

One advantage of this equivalent circuit over the transformer-based ones is that, as Figure 3.14(b) shows, all voltages and currents of the pair of equations (3.71), or (3.1) and (3.2), are directly accessible.

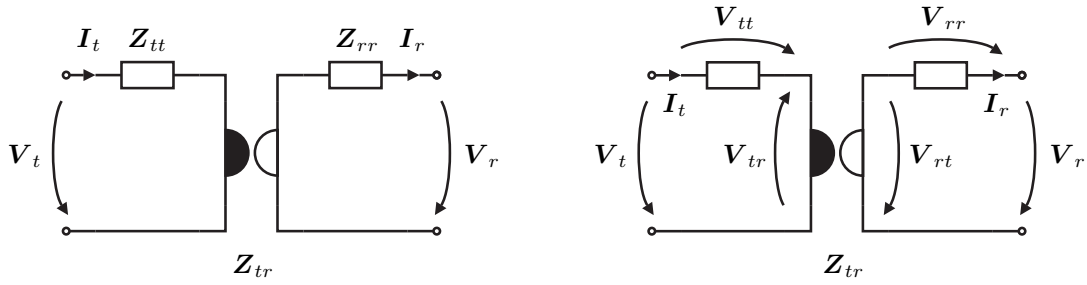

(a) Gyrator equivalent circuit

(b) Reference arrows in the gyrator equivalent circuit

Figure 3.14.: *Equivalent circuit of the transmission system from the Z parameters* (3.3) *using the complex gyrator*

The advantages of the new equivalent circuit in Figure 3.14(a) become particularly clear for transmission systems that are loaded with the optimal load impedance according to Section 3.1 and fed with a source reactance according to Section 3.2. If the loss resistance R_{tr} is neglected, the complex gyrator in Figure 3.14(a) has an imaginary gyration impedance. Furthermore, (3.13) shows that, in this case, the imaginary part of the optimal load impedance $X_{r,\eta}$ should equal the negative of X_{rr}. Similarly, according to (3.51) and (3.41), the source reactance for voltage feed should equal the negative of X_{tt}. If Figure 3.14(a) is extended by these reactances, the reactances at the input and at the output cancel, resulting in the simplified equivalent circuit in Figure 3.15. Since

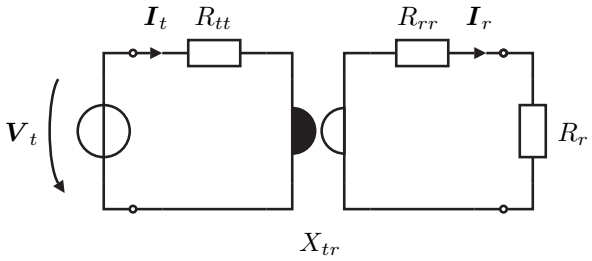

Figure 3.15.: *Equivalent circuit of the transmission system according to Figure 3.14(a) with $R_{tr} = 0$, the load reactance $X_r = X_{r,\eta}$ according to* (3.13)*, and the source reactance $X_t' = -X_t$ according to* (3.51)

the loss resistances R_{tt} and R_{rr} are very small in many cases, this equivalent circuit shows directly that a system with this circuitry behaves approximately like a complex gyrator. With voltage feed, the amplitude of the output current $\boldsymbol{I}_r$ is approximately independent of the load resistance R_r.

For example, [51] describes an inductive system with the same external circuitry, driven by a constant current; in this case, the output behaves approximately like a voltage source. This is just as easily confirmed with Figure 3.15. Moreover, for the special

case of current feed, the equivalent circuit in Figure 3.15 shows directly that a series impedance at the input has no influence on the voltage at the output terminals. With current feed, the current into the input terminals of the complex gyrator is independent of a series impedance, which results in a constant voltage at the output terminals of the gyrator. With the transformer-based equivalent circuits in Figure 3.12, this relationship is considerably more difficult to show.

3.4. Application Examples

This section illustrates the preceding findings with three application examples based on actual transmission systems. The first two examples show how the inductive and capacitive systems derived theoretically in Appendices A.1 and A.2 can be implemented. The third example examines the claim that transmission systems with several inductively coupled coils can generally achieve a higher efficiency than transmission systems with two coupled coils [28, 52].

3.4.1. Example Systems

The preceding sections of this chapter showed which measures enable a known transmission system to transfer a given power from a source to a load with the highest possible efficiency. Most of these sections ended with a design example. These design examples are now combined into two concrete application examples.

Figure 3.16 shows the inductive transmission system determined in Appendix A.1. The gyrator equivalent circuit from Figure 3.14 is used here, because it shows more clearly how the external circuitry affects the transfer behavior. The system is fed by a current source and transfers a power of 10 W. Its transfer quality factor of $Q_k = 7.14$ indicates a maximum possible efficiency of 75.44%.

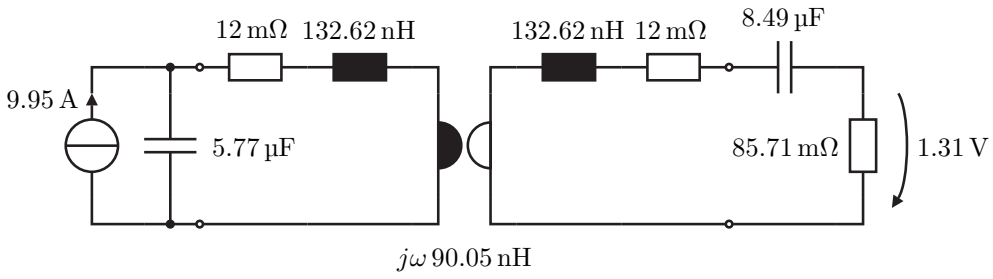

Figure 3.16.: *Application example for the inductive transmission system A.1. Current feed and an output power of* 10 W *were specified.*

When excited at the specified frequency of 150 kHz, the output-side inductance and the output-side capacitance form a series resonant circuit at resonance, so that the two reactances cancel. Hence, the output of the complex gyrator is loaded purely resistively by the series connection of the 12 mΩ and 85.71 mΩ resistances. In this case, (3.80) yields a resistance of 73.72 mΩ at the input terminals of the complex gyrator.

From this resistance, the input impedance of the overall system seen by the current source can be determined. It amounts to 267.98 mΩ and is likewise purely real. Consequently, the current source in Figure 3.16 does not have to supply any reactive power.

The active power drawn from the source can be calculated from the stated peak current and the input impedance. After conversion to an RMS current, an input active power of 13.26 W results, which, together with the specified output active power, corresponds to a power transfer efficiency of 75.44%. This result agrees exactly with the value predicted by the transfer quality factor.

The capacitive transmission system presented in Appendix A.2 behaves similarly. Figure 3.17 shows this example system with voltage feed. As already presented in Section 3.1.1, this transmission system has a considerably higher transfer quality factor of $Q_k = 260.49$ than the inductive system. This yields a maximum efficiency of 99.2%, which can be confirmed with the circuitry shown in Figure 3.17.

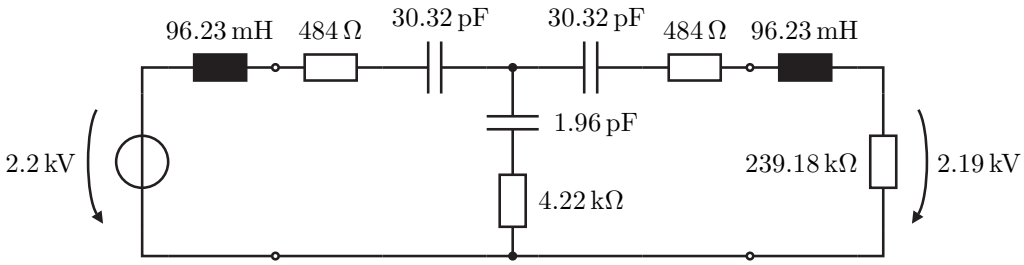

Figure 3.17.: *Application example for the capacitive transmission system A.2. Voltage feed and an output power of* 10 W *were specified.*

With the equivalent circuit chosen in Figure 3.17, it is considerably harder than in Figure 3.16 to see how the circuitry affects the transfer behavior. However, it shows clearly how the comparatively high transfer quality factor is achieved. The two series capacitances of 30.32 pF each are considerably larger than the shunt capacitance of 1.96 pF. This results in a higher reactance of the shunt path. The same applies to the loss resistances shown: the resistance in the shunt path dominates. This results in a comparatively high impedance of the shunt path, which favors current flow directly from the input to the output. Comparing the two equivalent circuits shows that, depending on the task, some of the equivalent circuits from Section 3.3 reveal a particular characteristic more clearly than others.

For completeness, the voltages at the input and output terminals of the transmission systems are calculated. With the values given, Figure 3.16 yields an output terminal voltage of 2.32 V. Figure 3.17 yields a far higher voltage of 2.34 kV at the output terminals. This marked difference is due to the different magnitudes of the elements of the respective impedance matrix (A.35) or (A.77) and thus to the geometry or the turns ratio.

The same can be seen at the input terminals of the two systems. Since the input impedance of the transmission system loaded with $Z_{r,\eta}$ is already known from (3.40) and (3.41), the voltage at the input terminals of the inductive example system can easily be determined to be 2.67 V. For the capacitive example system, the voltage at the input terminals is 2.35 kV. Here, too, the marked difference is due to the magnitudes of the elements of the impedance matrices (A.35) and (A.77).

3.4.2. Multi-Coil System

Since the first publications by the Massachusetts Institute of Technology in 2007 [31], many research groups have been working on inductive transmission systems consisting of more than two coupled coils [28, 52, 53, 54]. Figure 3.18 shows the basic arrangement of such a system, adapted from [31].

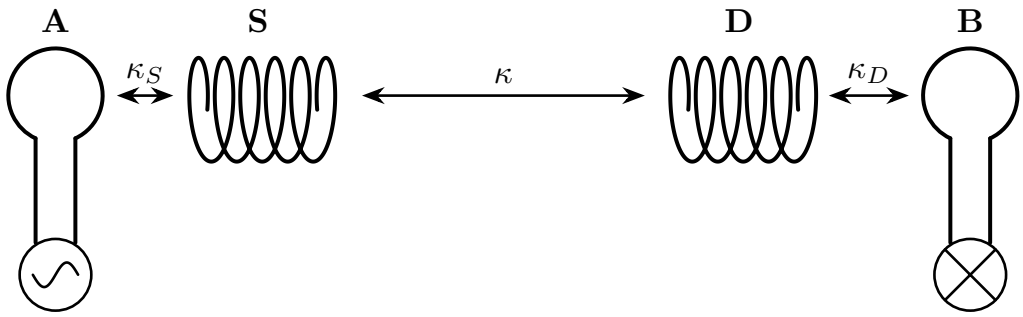

Figure 3.18.: *Transmission system with four coupled coils, own illustration, adapted from [31]*

In greatly simplified terms, this example system works as follows. The transfer distance lies between the transmitting inductance L_S and the receiving inductance L_D. These inductances are coupled by the coupling factor κ according to (A.18), and both are tuned to a common resonant frequency by a discrete [52] or parasitic [28] capacitor C_S or C_D, respectively. To transfer energy, the high-Q resonant circuit on the transmitter side, consisting of L_S and C_S, is excited at its resonant frequency by an additional inductance L_A coupled via the factor κ_S. Because of the high quality factor, this

excitation causes a large current in the transmitting resonant circuit, which, according to Section A.1, generates a high flux density. Across the distance to be bridged, this flux density excites the receiving resonant circuit, consisting of L_D and C_D and tuned to the same resonant frequency, and also induces a current in it. To use the transferred power, energy must be drawn from the receiving resonant circuit. This is done by a fourth inductance L_B, coupled via the coupling factor κ_D. Figure 3.19 shows the corresponding circuit diagram.

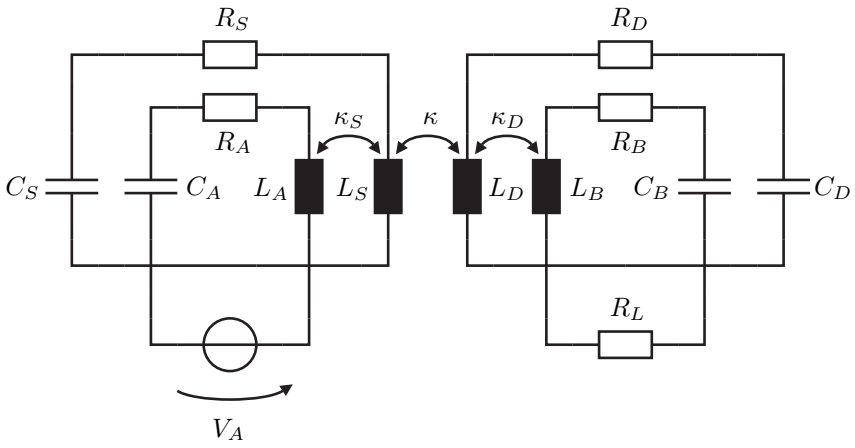

Figure 3.19.: *Circuit diagram of the transmission system with four coupled coils*

Coupling factors between non-adjacent inductances in Figure 3.19 are neglected. [52] gives an example design, whose values are summarized in Table 3.1.

Variable	Value
V_A	10.2 V
f	700 kHz
L_A	15.58 µH
C_A	3.3 nF
R_A	6.15 Ω
κ_S	0.56

Variable	Value
L_S	1099 µH
C_S	47.1 pF
R_S	5.1 Ω
κ	0.05
L_D	29.35 µH
C_D	1.76 nF

Variable	Value
R_D	493 mΩ
κ_D	0.59
L_B	3.56 µH
C_B	14.55 nF
R_B	225 mΩ
R_L	100 Ω

Table 3.1.: *Parameters of the example system determined in [52]*

According to [52] or [28], such multi-coil systems can transfer electrical energy with an efficiency that simple inductive systems with only two coils cannot achieve. Despite the low coupling factor of $\kappa = 0.05$, the circuit in Figure 3.19 with the given values achieves

an efficiency of 89.8%. Following the reasoning of [52], the advantage of this transfer variant is that both the transmitting and the receiving resonant circuits containing L_S and L_D oscillate freely, and the resonant current is not limited by any source or load resistance. According to [52], a transmission system consisting of only two coils achieves an efficiency of approximately 40% in a comparable configuration.

The following examines whether the derivations presented so far confirm this. For this purpose, it is assumed that only the two middle coupled coils from Figure 3.19, with the same coupling factor κ, are available for power transfer. At a frequency of 700 kHz, the given values yield $X_{tt} = 4.83\,\mathrm{k\Omega}$ and $X_{rr} = 129.09\,\Omega$. R_{tt} and R_{rr} can be read directly from Table 3.1: $R_{tt} = 5.1\,\Omega$ and $R_{rr} = 493\,\mathrm{m\Omega}$. Furthermore, $R_{tr} = 0$, and from κ, L_S, L_D, and (A.22) it follows that $X_{tr} = 39.5\,\Omega$. With these values, the transfer quality factor can be determined using (3.25). It is $Q_k = 24.928$. With (3.26), this transfer quality factor shows directly that, despite the low coupling factor, the inner coil pair can transfer energy with an efficiency of 92.3%. This contradicts the claim in [52] that a two-coil transmission system achieves an efficiency of only 40%.

The load impedance required to optimize the efficiency can be calculated from (3.10)–(3.13) and (3.15). This yields an optimal load reactance of $-129.09\,\Omega$, which can be realized by a capacitor of 1.76 nF. This result corresponds to the value given in Table 3.1 for the resonant capacitor C_D. The optimal load resistance is found to be $12.29\,\Omega$. Since the efficiency is independent of the source and the source reactance,

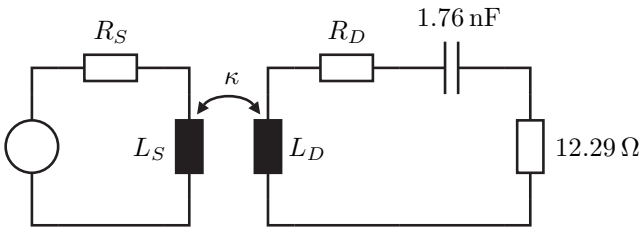

Figure 3.20.: *Optimized transmission system with 2 coupled coils*

Figure 3.20 simply assumes an arbitrary ideal source.

Figure 3.20 confirms that a comparable transmission system consisting of only two inductances can achieve an efficiency of 92.3%. To achieve such a high value, it is essential to choose a load impedance according to Section 3.1. Additional inductances, on the other hand, do not improve the efficiency. On the contrary, in practice they introduce further loss resistances, which reduce the overall efficiency of the power transfer.

4. Matching

Sections 3.1 and 3.2 showed that certain conditions must be met at the input and output to maximize the transferred power and the efficiency. The source and load must therefore be matched to the transmission system. In this context, the preceding application examples in Figures 3.16 and 3.17 showed that very high source voltage or current amplitudes may be required to transfer a given power. At the same time, the load resistances in these examples were in a range rather unusual for power transfer. Since the source and load are often specified by the application, matching [25, 26] is necessary.

There are two ways to achieve optimal power transfer. The first is to adapt the transmission system itself to the available source and load; for inductive power transfer, this means adapting the transmitting and receiving inductances.

If the transmission system cannot be adapted directly, the second option is to add matching networks. Figure 4.1 shows the transmission system together with two additional two-ports for matching the source and the load.

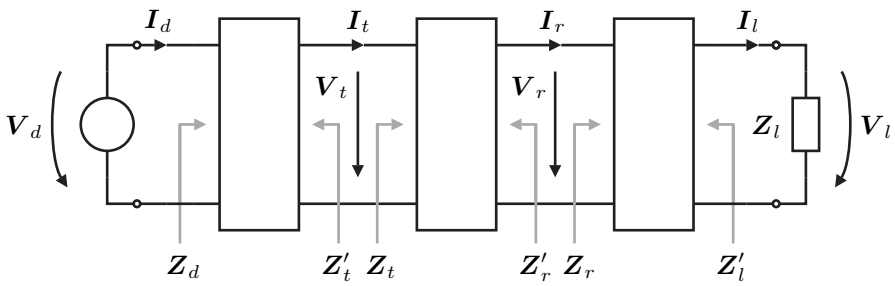

Figure 4.1.: *Matching of source and load to an existing transmission system*

In this way, the available source can be transformed into the required source according to (3.52) or (3.55). The same applies to the load impedance: an additional matching network converts the available load impedance into the required impedance according to (3.16).

In addition to the indices t for transmitter and r for receiver introduced in Figure 3.1, the subscript d denotes the source (driving) quantities, and l denotes the load quantities.

Chain matrices according to Appendix B, starting on page 117, are well suited for describing the coupled two-ports. Their advantage is that the chain matrix of a cascade of two-ports is simply the product of the individual matrices. In Figure 4.1, for example, this means that the system matrix of the overall system can be described by the product

$$\mathcal{A}_{dl} = \mathcal{A}_{dt}\mathcal{A}_{tr}\mathcal{A}_{rl} \; . \tag{4.1}$$

Here, too, the indices indicate the position of the respective two-port.

In many cases, the power receiver requires a DC voltage. Consequently, the transmission or matching systems presented here must be extended by an additional rectifier at the output. Since, according to [22, 55], a rectifier driven by a sinusoidal quantity can be approximated by a resistor, the following sections always assume a resistive load. In principle, however, the procedure shown can also be applied to a general load impedance.

Section 4.1 covers the direct adaptation of the transmission system to a given source and load. Sections 4.2 and 4.3 then show how a given load or source can be matched to an existing transmission system by additional matching networks. Before application examples are given in Section 4.5, Section 4.4 shows how matching affects the transfer quality factor and the transfer bandwidth introduced in the preceding chapter.

4.1. Transmission System Matching

In (3.9), Section 3.1 showed that the efficiency of every transmission system depends on the load resistance R_r. Figure 3.5 and the transfer bandwidth confirmed this. Furthermore, Section 3.2 determined the relationship between the output power and the source voltage (3.52) or source current (3.55). If the transmission system can be modified, it makes sense to match it directly to the source and the load. A distinction is made between matching to a voltage source and to a current source.

4.1.1. Voltage Feed

Figure 4.2 shows a general voltage-fed transmission system. Since the load reactance $X_{r,\eta}$ and the source reactance X_t' according to (3.13) and (3.51) depend on the impedance matrix $\mathcal{Z}_{tr}$ of the transmission system to be determined, specifying the actual load resistance R_l and the source voltage $\boldsymbol{V}_d$ results in a system in which only the elements $\boldsymbol{Z}_{tt}$, $\boldsymbol{Z}_{rr}$, and $\boldsymbol{Z}_{tr}$ of the impedance matrix are unknown. Since each of these impedances generally consists of a real and an imaginary part, this results in a system of equations with six unknowns.

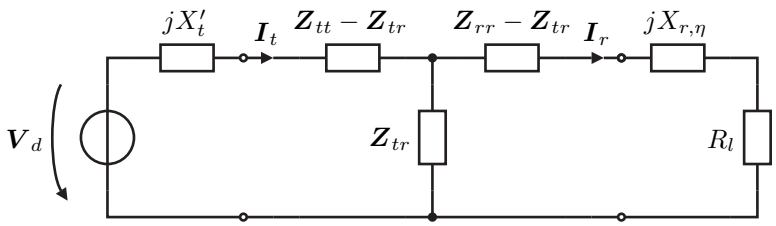

Figure 4.2.: *Voltage-fed transmission system, load impedance as series connection* (3.21)

If the six unknowns can be chosen freely, Figure 4.2 shows directly that, for power transfer, the real parts of the impedances $\boldsymbol{Z}_{tt}$ and $\boldsymbol{Z}_{rr}$ should be as small as possible and the real part of the impedance $\boldsymbol{Z}_{tr}$ as large as possible. In practical implementations, however, the loss resistances often cannot be chosen freely but depend on the corresponding reactances. This dependence can be described by quality factors, which can be defined as

$$Q_{tt} = \frac{X_{tt}}{R_{tt}} \tag{4.2}$$

and

$$Q_{rr} = \frac{X_{rr}}{R_{rr}} \,. \tag{4.3}$$

With this definition, the quality factors can be positive or negative, depending on the type of reactance. They are often approximately known from experience or measurements.

In addition to these quality factors, the coupling between transmitter and receiver can often be estimated from experience. If, for a reciprocal system and by analogy with the general coupling factor (B.13), this coupling is described by a resistive and a reactive coupling factor according to

$$k_R = \frac{R_{tr}}{\sqrt{R_{tt} R_{rr}}} \tag{4.4}$$

and

$$k_X = \frac{X_{tr}}{\sqrt{X_{tt} X_{rr}}} \,, \tag{4.5}$$

the transfer quality factor (3.25) together with (4.2)–(4.5) yields

$$Q_k = \sqrt{\frac{1 + Q_{tt} Q_{rr} k_X^2}{1 - k_R^2}} \,. \tag{4.6}$$

Using (3.26), this means that the efficiency of the power transfer can already be estimated from the four characteristic parameters (4.2)–(4.5). Furthermore, these four

parameters reduce the system of equations to be solved to a system with two unknowns. Rearranging (4.2), (4.3), and (4.4) yields

$$R_{tr} = k_R \sqrt{\frac{X_{tt} X_{rr}}{Q_{tt} Q_{rr}}} \tag{4.7}$$

and using (4.5) gives

$$X_{tr} = k_X \sqrt{X_{tt} X_{rr}} \,. \tag{4.8}$$

The quantities α and β from (3.10) and (3.11) can likewise be expressed in terms of the defined quality factors and the two coupling factors:

$$\alpha = \left(1 + Q_{tt} Q_{rr} k_X^2\right) \frac{X_{rr}}{Q_{rr}} \tag{4.9}$$

and

$$\beta = \left(1 - k_R^2\right) \frac{X_{rr}}{Q_{rr}} \,. \tag{4.10}$$

The transmission system to be determined should transfer energy with maximum efficiency while delivering the maximum power at the output. With the given load resistance R_l, input voltage $\boldsymbol{V}_d$, and specified output power P_r, (3.15) and (3.52) yield the system of equations

$$\begin{aligned} R_l = R_{r,\eta} &= \sqrt{\alpha\beta} \\ |\boldsymbol{V}_d| = |\boldsymbol{V}_t'| &= \frac{X_{tt}}{Q_{tt}} \left(\sqrt{\alpha} + \sqrt{\beta}\right) \sqrt{\frac{2 P_r \sqrt{\alpha} \sqrt{\beta}}{\alpha R_{tr}^2 + \beta X_{tr}^2}} \,. \end{aligned} \tag{4.11}$$

With (4.2)–(4.10), only the two quantities X_{tt} and X_{rr} in (4.11) are unknown. The solution is

$$X_{rr} = R_l \frac{Q_{rr}}{Q_k \left(1 - k_R^2\right)} \tag{4.12}$$

and

$$X_{tt} = \frac{|\boldsymbol{V}_d|^2}{2 P_r} \frac{Q_{tt} Q_k}{\left(Q_k + 1\right)^2 \left(1 - k_R^2\right)} \,. \tag{4.13}$$

Together with (4.2) and (4.3), (4.12) and (4.13) yield the resistances R_{tt} and R_{rr} and, in combination with (4.4) and (4.5), also the impedance $\boldsymbol{Z}_{tr}$. The system is thus fully determined, and the transmission system is matched to the load and the voltage source.

The situation is similar if, according to (3.22) and Figure 4.3, the output is instead terminated by a parallel connection of a reactance and a load resistance.

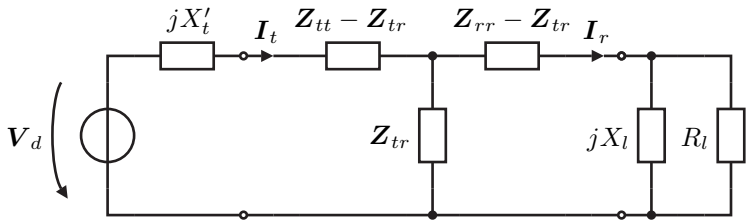

Figure 4.3.: *Voltage-fed transmission system, load impedance as parallel connection* (3.22)

In this case, according to (3.23) and (3.24), with (3.13) rewritten as

$$\gamma = X_{r,\eta} = k_X k_R \frac{Q_{tt}}{X_{tt}} \sqrt{\frac{X_{tt}^2 X_{rr}^2}{Q_{tt} Q_{rr}}} - X_{rr} \tag{4.14}$$

and with (4.2)–(4.8), the system of equations

$$\begin{aligned} R_l &= \frac{R_{r,\eta}^2 + X_{r,\eta}^2}{R_{r,\eta}} = \frac{\alpha\beta + \gamma^2}{\sqrt{\alpha\beta}} \\ X_l &= \frac{R_{r,\eta}^2 + X_{r,\eta}^2}{X_{r,\eta}} = \frac{\alpha\beta + \gamma^2}{\gamma} \\ |\boldsymbol{V}_d| = |\boldsymbol{V}'_t| &= \frac{X_{tt}}{Q_{tt}} \left(\sqrt{\alpha} + \sqrt{\beta}\right) \sqrt{\frac{2P_r\sqrt{\alpha}\sqrt{\beta}}{\alpha R_{tr}^2 + \beta X_{tr}^2}} \end{aligned} \tag{4.15}$$

must be solved. It consists of three equations but, unlike (4.11), also has three unknowns: X_{tt}, X_{rr}, and X_l. Since the analytical result is cumbersome, the equations are best solved numerically. This, too, matches the transmission system to the load.

4.1.2. Current Feed

Figure 4.4 shows a current-fed transmission system. Here, too, the load reactance $X_{r,\eta}$ and the source reactance X'_t are known from (3.13) and (3.54) and depend only on the elements of the impedance matrix of the transmission system to be determined. Analogous to Section 4.1.1, this leads to a system of equations with six unknowns, which, with the assumptions shown there and (4.2)–(4.5), can likewise be reduced to a system with only two unknowns, X_{tt} and X_{rr}.

With the given load resistance R_l, input current $\boldsymbol{I}_d$, and specified output power P_r,

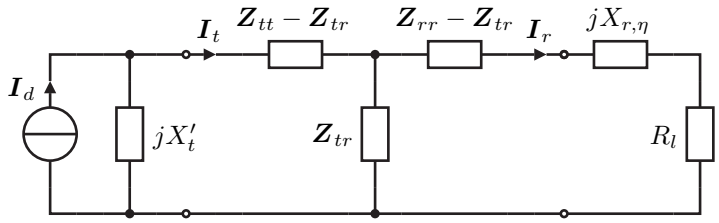

Figure 4.4.: *Current-fed transmission system, load impedance as series connection (3.21)*

(3.15) and (3.55) yield the system of equations

$$\begin{aligned} R_l &= R_{r,\eta} = \sqrt{\alpha\beta} \\ |\boldsymbol{I}_d| &= |\boldsymbol{I}'_t| = \frac{X_{tt}X_{rr}}{Q_{tt}Q_{rr}} \frac{\sqrt{\alpha}+\sqrt{\beta}}{\sqrt{\alpha R_{tr}^2 + \beta X_{tr}^2}} \sqrt{\frac{2P_r\sqrt{\alpha}\sqrt{\beta}}{\left(R_{tr}X_{tr} - \dfrac{X_{tt}X_{rr}}{Q_{rr}}\right)^2 + \alpha\beta\dfrac{X_{tt}^2}{Q_{tt}^2}}}, \end{aligned} \tag{4.16}$$

which can be solved by

$$X_{rr} = R_l \frac{Q_{rr}}{Q_k\left(1-k_R^2\right)} \tag{4.17}$$

and

$$X_{tt} = \frac{2P_r}{|\boldsymbol{I}_d|^2} \frac{Q_{tt}Q_k\left(Q_k+1\right)^2\left(k_R^2-1\right)}{\left(1-Q_k^2\right)\left[Q_k^2\left(k_R^2-1\right)^2 + Q_{tt}^2\left(1 - Q_{rr}k_X k_R\sqrt{\dfrac{1}{Q_{tt}Q_{rr}}}\right)^2\right]}. \tag{4.18}$$

Together with (4.2) and (4.3), (4.17) and (4.18) yield the resistances R_{tt} and R_{rr} and, in combination with (4.4) and (4.5), the impedance $\boldsymbol{Z}_{tr}$. This system is thus also fully determined.

Here, too, the output can alternatively be terminated by a parallel connection of a reactance and a load resistance, as shown in Figure 4.5.

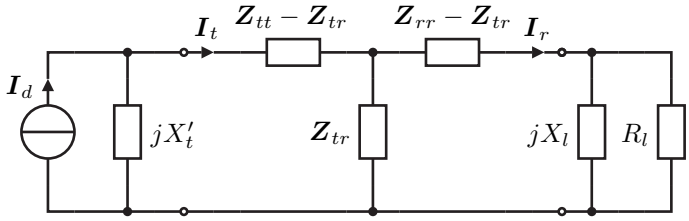

Figure 4.5.: *Current-fed transmission system, load impedance as parallel connection (3.22)*

With (4.14), the system of equations

$$\begin{aligned} R_l &= \frac{R_{r,\eta}^2 + X_{r,\eta}^2}{R_{r,\eta}} = \frac{\alpha\beta + \gamma^2}{\sqrt{\alpha\beta}} \\ X_l &= \frac{R_{r,\eta}^2 + X_{r,\eta}^2}{X_{r,\eta}} = \frac{\alpha\beta + \gamma^2}{\gamma} \\ |\boldsymbol{I}_d| = |\boldsymbol{I}_t'| &= \frac{X_{tt}X_{rr}}{Q_{tt}Q_{rr}} \frac{\sqrt{\alpha} + \sqrt{\beta}}{\sqrt{\alpha R_{tr}^2 + \beta X_{tr}^2}} \sqrt{\frac{2P_r\sqrt{\alpha}\sqrt{\beta}}{\left(R_{tr}X_{tr} - \frac{X_{tt}X_{rr}}{Q_{rr}}\right)^2 + \alpha\beta\frac{X_{tt}^2}{Q_{tt}^2}}} \end{aligned} \tag{4.19}$$

with the three unknowns X_{tt}, X_{rr}, and X_l follows, which, like (4.15), can be solved numerically. This makes it possible to match the transmission system to a current source and a defined load.

4.2. Load Matching

If the transmission system cannot be adapted directly to the actual load resistance according to Section 4.1, maximum-efficiency power transfer can still be achieved with an additional matching network at the output. Figure 4.6 shows the output of the transmission system from Figure 3.1, connected to the load resistance R_l through a matching network that is yet to be determined.

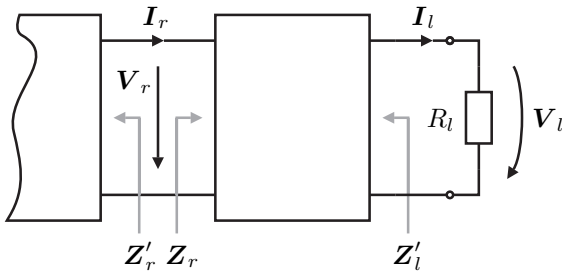

Figure 4.6.: *Matching the load to the given transmission system*

There are several ways to perform this matching. The following sections present matching with a complex transformer (Section 3.3.1) and with a complex gyrator (Section 3.3.2). The goal is a load-matching chain matrix $\mathcal{A}_{rl}$ that can be realized as a lossless circuit according to Appendix B.2. Realizable here means that the matching network consists of discrete components; since it must be lossless, only inductors and capacitors may be used.

4.2.1. Transformer-Based Series Load Matching

Section 3.1 showed that, to maximize the efficiency, the input impedance $\boldsymbol{Z}_r$ of the matching network should be chosen equal to the optimal load impedance $\boldsymbol{Z}_{r,\eta}$. According to (3.21), this input impedance can be realized by the series connection of a reactance and a resistor. Since, in the general case, the load resistance R_l in Figure 4.6 does not equal the ideal load resistance, it is transformed into the optimal resistance $R_{r,\eta}$ by a complex transformer according to Section 3.3.1. From (3.66), the required turns ratio of the complex transformer is

$$\boldsymbol{n}_{1,2} = \pm\sqrt{\frac{R_l}{R_{r,\eta}}}\,. \tag{4.20}$$

This turns ratio is real, and the complex transformer behaves like an ideal transformer. Because of the squaring in (3.66), however, the positive and negative signs must be considered separately. As a result, there are two matching networks that provide transformer-based series load matching.

These considerations lead to the network in Figure 4.7, from which, using (3.67), the

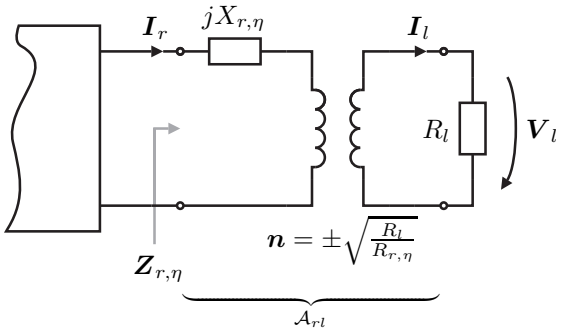

Figure 4.7.: *Network for transformer-based series load matching*

chain matrices of the required matching networks follow as

$$\mathcal{A}_{rl_{1,2}} = \begin{bmatrix} 1 & jX_{r,\eta} \\ 0 & 1 \end{bmatrix} \begin{bmatrix} \pm\sqrt{\dfrac{R_{r,\eta}}{R_l}} & 0 \\ 0 & \pm\sqrt{\dfrac{R_l}{R_{r,\eta}}} \end{bmatrix} = \begin{bmatrix} \pm\sqrt{\dfrac{R_{r,\eta}}{R_l}} & \pm jX_{r,\eta}\sqrt{\dfrac{R_l}{R_{r,\eta}}} \\ 0 & \pm\sqrt{\dfrac{R_l}{R_{r,\eta}}} \end{bmatrix}. \tag{4.21}$$

Since $\boldsymbol{a}_{2,1} = 0$, comparison with (B.21) shows directly that matching networks with the two-port parameters (4.21) can only be realized as Π networks according to Ap-

pendix B.2.2. From (4.21) and (B.23), the vectors

$$\vec{\boldsymbol{Z}}_{\Pi_{1,2}} = \begin{bmatrix} jX_{r,\eta}\dfrac{\sqrt{R_l}}{\sqrt{R_l} \mp \sqrt{R_{r,\eta}}} \\ \pm jX_{r,\eta}\sqrt{\dfrac{R_l}{R_{r,\eta}}} \\ \mp jX_{r,\eta}\dfrac{R_l}{R_{r,\eta}}\dfrac{\sqrt{R_{r,\eta}}}{\sqrt{R_l} \mp \sqrt{R_{r,\eta}}} \end{bmatrix} \tag{4.22}$$

and Figure 4.8 follow. Transformer-based load matching can therefore be realized

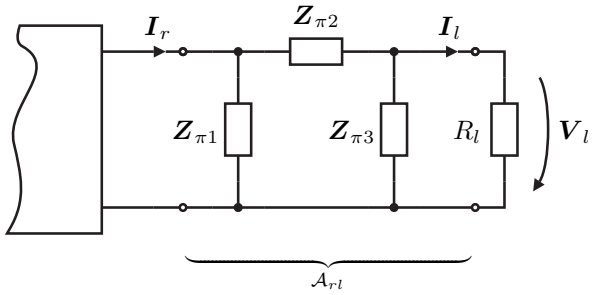

Figure 4.8.: *Load matching with a* Π *network*

with two Π networks. The impedances in (4.22) are purely reactive, so the matching networks can be built in practice.

4.2.2. Gyrator-Based Series Load Matching

In gyrator-based series load matching, too, the input impedance of the matching network must equal the impedance $\boldsymbol{Z}_{r,\eta}$ to maximize the efficiency. With the same reasoning as in Section 4.2.1, (3.80) yields the gyration impedance required to transform the load resistance:

$$\boldsymbol{Z}_{G_{1,2}} = \pm j\sqrt{R_l R_{r,\eta}}\,. \tag{4.23}$$

This gyration impedance is purely imaginary. Here, too, the positive and negative signs must be considered separately. It can be shown that the following analysis would not work with an ideal gyrator, whose chain matrix is known, for example, from [56]; negative resistances would be required.

The gyration impedances (4.23) lead to the network in Figure 4.9.

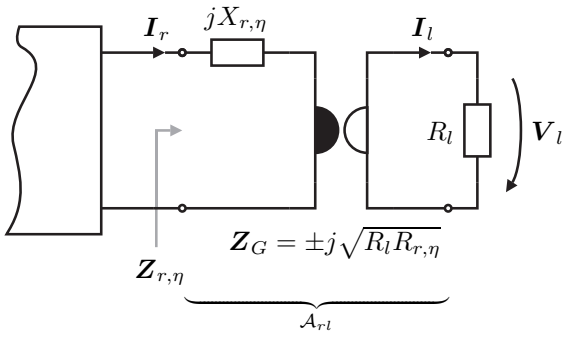

Figure 4.9.: *Network for gyrator-based series load matching*

From this figure, the required chain matrices of the matching networks can be calculated using (3.81):

$$\begin{aligned}\mathcal{A}_{rl_{1,2}} &= \begin{bmatrix} 1 & jX_{r,\eta} \\ 0 & 1 \end{bmatrix} \begin{bmatrix} 0 & \mp j\sqrt{R_l R_{r,\eta}} \\ \pm\dfrac{1}{j\sqrt{R_l R_{r,\eta}}} & 0 \end{bmatrix} \\ \mathcal{A}_{rl_{1,2}} &= \begin{bmatrix} \pm\dfrac{X_{r,\eta}}{\sqrt{R_l R_{r,\eta}}} & \mp j\sqrt{R_l R_{r,\eta}} \\ \pm\dfrac{1}{j\sqrt{R_l R_{r,\eta}}} & 0 \end{bmatrix}.\end{aligned} \tag{4.24}$$

Comparison with (B.21) or (B.23) shows that, here, matching networks with the two-port parameters (4.24) can be realized both as T networks and as Π networks. The vectors

$$\vec{\boldsymbol{Z}}_{T_{1,2}} = \begin{bmatrix} j\left(X_{r,\eta} \mp \sqrt{R_l R_{r,\eta}}\right) \\ \pm j\sqrt{R_l R_{r,\eta}} \\ \mp j\sqrt{R_l R_{r,\eta}} \end{bmatrix} \tag{4.25}$$

and

$$\vec{\boldsymbol{Z}}_{\Pi_{1,2}} = \begin{bmatrix} \pm j\sqrt{R_l R_{r,\eta}} \\ \mp j\sqrt{R_l R_{r,\eta}} \\ -j\dfrac{R_l R_{r,\eta}}{X_{r,\eta} \mp \sqrt{R_l R_{r,\eta}}} \end{bmatrix} \tag{4.26}$$

follow. Gyrator-based series load matching is therefore possible with two T and two Π networks. Again, the impedances are purely reactive, and the matching networks can be built in practice.

Matching with a T network according to (4.25) is shown in Figure 4.10.

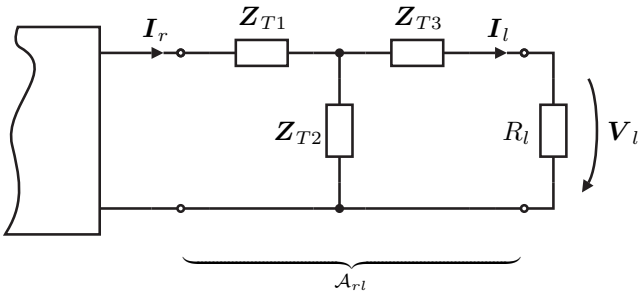

Figure 4.10.: *Load matching with a T network*

Matching with a Π network according to (4.26) uses the network already shown in Figure 4.8.

4.2.3. Transformer-Based Parallel Load Matching

In transformer-based parallel load matching, the input impedance $\boldsymbol{Z}_{r,\eta}$ required for load matching must be realized, according to (3.22), by a parallel connection of the reactance (3.24) and the resistance (3.23). Since, here too, the load resistance R_l in Figure 4.6 generally does not equal the required parallel load resistance according to (3.23), it is transformed by a complex transformer. From (3.66) and (3.23), the required turns ratio is

$$\boldsymbol{n}_{1,2} = \pm\sqrt{\frac{R_{r,\eta}}{X_{r,\eta}^2 + R_{r,\eta}^2} R_l}\,. \tag{4.27}$$

This ratio is real, and the complex transformer behaves like an ideal transformer. Here, too, the positive and negative signs must be considered separately. The resulting network is shown in Figure 4.11.

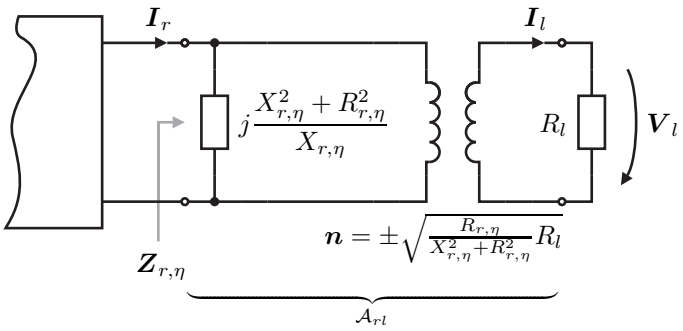

Figure 4.11.: *Network for transformer-based parallel load matching*

The chain matrices of the required matching networks can be read from Figure 4.11:

$$\mathcal{A}_{rl_{1,2}} = \begin{bmatrix} 1 & 0 \\ -j\dfrac{X_{r,\eta}}{R_{r,\eta}^2+X_{r,\eta}^2} & 1 \end{bmatrix} \begin{bmatrix} \pm\sqrt{\dfrac{R_{r,\eta}^2+X_{r,\eta}^2}{R_{r,\eta}}\dfrac{1}{R_l}} & 0 \\ 0 & \pm\sqrt{\dfrac{R_{r,\eta}}{R_{r,\eta}^2+X_{r,\eta}^2}R_l} \end{bmatrix}$$

$$\mathcal{A}_{rl_{1,2}} = \begin{bmatrix} \pm\sqrt{\dfrac{R_{r,\eta}^2+X_{r,\eta}^2}{R_{r,\eta}}\dfrac{1}{R_l}} & 0 \\ \mp j\dfrac{X_{r,\eta}}{R_{r,\eta}^2+X_{r,\eta}^2}\sqrt{\dfrac{R_{r,\eta}^2+X_{r,\eta}^2}{R_{r,\eta}}\dfrac{1}{R_l}} & \pm\sqrt{\dfrac{R_{r,\eta}}{R_{r,\eta}^2+X_{r,\eta}^2}R_l} \end{bmatrix}. \tag{4.28}$$

Since $\boldsymbol{a}_{1,2} = 0$ in (4.28), comparison with (B.23) shows that these matching networks can only be synthesized as T networks according to Figure 4.10. From (B.21), the vectors

$$\vec{\boldsymbol{Z}}_{T_{1,2}} = \begin{bmatrix} j\dfrac{R_{r,\eta}^2+X_{r,\eta}^2}{X_{r,\eta}}\left(1\mp\sqrt{\dfrac{R_{r,\eta}}{R_{r,\eta}^2+X_{r,\eta}^2}R_l}\right) \\ \pm j\dfrac{R_{r,\eta}^2+X_{r,\eta}^2}{X_{r,\eta}}\sqrt{\dfrac{R_{r,\eta}}{R_{r,\eta}^2+X_{r,\eta}^2}R_l} \\ jR_l\dfrac{R_{r,\eta}}{X_{r,\eta}}\left(1\mp\sqrt{\dfrac{R_{r,\eta}^2+X_{r,\eta}^2}{R_{r,\eta}}\dfrac{1}{R_l}}\right) \end{bmatrix} \tag{4.29}$$

follow. The impedances are purely reactive, so the matching networks can be built with discrete reactive components.

4.2.4. Gyrator-Based Parallel Load Matching

The input impedance of the matching network, consisting of a parallel connection of the reactance (3.24) and the resistance (3.23), must equal the impedance $\boldsymbol{Z}_{r,\eta}$. In general, the load resistance R_l must be transformed to (3.23), which can be done with a complex gyrator:

$$\boldsymbol{Z}_{G_{1,2}} = \pm j\sqrt{\frac{R_{r,\eta}^2 + X_{r,\eta}^2}{R_{r,\eta}} R_l}\ . \tag{4.30}$$

The gyration impedance (4.30) is purely imaginary and, as with all previous variants, both signs must be considered separately. Analogous to Section 4.2.3, the complex gyrator leads to the network in Figure 4.12.

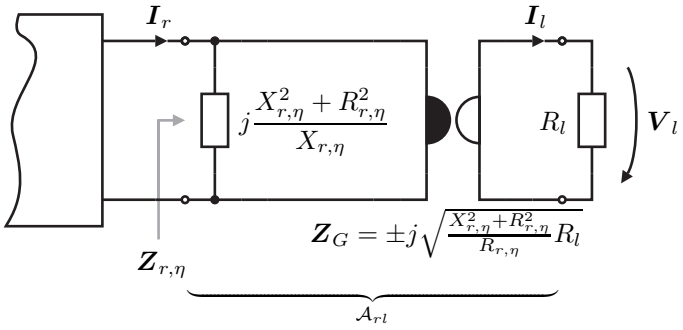

Figure 4.12.: *Network for gyrator-based parallel load matching*

Here, too, the chain matrices of the required matching networks can be read directly from Figure 4.12:

$$\begin{aligned}
\mathcal{A}_{rl_{1,2}} &= \begin{bmatrix} 1 & 0 \\ -j\dfrac{X_{r,\eta}}{R_{r,\eta}^2 + X_{r,\eta}^2} & 1 \end{bmatrix} \begin{bmatrix} 0 & \mp j\sqrt{\dfrac{R_{r,\eta}^2 + X_{r,\eta}^2}{R_{r,\eta}} R_l} \\ \mp j\sqrt{\dfrac{R_{r,\eta}}{R_{r,\eta}^2 + X_{r,\eta}^2}\dfrac{1}{R_l}} & 0 \end{bmatrix} \\
\mathcal{A}_{rl_{1,2}} &= \begin{bmatrix} 0 & \mp j\sqrt{\dfrac{R_{r,\eta}^2 + X_{r,\eta}^2}{R_{r,\eta}} R_l} \\ \mp j\sqrt{\dfrac{R_{r,\eta}}{R_{r,\eta}^2 + X_{r,\eta}^2}\dfrac{1}{R_l}} & \mp\dfrac{X_{r,\eta}}{R_{r,\eta}^2 + X_{r,\eta}^2}\sqrt{\dfrac{R_{r,\eta}^2 + X_{r,\eta}^2}{R_{r,\eta}} R_l} \end{bmatrix}\ .
\end{aligned} \tag{4.31}$$

As with gyrator-based series load matching in Section 4.2.2, synthesis is possible here with both T and Π networks. For the T network according to Figure 4.10, the vectors

are

$$\vec{\boldsymbol{Z}}_{T_{1,2}} = \begin{bmatrix} \mp j\sqrt{\dfrac{R_{r,\eta}^2 + X_{r,\eta}^2}{R_{r,\eta}} R_l} \\ \pm j\sqrt{\dfrac{R_{r,\eta}^2 + X_{r,\eta}^2}{R_{r,\eta}} R_l} \\ -j\left[X_{r,\eta}\dfrac{R_l}{R_{r,\eta}} \pm \sqrt{\dfrac{R_{r,\eta}^2 + X_{r,\eta}^2}{R_{r,\eta}} R_l}\right] \end{bmatrix} . \tag{4.32}$$

Matching with Π networks according to Figure 4.8 is possible with the vectors

$$\vec{\boldsymbol{Z}}_{\Pi_{1,2}} = \begin{bmatrix} \pm j\dfrac{1}{\sqrt{\dfrac{R_{r,\eta}}{R_{r,\eta}^2 + X_{r,\eta}^2}\dfrac{1}{R_l}} \pm \dfrac{X_{r,\eta}}{R_{r,\eta}^2 + X_{r,\eta}^2}} \\ \mp j\sqrt{\dfrac{R_{r,\eta}^2 + X_{r,\eta}^2}{R_{r,\eta}} R_l} \\ \pm j\sqrt{\dfrac{R_{r,\eta}^2 + X_{r,\eta}^2}{R_{r,\eta}} R_l} \end{bmatrix} . \tag{4.33}$$

Here, too, the vectors (4.32) and (4.33) are purely reactive, so the matching networks can be built with discrete components.

Counting both sign cases, this last derivation completes a set of twelve different load-matching networks. A comparison of these networks is beyond the scope of this thesis.

4.3. Source Matching

If the transmission system cannot be adapted directly to the available source according to Section 4.1, maximum power transfer, as discussed in Section 3.2, can still be achieved with an additional matching network at the input. Figure 4.13 shows an arbitrary source connected to the input of the transmission system from Figure 3.1 through a matching network that is yet to be determined.

As in Section 4.2, there are many ways to perform this matching. The following sections present source matching with a complex transformer and with a complex gyrator. Each can be combined with voltage feed or current feed (Sections 3.2.2 and 3.2.3), which yields four matching options.

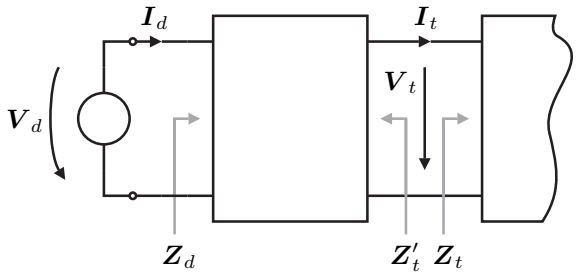

Figure 4.13.: *Matching the source to the given transmission system*

Note that the terms voltage feed and current feed describe the source behavior at the input of the transmission system itself. The source that actually drives the matching network may behave differently, particularly with gyrator-based matching.

As in Section 4.2, care is taken to ensure that the matching networks can be realized with real components.

4.3.1. Transformer-Based Voltage Feed

According to (3.56), the output terminals of a complex transformer behave like a voltage source when a constant voltage is applied to its input. Consequently, for a voltage-fed transmission system, the matching network must also be driven by a voltage source. From (3.56), the required turns ratio is

$$\boldsymbol{n} = \frac{\boldsymbol{V}'_t}{\boldsymbol{V}_d} \,. \tag{4.34}$$

Section 3.2.2 showed that, to maximize the transferred power with voltage feed, the source must have a source reactance according to (3.51). This leads to the matching network in Figure 4.14. From this figure, the chain matrix of the matching network

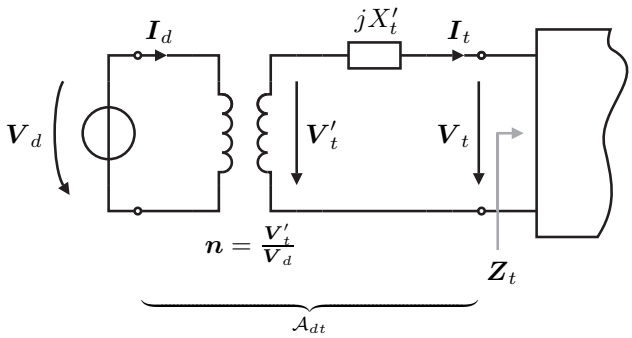

Figure 4.14.: *Transformer-based voltage feed*

can be calculated. With (3.67) and (3.51),

$$\mathcal{A}_{dt} = \begin{bmatrix} \frac{1}{\boldsymbol{n}} & 0 \\ 0 & \boldsymbol{n} \end{bmatrix} \begin{bmatrix} 1 & jX'_t \\ 0 & 1 \end{bmatrix} = \begin{bmatrix} \frac{1}{\boldsymbol{n}} & jX'_t\frac{1}{\boldsymbol{n}} \\ 0 & \boldsymbol{n} \end{bmatrix} . \tag{4.35}$$

Since $\boldsymbol{a}_{2,1} = 0$, (B.21) shows directly that a matching network with the two-port parameters (4.35) can only be built as a Π network according to Section B.2.2. The vector

$$\vec{\boldsymbol{Z}}_{\Pi} = \begin{bmatrix} jX'_t\frac{1}{\boldsymbol{n}\,(\boldsymbol{n}-1)} \\ jX'_t\frac{1}{\boldsymbol{n}} \\ -jX'_t\frac{1}{\boldsymbol{n}-1} \end{bmatrix} \tag{4.36}$$

follows. This vector shows that the Π network can only be built if all three impedances in (4.36) can be realized in practice. This is only the case if the turns ratio $\boldsymbol{n}$ in (4.36) is real. From (4.34) it follows that, in this case, the input voltage $\boldsymbol{V}_d$ must be in phase or in antiphase with the voltage $\boldsymbol{V}'_t$. (4.34) simplifies to

$$\boldsymbol{n}_{1,2} = \pm\frac{|\boldsymbol{V}'_t|}{|\boldsymbol{V}_d|} . \tag{4.37}$$

The complex transformer thus behaves like an ideal transformer. Substituting (4.37) into (4.36) yields two networks according to Figure 4.15 that enable transformer-based voltage feed.

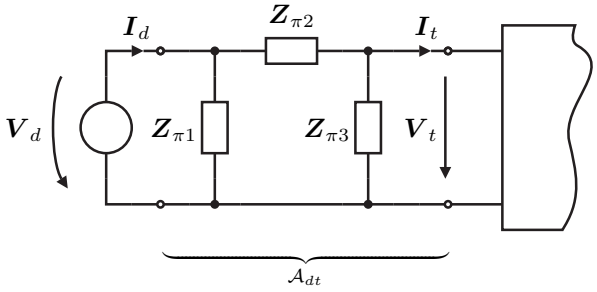

Figure 4.15.: *Source matching with a* Π *network*

4.3.2. Gyrator-Based Voltage Feed

According to (3.75), the output terminals of a complex gyrator behave like a voltage source when a constant current is injected at its input. Consequently, for a voltage-fed

transmission system, the matching network must be driven by a current source. From (3.75), the required gyration impedance is

$$\boldsymbol{Z}_G = \frac{\boldsymbol{V}'_t}{\boldsymbol{I}_d} \,. \tag{4.38}$$

Again, the source must have a source reactance according to (3.51) to maximize the transferred power. This leads to the matching network in Figure 4.16. From this figure,

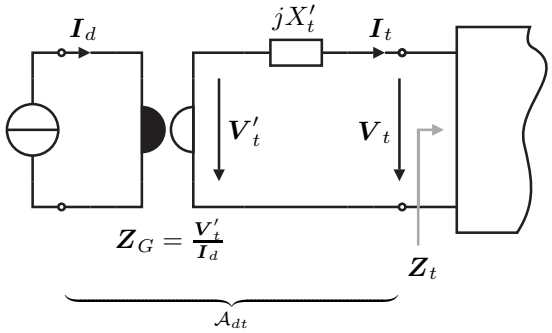

Figure 4.16.: *Gyrator-based voltage feed*

the chain matrix of the matching network can be calculated. With (3.81) and (3.51),

$$\mathcal{A}_{dt} = \begin{bmatrix} 0 & -\boldsymbol{Z}_G \\ \dfrac{1}{\boldsymbol{Z}_G} & 0 \end{bmatrix} \begin{bmatrix} 1 & jX'_t \\ 0 & 1 \end{bmatrix} = \begin{bmatrix} 0 & -\boldsymbol{Z}_G \\ \dfrac{1}{\boldsymbol{Z}_G} & jX'_t \dfrac{1}{\boldsymbol{Z}_G} \end{bmatrix} \,. \tag{4.39}$$

According to (B.21) and (B.23), (4.39) can be built both as a T network and as a Π network. The vectors

$$\vec{\boldsymbol{Z}}_T = \begin{bmatrix} -\boldsymbol{Z}_G \\ \boldsymbol{Z}_G \\ -\left(\boldsymbol{Z}_G - jX'_t\right) \end{bmatrix} \tag{4.40}$$

and

$$\vec{\boldsymbol{Z}}_\Pi = \begin{bmatrix} \boldsymbol{Z}_G^2 \dfrac{\boldsymbol{Z}_G + jX'_t}{X_t'^2 + \boldsymbol{Z}_G^2} \\ -\boldsymbol{Z}_G \\ \boldsymbol{Z}_G \end{bmatrix} \tag{4.41}$$

follow. Analogous to Section 4.3.1, the impedances in (4.40) and (4.41) must also be physically realizable. For both vectors, this is only possible with a purely imaginary

gyration impedance, so that (4.38) simplifies to

$$\boldsymbol{Z}_{G_{1,2}} = \pm j \frac{|\boldsymbol{V}_t'|}{|\boldsymbol{I}_d|} \,. \tag{4.42}$$

Substituting (4.42) into (4.40) or (4.41) yields four practical networks for gyrator-based voltage feed. Matching with a T network is shown in Figure 4.17. Source matching with a Π network was already shown in Figure 4.15.

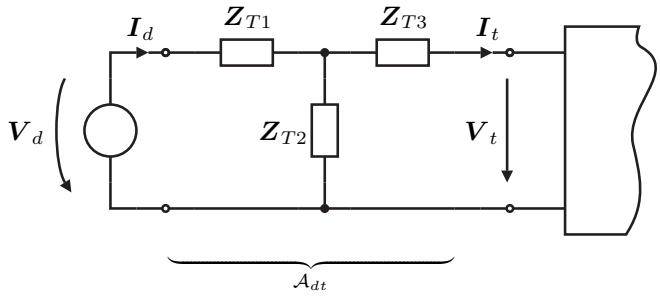

Figure 4.17.: *Source matching with a T network*

4.3.3. Transformer-Based Current Feed

As shown in Section 4.3.1, the output terminals of a complex transformer behave like a voltage source when a constant voltage is applied. For the output terminals to behave like a current source, the transformer must, according to (3.57), itself be driven by a current source. With (3.55),

$$\boldsymbol{n} = \frac{\boldsymbol{I}_d}{\boldsymbol{I}_t'} \,. \tag{4.43}$$

To maximize the output power, this current source must have a source reactance according to (3.54). This leads to the network in Figure 4.18. Here, too, the required chain matrix of the matching network can be read from Figure 4.18:

$$\mathcal{A}_{dt} = \begin{bmatrix} \frac{1}{\boldsymbol{n}} & 0 \\ 0 & \boldsymbol{n} \end{bmatrix} \begin{bmatrix} 1 & 0 \\ \frac{1}{jX_t'} & 1 \end{bmatrix} = \begin{bmatrix} \frac{1}{\boldsymbol{n}} & 0 \\ \boldsymbol{n}\frac{1}{jX_t'} & \boldsymbol{n} \end{bmatrix} \,. \tag{4.44}$$

Since $a_{1,2} = 0$, comparison with (B.23) shows that this matching can only be realized

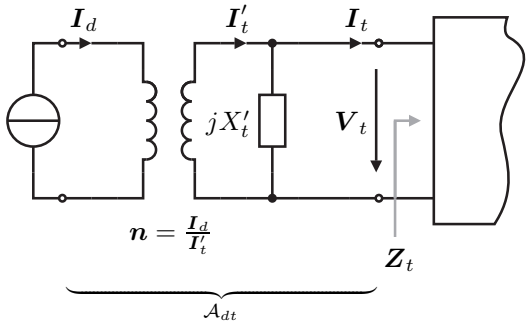

Figure 4.18.: *Transformer-based current feed*

with a T network. From (4.44) and (B.21), the vector

$$\vec{\boldsymbol{Z}}_T = \begin{bmatrix} -jX'_t \dfrac{\boldsymbol{n}-1}{\boldsymbol{n}^2} \\ jX'_t \dfrac{1}{\boldsymbol{n}} \\ jX'_t \dfrac{\boldsymbol{n}-1}{\boldsymbol{n}} \end{bmatrix} \tag{4.45}$$

follows. As in Section 4.3.1, (4.45) shows directly that the individual impedances of the T network can be replaced by reactances if the turns ratio is real. Analogous to (4.37), (3.57) yields the turns ratio

$$\boldsymbol{n}_{1,2} = \pm \frac{|\boldsymbol{I}_d|}{|\boldsymbol{I}'_t|} \,. \tag{4.46}$$

Substituting (4.46) into (4.45) yields two practical networks according to Figure 4.17 for transformer-based current feed.

4.3.4. Gyrator-Based Current Feed

For the output terminals of the complex gyrator to behave like a current source, the matching network must be driven by a voltage source. From (3.74) and (3.55), the gyration impedance is

$$\boldsymbol{Z}_G = \frac{\boldsymbol{V}_d}{\boldsymbol{I}'_t} \,. \tag{4.47}$$

The source reactance that maximizes the output power is again given by (3.54), which leads to the matching network in Figure 4.19. From this figure, the chain matrix of

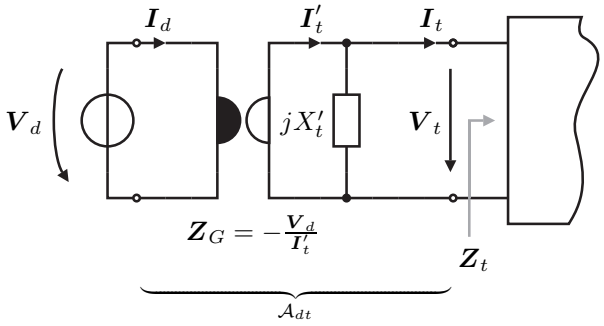

Figure 4.19.: *Gyrator-based current feed*

the matching network is

$$\mathcal{A}_{dt} = \begin{bmatrix} 0 & -\boldsymbol{Z}_G \\ \dfrac{1}{\boldsymbol{Z}_G} & 0 \end{bmatrix} \begin{bmatrix} 1 & 0 \\ \dfrac{1}{jX'_t} & 1 \end{bmatrix} = \begin{bmatrix} -\dfrac{\boldsymbol{Z}_G}{jX'_t} & -\boldsymbol{Z}_G \\ \dfrac{1}{\boldsymbol{Z}_G} & 0 \end{bmatrix} , \tag{4.48}$$

from which the two vectors

$$\vec{\boldsymbol{Z}}_T = \begin{bmatrix} -\left(\boldsymbol{Z}_G + \dfrac{\boldsymbol{Z}_G^2}{jX'_t}\right) \\ \boldsymbol{Z}_G \\ -\boldsymbol{Z}_G \end{bmatrix} \tag{4.49}$$

and

$$\vec{\boldsymbol{Z}}_\Pi = \begin{bmatrix} \boldsymbol{Z}_G \\ -\boldsymbol{Z}_G \\ jX'_t\boldsymbol{Z}_G\dfrac{\boldsymbol{Z}_G - jX'_t}{\boldsymbol{Z}_G^2 + X_t'^2} \end{bmatrix} \tag{4.50}$$

follow according to (B.21) and (B.23), respectively. As in Section 4.3.2, these vectors show that both the T and the Π network can only be realized in practice if the gyration impedance is purely imaginary:

$$\boldsymbol{Z}_{G_{1,2}} = \pm j\frac{|\boldsymbol{V}_d|}{|\boldsymbol{I}'_t|} . \tag{4.51}$$

Substituting (4.51) into (4.49) and (4.50) yields, with Figures 4.17 and 4.15, four matching networks that provide gyrator-based current feed.

As with load matching, a total of twelve source-matching networks have been found. A comparison of these networks is left to future work.

4.4. Transfer Quality Factor and Transfer Bandwidth

The transmission system is characterized, among other things, by the quantities α and β. These quantities describe the maximum possible efficiency (3.26), the transfer bandwidth (3.32), and also the optimal real part of the load impedance (3.15). This section shows how the matching networks presented above affect α and β. To represent a general lossless, reciprocal matching network, its impedance matrix is defined as follows. Because the network is lossless, the matrix can be written with $\boldsymbol{z} = r + jx$ as

$$\mathcal{Z}_A = \begin{bmatrix} jx_{1,1} & -jx_{1,2} \\ jx_{1,2} & -jx_{2,2} \end{bmatrix} , \tag{4.52}$$

where the quantities $x_{1,1}$, $x_{1,2}$, and $x_{2,2}$ are real. According to Figures 4.6 and 4.13, this general matching network can be placed either upstream or downstream of the transmission system, which corresponds to general source or load matching. For this purpose, it is convenient to convert the impedance matrix (4.52) into a chain matrix. Using (B.3),

$$\mathcal{A}_A = \begin{bmatrix} \dfrac{x_{1,1}}{x_{1,2}} & j\dfrac{\det \mathcal{Z}_A}{x_{1,2}} \\ -j\dfrac{1}{x_{1,2}} & \dfrac{x_{2,2}}{x_{1,2}} \end{bmatrix} . \tag{4.53}$$

With (4.53), the chain matrix of the general source matching combined with the transmission system is

$$\mathcal{A}_{dr} = \mathcal{A}_A \mathcal{A}_{tr} \tag{4.54}$$

and that of the transmission system combined with the general load matching is

$$\mathcal{A}_{tl} = \mathcal{A}_{tr} \mathcal{A}_A . \tag{4.55}$$

Section 3.1 already showed that the efficiency of a transmission system can only be optimized through the choice of load impedance. It follows directly that the transfer quality factor introduced in Section 3.1.1 and, via (3.33), the transfer bandwidth presented in Section 3.1.2 are independent of any source matching upstream of the transmission system. By transforming (4.54) back into an impedance matrix (B.4), it can be shown that, for lossless source matching,

$$\alpha_{dr} = \alpha \tag{4.56}$$

and

$$\beta_{dr} = \beta . \tag{4.57}$$

This confirms that source matching has no influence on the transfer quality factor (3.25).

The load matching from Section 4.2 behaves similarly. Section 3.1 showed that the efficiency depends on the load impedance $\boldsymbol{Z}_r$, which, with load matching, is the input impedance of the matching network. It can easily be shown that, after transforming (4.55) back into an impedance matrix,

$$\alpha_{tl} = \delta\alpha \tag{4.58}$$

and

$$\beta_{tl} = \delta\beta \tag{4.59}$$

follow, where in both cases δ is given by

$$\delta = \frac{x_{1,2}^2}{x_{1,1}^2 - X_{rr}^2 - 2\gamma\left(X_{rr} + x_{1,1}\right) + R_{rr}\left(\alpha + \beta\right) - R_{rr}^2} \,. \tag{4.60}$$

This shows that lossless load matching generally scales the quantities α and β by the same factor. For the transfer quality factor of the matched system, (3.25) gives

$$Q_{k_{tl}} = \sqrt{\frac{\alpha_{tl}}{\beta_{tl}}} = \sqrt{\frac{\delta\alpha}{\delta\beta}} = \sqrt{\frac{\alpha}{\beta}} = Q_k \,. \tag{4.61}$$

The factor δ in (4.61) cancels, so the transfer quality factor and, via (3.33), the transfer bandwidth are independent of load matching. Consequently, the maximum achievable efficiency of the losslessly matched system remains the same. For the optimal real part of the load impedance of the matched system, $R_{l,\eta}$, (3.15) yields

$$R_{l,\eta} = \sqrt{\alpha_{tl}\beta_{tl}} = \sqrt{\delta\alpha\delta\beta} = \delta\sqrt{\alpha\beta} = \delta R_{r,\eta} \,, \tag{4.62}$$

according to which $R_{r,\eta}$ is also scaled by the factor (4.60), as already confirmed for α and β with (4.58) and (4.59). These relationships already suggest that lossless load matching merely shifts the efficiency curve versus load resistance from Figure 3.5.

This assumption can be confirmed with (3.14). If the matched system is also terminated with its system-dependent optimal reactance $X_{l,\eta}$ but a variable load resistance, the efficiency is

$$\eta_{tl} = \frac{\alpha_{tl}}{\alpha_{tl} + R_r} - \frac{\beta_{tl}}{\beta_{tl} + R_r} = \frac{\delta\alpha}{\delta\alpha + R_r} - \frac{\delta\beta}{\delta\beta + R_r} = \frac{\alpha}{\alpha + \dfrac{R_r}{\delta}} - \frac{\beta}{\beta + \dfrac{R_r}{\delta}} \,. \tag{4.63}$$

This shows that lossless load matching indeed only shifts the known curve from Figure 3.5 along the R_r axis. Figure 4.20 illustrates this shift for a transmission system with an arbitrarily assumed transfer quality factor of $Q_k = 10$.

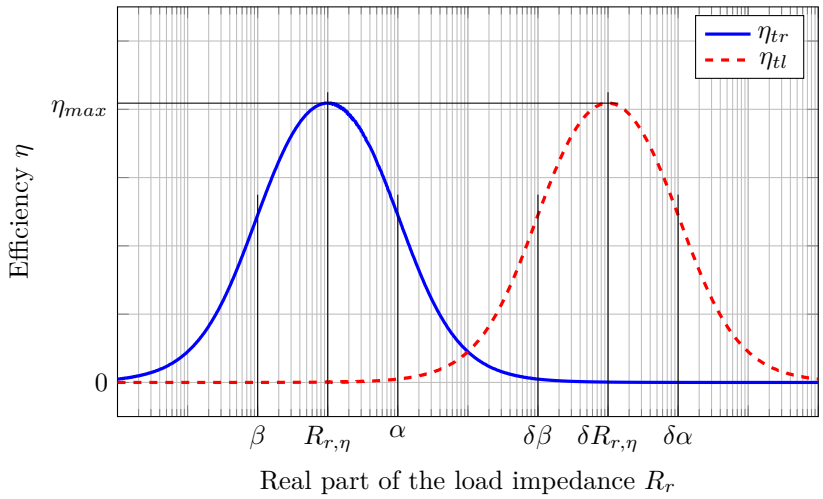

Figure 4.20.: *Shift of the efficiency curve caused by load matching, plotted versus a variable real part of the load impedance*

The two curves have exactly the same shape but are shifted relative to each other along the axis of the load resistance. In summary, neither source matching nor load matching affects the transfer quality factor or the transfer bandwidth. Only the load resistance range with high efficiency is shifted. This shift was already used in Section 4.2 to match the actual load resistance R_l to the optimal load resistance $R_{r,\eta}$.

For completeness, the same proof can also be carried out with a lossless and reciprocal admittance matrix [45, 46] instead of the impedance matrix (4.52). Only the factor δ from (4.60) differs. This additional proof underlines that reciprocal, lossless load-matching networks affect neither the transfer quality factor nor the transfer bandwidth.

4.5. Application Examples

The following examples illustrate the matching options described above. First, the inductive and capacitive example systems from Appendix A are matched. To allow comparison with the application examples of the preceding chapter (Section 3.4), a power of 10 W is transferred here as well. The sources are specified to supply a sinusoidal voltage with an amplitude of $|\boldsymbol{V}_d| = 10\,\mathrm{V}$ or a sinusoidal current with an amplitude of $|\boldsymbol{I}_d| = 1\,\mathrm{A}$. The frequency is 150 kHz in both cases. In the load matching example, the transmission system is matched to a resistive load of $R_l = 20\,\Omega$.

A final example revisits the multi-coil system from Section 3.4.2 and examines how the additional coils at the input and output affect the power transfer.

All voltages and currents given in the equivalent circuits are amplitudes of sinusoidal quantities.

4.5.1. Transmission System Matching

Section 4.1 showed that several characteristic parameters are required to adapt the transmission system directly. They can be obtained, for example, by measuring a comparable system according to Appendix B.1. In this example, the inductive system described in Appendix A.1 serves as the reference system. For clarity, the inductances are named as in Appendix A.1.

From the impedance matrix of the inductive example system (A.35), the required parameters $Q_{tt} = Q_{rr} = 10.42$, $k_X = 0.68$, and $k_R = 0$ follow. With these values, (4.6) also reproduces the transfer quality factor of $Q_k = 7.14$. These quantities are needed to solve (4.17) and (4.18). This yields $X_{rr} = 29.17\,\Omega$ and $X_{tt} = 12.37\,\Omega$, from which, at the specified frequency of 150 kHz, the inductances $L_t = 13.12\,\mu\text{H}$ and $L_r = 30.95\,\mu\text{H}$ result.

With X_{tt} and X_{rr}, (4.2) and (4.3) yield the loss resistances $R_{tt} = 1.19\,\Omega$ and $R_{rr} = 2.8\,\Omega$, and, in combination with (4.4) and (4.5), also the impedance $\boldsymbol{Z}_{tr} = j12.895\,\Omega$. At 150 kHz, this impedance corresponds to a mutual inductance of $M = 13.68\,\mu\text{H}$.

Finally, the optimal load and source reactances must be determined with these new values. (3.13) yields a load reactance of $-29.17\,\Omega$, which corresponds to a capacitance of 36.37 nF at 150 kHz. Furthermore, (3.54) yields a source reactance of $-18.18\,\Omega$, which can be realized by a capacitor of 58.36 nF.

These results lead to the circuit in Figure 4.21. Along with the inductances, the turns ratio of the new system has also been adapted to the specified conditions.

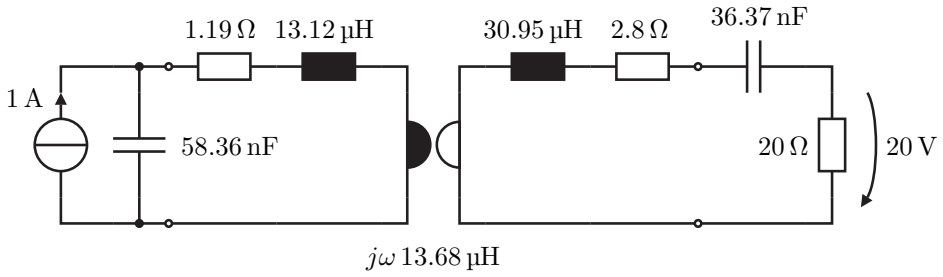

Figure 4.21.: *Application example of transmission system matching*

Compared to the application example in Figure 3.16 on page 46, the quality factors of the inductances (4.2) and (4.3), the coupling factors (4.4) and (4.5), and thus, according

to (4.6), also the transfer quality factor remain unchanged. Consequently, both systems have the same efficiency.

4.5.2. Load Matching

As described at the beginning of this chapter, adapting the transmission system is not always possible for design reasons. This also applies to the capacitive example system from Appendix A.2. With the electrode area, distance, and dielectric fixed, the transmission system cannot be adapted to the source or the load. If, as in the case shown here, the actual load resistance of 20 Ω differs from the optimal load already known from the application example in Figure 3.17 on page 47, load matching according to Section 4.2 is required to achieve maximum efficiency.

To transform the load resistance of the capacitive example system to the optimal load impedance using gyrator-based parallel load matching with a T network, the system matrix (A.77) (Figure 3.17) together with (3.13), (3.15), and (4.32) yields, for the two sign cases, the two equivalent synthesis vectors

$$\vec{\boldsymbol{Z}}_{T_1} = \begin{bmatrix} -j2.34 \\ j2.34 \\ -j2.35 \end{bmatrix} \text{k}\Omega \tag{4.64}$$

and

$$\vec{\boldsymbol{Z}}_{T_2} = \begin{bmatrix} j2.34 \\ -j2.34 \\ j2.33 \end{bmatrix} \text{k}\Omega\,. \tag{4.65}$$

These vectors define two matching networks that, at the frequency considered, transform the actual load resistance of 20 Ω into the optimal load impedance $Z_{r,\eta}$. From (4.64), for example, the components required for a practical implementation can be calculated as 453.6 pF, 2.48 mH, and 452.14 pF. Adding the corresponding T network (Appendix B.2.1) to the output of Figure 3.17 gives the circuit in Figure 4.22.

Although the inductive example system could be adapted directly (Section 4.5.1), the same load resistance is now also transformed to its optimal load impedance by gyrator-based parallel load matching with a T network. Using the same approach as before, the two equivalent synthesis vectors for the inductive example system are

$$\vec{\boldsymbol{Z}}_{T_1} = \begin{bmatrix} -j2.32 \\ j2.32 \\ j26.85 \end{bmatrix} \Omega \tag{4.66}$$

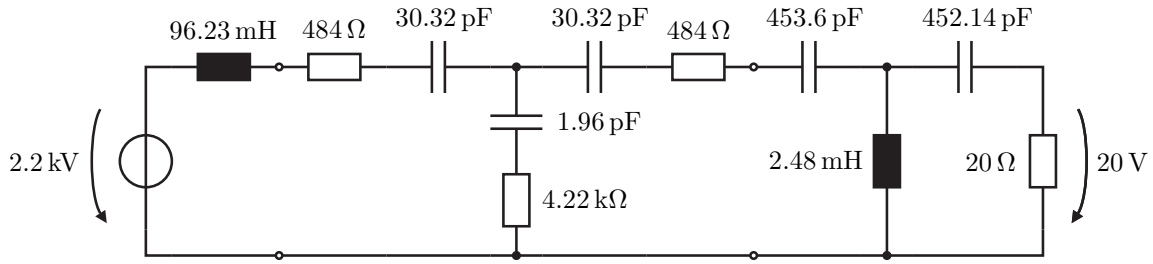

Figure 4.22.: *Application example of gyrator-based parallel load matching for the capacitive example system*

and

$$\vec{\boldsymbol{Z}}_{T_2} = \begin{bmatrix} j2.32 \\ -j2.32 \\ j31.38 \end{bmatrix} \Omega \,, \tag{4.67}$$

from which, taking (4.66) as an example, the components required for a practical implementation are 458.31 nF, 2.46 µH, and 28.49 µH. The resulting circuit is shown in Figure 4.23.

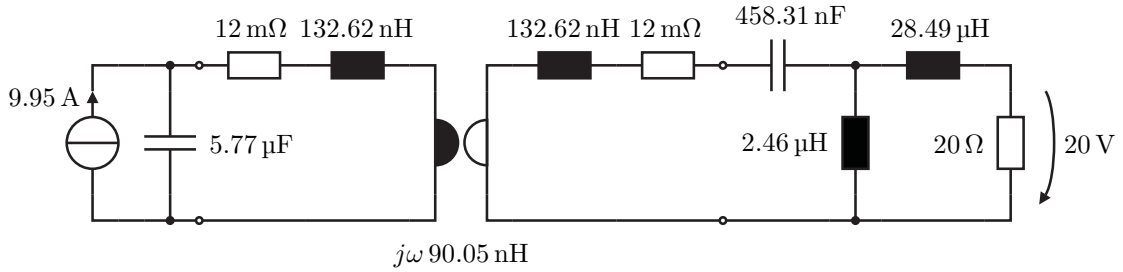

Figure 4.23.: *Application example of gyrator-based parallel load matching for the inductive example system*

The application examples in Figures 4.22 and 4.23 meet the specified requirements and, through the respective transmission system, deliver a power of 10 W into a resistance of 20 Ω. In both cases, the efficiency equals the maximum already known from Section 3.4: 99.2% for the capacitive and 75.44% for the inductive example system.

As with the application examples of the preceding chapter (Section 3.4), the voltage at the output terminals of the transmission system is determined for completeness. Since this voltage equals the input voltage of the respective matching network, its amplitude for the capacitive example system can easily be calculated from (4.64) as 2.34 kV. The voltage at the output terminals of the transmission system is therefore considerably higher than the voltage across the load resistance. The inductive example

system behaves differently: in the same way, (4.66) yields an amplitude of 2.32 V for the voltage at the output terminals of the transmission system. This voltage is lower than the voltage across the load resistance. As expected, both amplitudes agree with the values already determined in Section 3.4.

4.5.3. Source Matching

To transfer a power of 10 W with voltage feed, the capacitive example system in Figure 3.17 requires a voltage with an amplitude of 2.2 kV. This example shows how source matching allows the same transmission system to transfer the same power from an arbitrary voltage source, here with an amplitude of 10 V.

The introductory application example of capacitive coupling in Figure 3.17 on page 47 assumed that the transmission system is fed by a voltage source. For the transmission system to behave identically after matching to a different source, the output of the matching network must also behave like a voltage source. Since the given source is also a voltage source, matching according to the transformer-based voltage feed from Section 4.3.1 is required. With this matching network, the constant input voltage is transformed into a constant output voltage. According to Section 4.3.1, this matching is only possible with a Π network.

The transmission system is terminated with the optimal load impedance $Z_{r,\eta}$. With (3.41), (3.51), and (3.52), the amplitude of the input voltage V_t' and the source reactance X_t' required to transfer the specified power are known. With these quantities and the specification $|\boldsymbol{V}_d| = 10\,\mathrm{V}$, (4.37) yields the required turns ratio and (4.36) the possible synthesis vectors, depending on the sign of the turns ratio:

$$\vec{\boldsymbol{Z}}_\Pi = \begin{bmatrix} j1.89 \\ j413.07 \\ -j414.96 \end{bmatrix} \Omega \tag{4.68}$$

and

$$\vec{\boldsymbol{Z}}_\Pi = \begin{bmatrix} j1.87 \\ -j413.07 \\ j411.19 \end{bmatrix} \Omega \tag{4.69}$$

Changing the sign of the turns ratio changes the phase relationship between the input and output voltages of the matching network.

Choosing vector (4.69) gives the components 1.99 µH, 2.57 nF, and 436.29 µH. With Appendix B.2.2, Figure 3.17 is extended to the matched circuit in Figure 4.24.

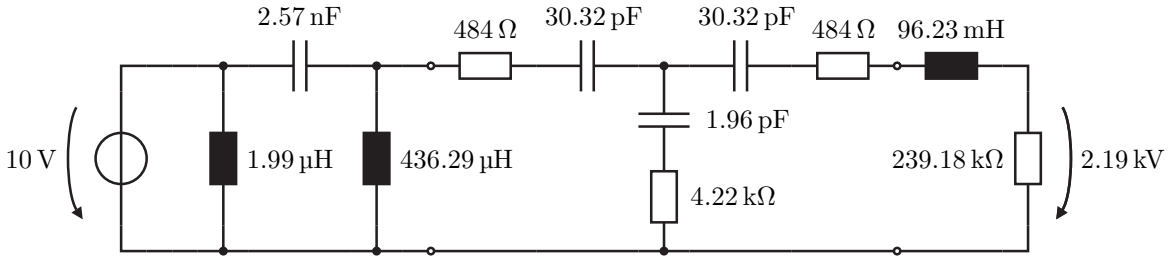

Figure 4.24.: *Application example of transformer-based voltage feed for the capacitive example system*

In contrast to the capacitive case, the introductory application example of inductive coupling in Figure 3.16 on page 46 assumed that the transmission system is fed by a current source. To obtain the same system behavior after source matching with a constant input voltage, matching according to the gyrator-based current feed from Section 4.3.4 is required. With this matching network, the constant input voltage is transformed into a constant output current. Here, too, a Π network is used.

This transmission system is likewise terminated with the optimal load impedance $Z_{r,\eta}$. From (3.40) and (3.41), together with (3.54) and (3.55), the source reactance of the current source X_t' and the amplitude of the required input current I_t' follow. These quantities are already known from Figure 3.16. (4.47) then gives the required gyration impedance, and (4.50) the synthesis vectors:

$$\vec{\boldsymbol{Z}}_{\Pi} = \begin{bmatrix} j1.01 \\ -j1.01 \\ -j0.23 \end{bmatrix} \Omega \tag{4.70}$$

and

$$\vec{\boldsymbol{Z}}_{\Pi} = \begin{bmatrix} -j1.01 \\ j1.01 \\ -j0.16 \end{bmatrix} \Omega\,. \tag{4.71}$$

For the practical implementation, synthesis vector (4.70) is chosen. At 150 kHz, it gives the components 1.07 µH, 1.06 µF, and 4.72 µF shown in Figure 4.25.

The application examples in Figures 4.24 and 4.25 both meet the specified requirements and, despite being driven by an arbitrary source, deliver an active power of 10 W to the real part of the respective optimal load impedance. In both cases, the efficiency reaches the already known maximum of 99.2% for the capacitive and 75.44% for the inductive example system.

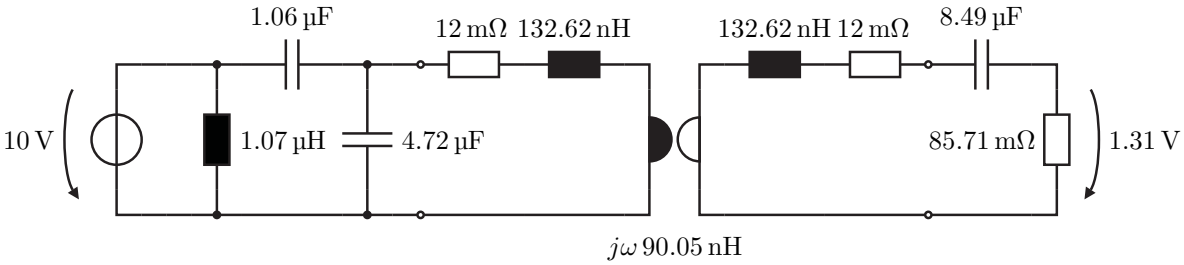

Figure 4.25.: *Application example of gyrator-based current feed for the inductive example system*

Here, too, the voltage at the input terminals of the transmission system is determined for completeness. Since both transmission systems are terminated with the optimal load impedance $Z_{r,\eta}$, this voltage can easily be determined from (3.40) and (3.41) and the respective synthesis vectors (4.68) and (4.70). For the capacitive example system, a voltage amplitude of 2.35 kV results at the input terminals. This voltage is considerably higher than the source voltage. For the inductive example system, by comparison, a voltage amplitude of 2.67 V results. This voltage is lower than the source voltage. As expected, the amplitudes determined in this way agree with those already determined in Section 3.4.

4.5.4. Multi-Coil System

In principle, the following analysis applies to systems with any number of coupled inductances, for example the three-coil system in [28]. The application example presented here is based on the widely used transmission system with four coupled inductances, which is already known from Section 3.4.2.

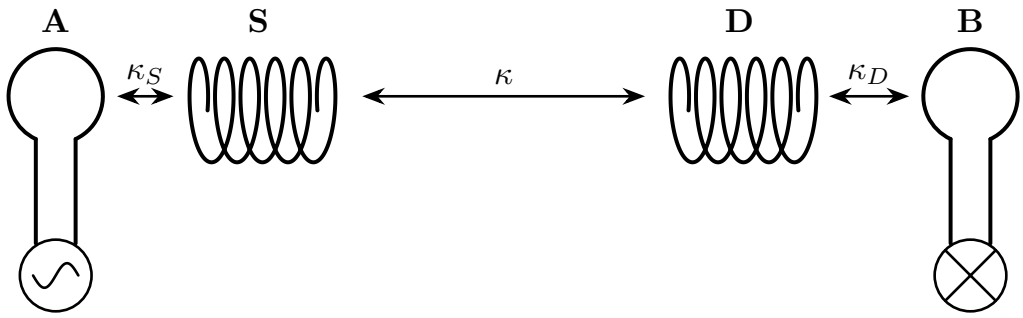

Figure 4.26.: *Four-coil transmission system from Figure 3.18, own illustration, adapted from [31]*

Figure 4.26 shows an arrangement of four coupled coils that is used in many publications on inductive power transfer [28, 52, 53, 54]. These publications usually assume that only three of the coupling factors between the four inductances are significant [52]. In Figure 4.26, for example, there is approximately no coupling between the inductances L_A and L_D, L_A and L_B, or L_S and L_B. With this assumption, for the lossless case and sinusoidal quantities, analogous to the transformer equations (A.25) and using the nomenclature of [31], the system of equations

$$\begin{bmatrix} \boldsymbol{V}_A \\ \boldsymbol{V}_S \\ \boldsymbol{V}_D \\ \boldsymbol{V}_B \end{bmatrix} = j\omega \begin{bmatrix} L_A & \kappa_S\sqrt{L_A L_S} & 0 & 0 \\ \kappa_S\sqrt{L_A L_S} & L_S & \kappa\sqrt{L_S L_D} & 0 \\ 0 & \kappa\sqrt{L_S L_D} & L_D & \kappa_D\sqrt{L_D L_B} \\ 0 & 0 & \kappa_D\sqrt{L_D L_B} & L_B \end{bmatrix} \begin{bmatrix} \boldsymbol{I}_A \\ \boldsymbol{I}_S \\ \boldsymbol{I}_D \\ \boldsymbol{I}_B \end{bmatrix} \tag{4.72}$$

can be written. If, for simplicity, mutual inductances are defined by rearranging (A.22) as

$$M_S = \kappa_S\sqrt{L_A L_S}\,, \tag{4.73}$$

$$M = \kappa\sqrt{L_S L_D} \tag{4.74}$$

and

$$M_D = \kappa_D\sqrt{L_D L_B} \tag{4.75}$$

the equivalent circuit in Figure 4.27 can be derived from (4.72).

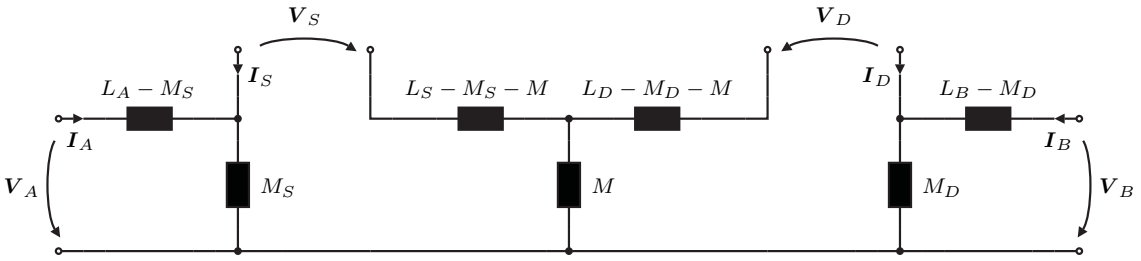

Figure 4.27.: *Inductive model of the simplified transformer equations (4.72)*

The cited publications and Figure 3.19 show that each of the inner inductances is connected only to a resonant capacitor. Consequently, the terminal pairs at $\boldsymbol{V}_S$ and $\boldsymbol{V}_D$ can each be terminated with a resonant capacitor, C_S and C_D. In addition, the input and output loops each contain a resonant capacitor, C_A and C_B.

The chain matrix of the complex gyrator is known from (3.81). If this matrix is realized as a T network using the vector (B.21), Figure 4.28(b) results. Consequently, the

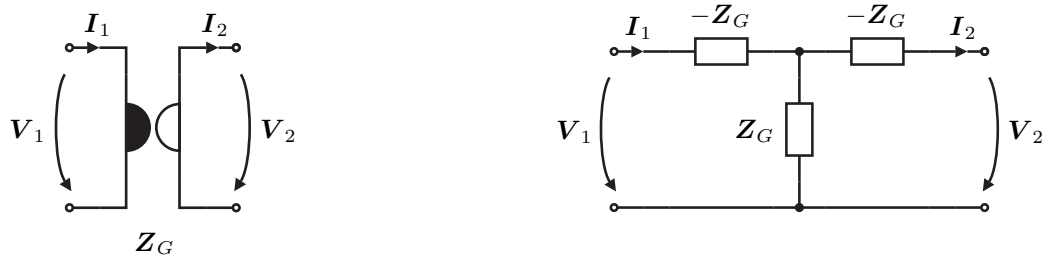

(a) Complex gyrator from Figure 3.13(b)

(b) T network of the complex gyrator

Figure 4.28.: *Synthesis of the complex gyrator as a T network*

complex gyrator can be represented by a T network with a shunt impedance equal to the gyration impedance and two identical series impedances equal to the negative of the gyration impedance. This relationship also makes it possible, for example, to convert the general transmission system directly into the new equivalent circuit in Figure 3.14(a) after splitting each of the two series impedances in Figure 3.2 into a series connection of two partial impedances. The same is possible in Figure 4.27. If the mutual inductances M_S, M, and M_D shown there are regarded as gyration impedances and, in addition, the required negative gyration impedances are extracted from the series inductances, the equivalent circuit in Figure 4.29 follows after taking the resonant capacitors into account.

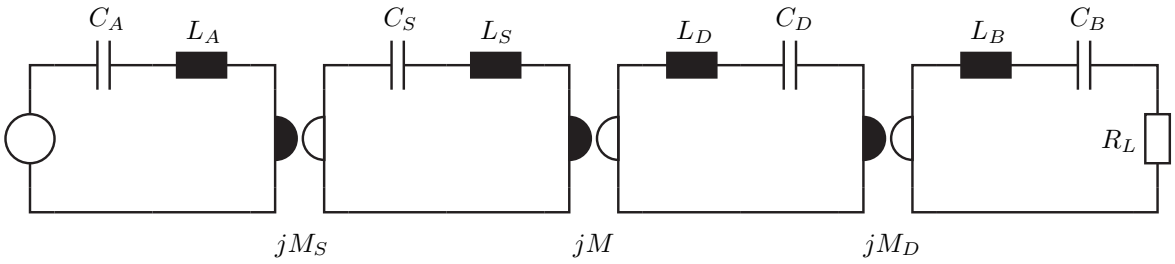

Figure 4.29.: *Transmission system with four coupled inductances (Figure 3.19) represented by three complex gyrators*

The capacitances C_A and C_B are generally chosen such that they form a series resonant circuit with the inductances L_A and L_B, respectively [52]. Since the total impedance of a lossless series resonant circuit excited at its resonant frequency is zero, the series connections of C_A and L_A and of L_B and C_B can be regarded as direct connections. Furthermore, comparing the inner complex gyrator with the equivalent circuit in Figure 3.14(a) shows that this gyrator, together with the inductances L_S and L_D, corresponds to the equivalent circuit of the lossless inductive coupling between the two inner inductances in Figure 4.27.

As a result of these considerations, the capacitance C_S together with the left gyrator can formally be regarded as a source matching network according to Figure 4.16, and the capacitance C_D together with the right gyrator as a load matching network according to Figure 4.9. This makes it clear that, under the stated simplifications, a system with four coupled inductances cannot achieve a higher efficiency than one with two. It merely represents another way of implementing source and load matching.

To achieve the same transfer behavior as in Figure 4.29 with only two inductances, the inductance L_S must be excited by a gyrator-based voltage feed (Section 4.3.2), and power must be drawn from L_D by gyrator-based series load matching (Section 4.2.2).

The preceding analysis of the lossless system has shown that the same transfer characteristics as those of a transmission system with four coupled inductances can also be obtained with a transmission system consisting of only two coupled inductances. The lossy case would still have to be examined separately, which is beyond the scope of this thesis.

Figure 4.29 also highlights a particular advantage of the complex gyrator. In the lossless case, it is immediately apparent that, with series resonance of L_S and C_S as well as L_B and C_B, the system will deliver a load-independent output voltage when current-fed. According to (3.75), the constant input current results in a constant voltage at the output of the first complex gyrator. If the inductance L_S is compensated, this voltage is at the same time the constant input voltage of the middle gyrator, which, according to (3.74), delivers a constant output current. As the input current of the last gyrator, the constant current therefore produces a constant output voltage. Alternative equivalent circuits show this relationship less clearly.

5. Summary and Outlook

In addition to the chosen description and possible equivalent circuits, Chapter 3 established the requirements that the external circuitry of a transmission system must meet to transfer maximum power at maximum efficiency. High efficiency requires a suitable load impedance at the output terminals of the transmission system. This impedance was determined as $\boldsymbol{Z}_{r,\eta}$ according to (3.16). To transfer high active power, in turn, a voltage source with a source reactance according to (3.51) or a current source with a source reactance according to (3.54) is required.

Since these requirements cannot always be met directly, Chapter 4 presented matching methods: both the direct adaptation of the transmission system to a given source and load resistance and indirect matching with additional networks. With these methods, any near-field transmission system can be driven from an arbitrary source while delivering the desired power to an arbitrary load resistance at maximum efficiency.

In Section 3.3.2, a new equivalent circuit of the transmission system with a complex gyrator was presented. Figure 3.15 showed that a transmission system terminated with the optimal load reactance $X_{r,\eta}$ (3.13) and driven with a source reactance according to (3.51) behaves approximately like a complex gyrator. Consequently, if power transfer with an approximately constant and load-independent output voltage is required, the transmission system must be fed by a constant current. This is where the matching networks from Sections 4.2 and 4.3 become important. If the transmission system requires a constant current but only a voltage source is available, this can be resolved by source matching according to the gyrator-based current feed from Section 4.3.4. This matching network transforms the constant voltage source into a constant current, which then drives the transmission system. If load matching is also needed and the load voltage is to remain approximately constant and load-independent, this source matching must be combined with transformer-based series load matching according to Section 4.2.1. This ensures that the now comparatively constant output voltage of the transmission system also results in an approximately constant and load-independent voltage across the load resistance.

Along the same lines, other circuit configurations with similar transfer behavior are possible. If, for example, transformer-based voltage feed is chosen for matching at the input terminals and gyrator-based series load matching at the output terminals, a constant input voltage likewise results in a constant and load-independent voltage

across the load resistance. In total, twelve possible load matching networks and twelve possible source matching networks were presented. Combined, they offer 144 different ways of matching a transmission system. Comparing these many variants is left to future work.

The synthesis vectors presented in Appendix B.2 for implementing the matching networks in practice represent only one possible solution; many other networks with identical terminal behavior are conceivable. If, for example, a matching network has to convert a low input voltage into a high output voltage, the synthesis vectors shown require high-Q resonant circuits for the voltage step-up. Since such a high quality factor usually permits only small component tolerances, more practical matching networks with coupled inductances can be found for the voltage step-up, in which tolerances of the resonant circuits have less effect. This aspect, too, deserves further investigation.

Practical networks and transmission systems are always subject to tolerances. If a constant output quantity is required, closed-loop control is often unavoidable, which in turn requires feedback from the power receiver to the power transmitter. This feedback can be implemented in many different ways, for example via an additional transmission channel in the near or far field, or by modulating the transmission system itself. The following assumes that some form of feedback is available.

To maintain maximum efficiency at the same time, a control scheme based on the two-stage method shown in Figure 5.1 could be designed. For illustration, it is assumed that the loss resistance R_{tr} of the shunt impedance $\boldsymbol{Z}_{tr}$ in Figure 3.2 can be neglected.

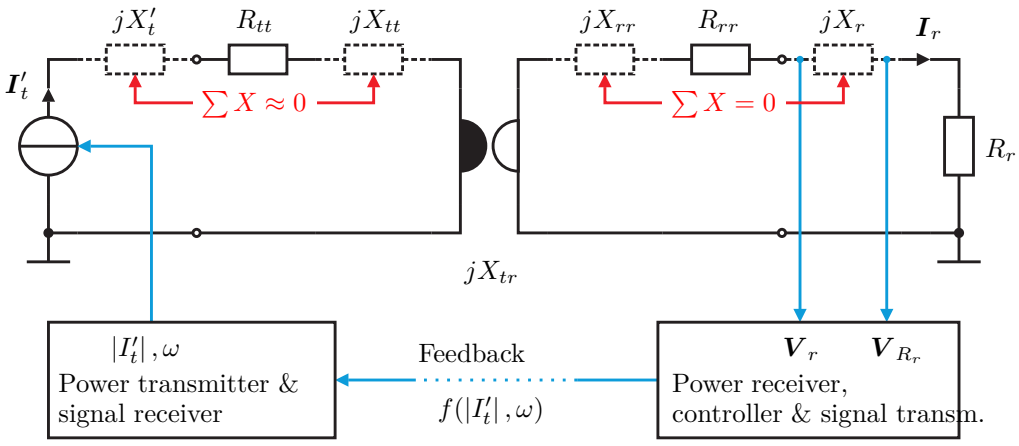

Figure 5.1.: *Possible control model*

In Chapter 3, (3.13) determined the reactance of the load impedance X_r required to maximize the efficiency. Under the condition $R_{tr} = 0$, it equals $-X_{rr}$. To meet this

condition despite component tolerances, closed-loop control appears useful. Assuming that the transmission system is fed by a constant current, the voltage at the output of the complex gyrator is constant. If, in addition, the reactance X_r varies inversely with frequency, unlike the reactance X_{rr}, there is a frequency at which the magnitudes of the two reactances are equal. At this point, the two reactances are in resonance, the condition $X_r = -X_{rr}$ is met, and the voltage across each individual reactance reaches a maximum. A controller that tracks this maximum, using the frequency as the manipulated variable, ensures that the imaginary part required for maximum efficiency is actually present.

Under these conditions, the load resistance receives the complex gyrator's output voltage, reduced only by the loss resistance. Because of the current feed, the voltage across the load resistance R_r therefore depends only slightly on the value of this resistance. If this voltage must match a specified value exactly even with a variable load, an additional outer control loop can be used. This control loop uses the amplitude of the injected current as the manipulated variable. Because of the transfer characteristics of the complex gyrator, only a slight change in this amplitude is required. It compensates load-dependent voltage drops across the loss resistance R_{rr}.

The series reactance X_t' in Figure 5.1 serves to reduce the voltage at the current source and ideally equals $-X_{tt}$. Because of tolerances, this can only be met approximately. Since the system is current-fed, however, X_t' does not affect the power transfer.

The control of the transmission system and the feedback path are left to future work. This should also examine phase-angle control and pulse-width modulation as manipulated variables in addition to frequency and amplitude.

A. Example Systems

To illustrate the forms of description and matching shown in Chapters 3 and 4, the impedance matrices (3.3) of an inductive and a capacitive transmission system are derived theoretically. For a fair comparison, both systems use the same area for power transfer and the same distance between transmitter and receiver. A circular area of $A_{ges} = 2000\,\mathrm{mm}^2$ was specified, corresponding to a diameter of $d_{ges} = 50.46\,\mathrm{mm}$. Figure A.1 shows a schematic representation of the two chosen example systems.

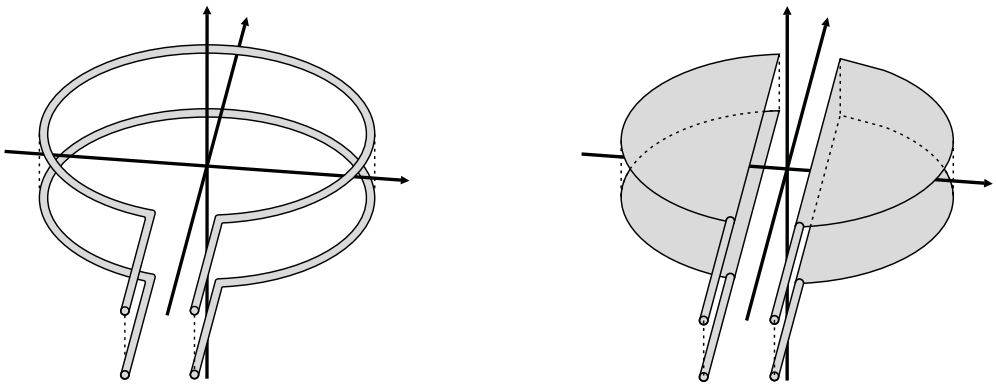

(a) Inductive coupling (b) Capacitive coupling

Figure A.1.: *Example systems for inductive and capacitive near-field coupling*

In both the inductive system in Figure A.1(a) and the capacitive system in Figure A.1(b), the transmitter and the receiver are of identical design.

Figure A.1 already reveals fundamental differences between the two transfer methods. Inductive power transfer is an electromagnetic interaction. As with a conventional tightly coupled transformer, two electromagnetic conversions are required for power transfer. On the transmitter side, the electric current is converted into a magnetic field by a conductor loop. This magnetic field induces a voltage in a second, distant conductor loop, which then serves as an electrical source on the receiver side. Since both transmitter and receiver are stationary, alternating quantities are required. This makes the analysis somewhat more complex but, in principle, allows the conversion to be modified according to Section 4.1 to shape the transfer characteristics. One example

is adapting the turns ratio between the coupled windings. Because the magnetic field is solenoidal (divergence-free), each winding can use the entire available area.

Capacitive power transfer is different. This coupling is based on purely electric-field relationships, which simplifies its description. Because the impedance of a capacitor tends toward infinity at DC, alternating quantities are required here as well. Unlike inductive power transfer, however, it offers no means of adjustment once the electrode size, distance, and dielectric are fixed. This may make an additional transformation of the input or output quantities according to Sections 4.2 and 4.3 necessary. In addition, the capacitive variant needs two electrodes on each side, for the forward and return paths, within the available area. Since a parasitic capacitance also acts between these two electrodes, their placement is critical. Unlike the inductive system, the capacitive system shown is not rotationally symmetric. If the application requires this, the electrodes could be changed to a coaxial arrangement.

Neither the inductive nor the capacitive example system in Figure A.1 is optimized. For inductive coupling in particular, more turns can be expected to increase the coil quality factor and thus, according to (4.6), improve the transfer characteristics. Since both systems require alternating quantities for power transfer, this thesis assumes a fixed frequency of 150 kHz for both systems.

A.1. Inductive System

This section analyzes the inductive coupling between two conductor loops and derives an impedance matrix for comparison with alternative methods. Figure A.2 shows the example system chosen for inductive coupling. Two conductor loops are bonded to a

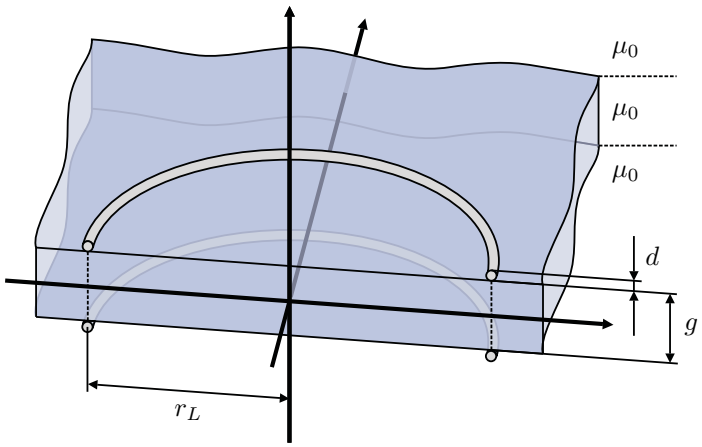

Figure A.2.: *Example system for inductive coupling*

carrier material with a relative permeability of $\mu_r = 1$. Since this material does not affect the magnetic field, each of the two conductor loops can be regarded as an air-core coil.

A.1.1. Magnetic Vector Field of a Concentric Conductor Loop

An electric current flowing in a conductor loop generates a magnetic field. Since the direction and magnitude of this field vary with position, it must be described by a vector field. Under a quasi-static assumption, the field can be calculated using the Biot-Savart law [57]. The Biot-Savart law gives the infinitesimal magnetic flux density at a point $P_{\mathrm{d}\vec{B}}$ generated by an infinitesimal current-carrying conductor element $\mathrm{d}\vec{l}$:

$$\mathrm{d}\vec{B} = \frac{\mu_0 I}{4\pi} \frac{\mathrm{d}\vec{l} \times \vec{R}}{|\vec{R}|^3} \,, \tag{A.1}$$

where the vector $\vec{R}$ connects the infinitesimal conductor element $\mathrm{d}\vec{l}$ at the point $P_{\mathrm{d}\vec{l}}$ and the point of interest $P_{\mathrm{d}\vec{B}}$. The vector $\mathrm{d}\vec{l}$ points in the direction of current flow.

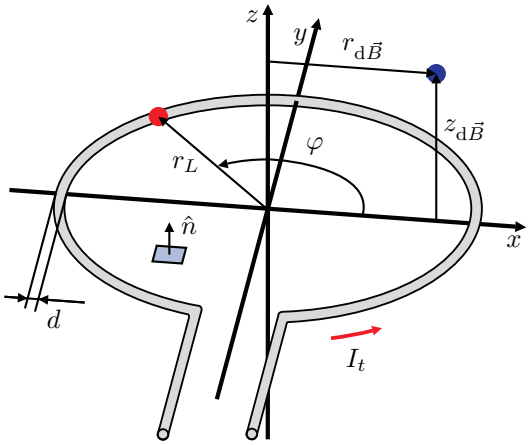

Figure A.3.: *Concentric conductor loop. The area vector $\hat{n}$ is orthogonal to the enclosed area at every point.*

For the concentric conductor loops considered here (Figure A.2), cylindrical coordinates are the natural choice. The z axis of this coordinate system is chosen to coincide with an axis through the centers of the conductor loops, orthogonal to the area enclosed by each loop. As shown in Figure A.3, the origin is placed at the center of one conductor loop. The area enclosed by this loop thus lies in the r-φ plane. This plane is shown in Figure A.4.

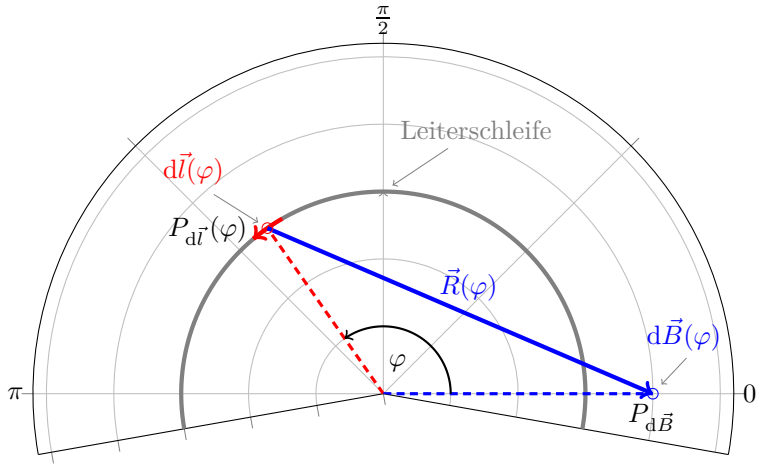

Figure A.4.: *Calculation of the magnetic flux density using the Biot-Savart law in the r-φ plane*

The position of the infinitesimal conductor element $\mathrm{d}\vec{l}$ is described by the point $P_{\mathrm{d}\vec{l}}$ in three-dimensional space. The same applies to the position of the point of interest $P_{\mathrm{d}\vec{B}}$. In vector notation, in cylindrical coordinates with a constant loop radius r_L,

$$P_{\mathrm{d}\vec{l}}(\varphi) = \begin{bmatrix} r_L \\ \varphi \\ 0 \end{bmatrix}_Z \tag{A.2}$$

and

$$P_{\mathrm{d}\vec{B}} = \begin{bmatrix} r_{\mathrm{d}\vec{B}} \\ 0 \\ z_{\mathrm{d}\vec{B}} \end{bmatrix}_Z . \tag{A.3}$$

The subscript Z on the vectors indicates that cylindrical coordinates were chosen. For the conductor loop in the r-φ plane, the z component is always zero. Because of the rotational symmetry of the conductor loop, the point of interest can always be placed at $\varphi = 0$ by rotating the loop.

The connecting vector $\vec{R}(\varphi)$, shown dashed in Figure A.4, is the difference between the position vectors (A.2) and (A.3). In general, the difference between two points in cylindrical coordinates is

$$\vec{R}_P = \vec{P} - \vec{P}' = \begin{bmatrix} r - r' \cos(\varphi - \varphi') \\ r' \sin(\varphi - \varphi') \\ z - z' \end{bmatrix} . \tag{A.4}$$

The difference $\vec{R}_P$ is then given in Cartesian coordinates. For the case considered here, (A.4) yields the difference

$$\vec{R}(\varphi) = \vec{P}_{\mathrm{d}\vec{B}} - \vec{P}_{\mathrm{d}\vec{l}}(\varphi) = \begin{bmatrix} r_{\mathrm{d}\vec{B}} - r_L \cos(\varphi) \\ -r_L \sin(\varphi) \\ z_{\mathrm{d}\vec{B}} \end{bmatrix} \tag{A.5}$$

The magnitude of the connecting vector required to solve the Biot-Savart equation can be calculated with the dot product

$$|\vec{R}(\varphi)| = \sqrt{\vec{R}(\varphi) \circ \vec{R}(\varphi)} \tag{A.6}$$

After transformation into a Cartesian coordinate system, the point $P_{\mathrm{d}l}$ is given by

$$P_{\mathrm{d}\vec{l}}(\varphi) = \begin{bmatrix} r_L \\ \varphi \\ 0 \end{bmatrix}_Z \xrightarrow{Z \to C} \begin{bmatrix} r_L \cos(\varphi) \\ r_L \sin(\varphi) \\ 0 \end{bmatrix} . \tag{A.7}$$

After a simple substitution [58], the vector of the infinitesimal conductor element $\mathrm{d}\vec{l}$ can be determined from (A.7):

$$\mathrm{d}\vec{l}(\varphi) = \begin{bmatrix} \frac{\mathrm{d}x}{\mathrm{d}\varphi}\mathrm{d}\varphi \\ \frac{\mathrm{d}y}{\mathrm{d}\varphi}\mathrm{d}\varphi \\ \frac{\mathrm{d}z}{\mathrm{d}\varphi}\mathrm{d}\varphi \end{bmatrix} = \begin{bmatrix} \frac{\mathrm{d}}{\mathrm{d}\varphi}\left(r_L \cos(\varphi)\right)\mathrm{d}\varphi \\ \frac{\mathrm{d}}{\mathrm{d}\varphi}\left(r_L \sin(\varphi)\right)\mathrm{d}\varphi \\ \frac{\mathrm{d}}{\mathrm{d}\varphi}0\,\mathrm{d}\varphi \end{bmatrix} = \begin{bmatrix} -r_L \sin(\varphi) \\ r_L \cos(\varphi) \\ 0 \end{bmatrix} . \tag{A.8}$$

With (A.5), (A.6), and (A.8), all components needed to solve the Biot-Savart equation (A.1) have been found. For an arbitrary point $P_{\mathrm{d}\vec{B}}$, the magnetic flux density vector is obtained by integrating all infinitesimal contributions

$$\vec{B} = \frac{\mu_0 I}{4\pi} \int_0^{2\pi} \frac{\mathrm{d}\vec{l}(\varphi) \times \vec{R}(\varphi)}{|\vec{R}(\varphi)|^3}\,\mathrm{d}\varphi \tag{A.9}$$

along the conductor loop. The corresponding vector field is shown normalized in Figure A.5. Because of the symmetry of the conductor loop, it is sufficient to show the x-z plane. The field is rotationally symmetric about the z axis.

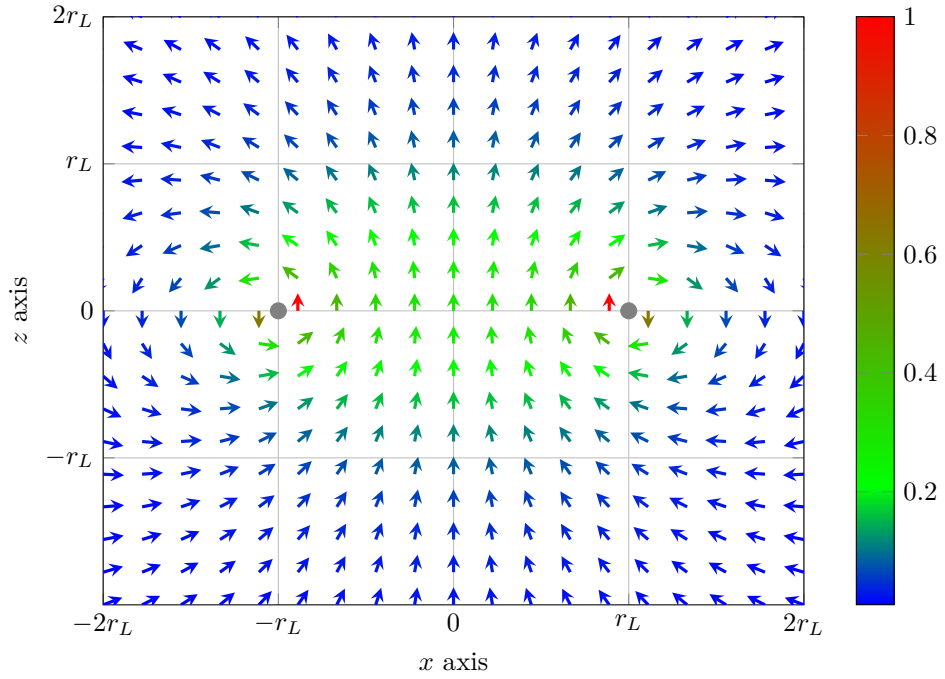

Figure A.5.: *Normalized vector field of a current-carrying conductor loop according to Biot-Savart*

The color coding in Figure A.5 clearly shows that the field inside the conductor loop is generally stronger than outside. Intuitively, this follows from Gauss's law for magnetism (one of Maxwell's equations): there are no magnetic monopoles, and the magnetic field is solenoidal. Because of

$$\oint_S \vec{B} \circ \hat{n} \, \mathrm{d}a = 0 \tag{A.10}$$

in microscopic form, all field lines are closed. The number of field lines passing through the loop must therefore equal the number returning outside it. Since the area inside the loop is bounded, whereas the area outside extends to infinity, the flux density inside is many times higher; the field is strongly concentrated inside the loop. The color coding also shows that the field is strongest near the current-carrying conductor. This is consistent with the field of an infinitely long straight conductor, whose flux density decreases inversely with distance. Accordingly, the field of a closed loop also decreases toward the center of the loop.

The magnetic flux Φ through the conductor loop can be calculated by integrating the

field vectors over the entire enclosed area:

$$\Phi = \int_0^{2\pi} \int_0^{r_L - \frac{d}{2}} \vec{B} \circ \hat{n}\, r_{\mathrm{d}\vec{B}}\, \mathrm{d}r_{\mathrm{d}\vec{B}} \mathrm{d}\varphi \Big|_{z_{\mathrm{d}\vec{B}}=0} , \tag{A.11}$$

where the vector $\hat{n}$ is the unit vector in the z direction, $\hat{n} = \vec{e}_z = [0, 0, 1]^{\mathrm{T}}$. Because of its low resistance, the interior of the loop wire is assumed to be approximately field-free. The upper integration limit in (A.11) is therefore reduced by half the wire diameter d. Because of the symmetry of the conductor loop, the field vectors penetrating the area enclosed by the loop have no x or y component; they are orthogonal to the area.

If the current amplitude changes, the magnetic flux density $\vec{B}$, and thus the magnetic flux Φ, changes proportionally. According to Faraday's law of induction (another of Maxwell's equations), this change induces a proportional voltage in the conductor loop. In integral form,

$$v(t) = \oint_C \vec{E} \circ \mathrm{d}\vec{l} = -\frac{\mathrm{d}}{\mathrm{d}t} \int_S \vec{B} \circ \hat{n}\, \mathrm{d}a\,. \tag{A.12}$$

The induced voltage around the closed loop is the line integral of the electric field $\vec{E}$ and equals the negative time derivative of the magnetic flux through the loop, i.e., of the integral of the normal component of $\vec{B}$ over the enclosed area. The unit vector $\hat{n}$ is perpendicular to each infinitesimal area element $\mathrm{d}a$ penetrated by magnetic flux. Because of (A.12), a change in magnetic flux results in

$$v(t) = -\frac{\mathrm{d}\Phi(t)}{\mathrm{d}t} , \tag{A.13}$$

according to which the voltage induced in the conductor loop can be determined directly from (A.11) and the corresponding time dependence. Since the voltage is induced by the current in the same loop, this is called self-induction; induction by an externally generated magnetic flux is called mutual induction.

The relationship between the current and the generated field, or the self-induced voltage, can be defined by a proportionality factor L, which is called the inductance of the conductor loop. It can likewise be determined directly from (A.11) as

$$L = \frac{N\Phi}{I}\Big|_{N=1} = \frac{1}{I} \int_0^{2\pi} \int_0^{r_L - \frac{d}{2}} \vec{B} \circ \hat{n}\, r_{\mathrm{d}\vec{B}}\, \mathrm{d}r_{\mathrm{d}\vec{B}} \mathrm{d}\varphi \Big|_{z_{\mathrm{d}\vec{B}}=0} \tag{A.14}$$

where the factor N is the number of turns. For the single conductor loop considered here, $N = 1$.

From (A.11), (A.13), and (A.14), the well-known relationship for the voltage across the conductor loop in the passive sign convention follows:

$$v(t) = L\frac{\mathrm{d}i(t)}{\mathrm{d}t} \,. \tag{A.15}$$

[59] gives an approximation for the inductance of a concentric conductor loop. For wire cross sections that are very small compared to the enclosed area, it is

$$L \approx N^2 \mu_0 r_L \ln\left(\frac{2r_L}{d}\right) \tag{A.16}$$

A maximum ratio of wire diameter to loop radius of $d/r_L < 0.002$ is specified for this approximation.

A.1.2. Magnetic Coupling

As in Chapter 3, the subscripts t and r denote transmitter and receiver. The subscript rt indicates that the corresponding quantity occurs in the receiver loop but is generated by the transmitter loop. Thus, for example, the magnetic flux Φ in (A.11) becomes the magnetic flux Φ_{tt}, because it occurs in the transmitter loop and is generated by the current in the transmitter loop.

The vector field determined in Section A.1.1 induces a voltage according to (A.12) or (A.13) not only in the field-generating conductor loop but also in any other conductor loop. This induced voltage depends on the penetrating field vectors and thus on the position of the respective conductor loop.

If, as shown in Figure A.6, a second conductor loop of identical design is merely displaced along the z axis, the magnetic flux penetrating this second loop orthogonally can be determined according to (A.11) by

$$\Phi_{rt} = \int_0^{2\pi} \int_0^{r_L - \frac{d}{2}} \vec{B} \circ \hat{n}_r \; r_{\mathrm{d}\vec{B}} \; \mathrm{d}r_{\mathrm{d}\vec{B}} \mathrm{d}\varphi \Big|_{z_{\mathrm{d}\vec{B}} = g} \tag{A.17}$$

where g is the distance between the conductor loops. Because of the purely axial displacement in the z direction, the vector $\hat{n}_r$ is again $\hat{n}_r = \hat{n}_t = [0, 0, 1]^{\mathrm{T}}$.

The flux Φ_{rt} penetrating the second conductor loop must be smaller than the flux Φ_{tt} in the field-generating loop. This, too, follows from the solenoidal nature (A.10) of the field: the field lines close outside the conductor loop, so the normal field component

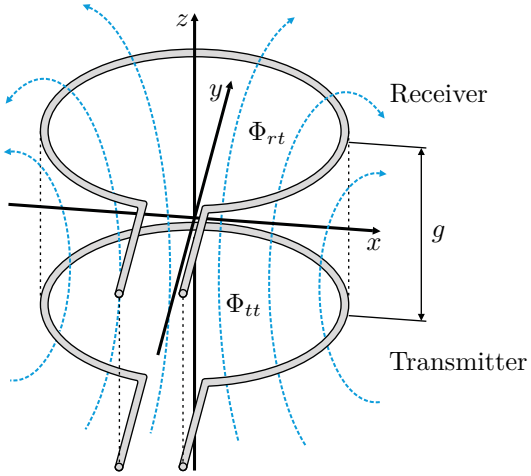

Figure A.6.: *Two magnetically coupled conductor loops*

inside the second loop decreases with increasing distance g. A magnetic coupling factor can be defined as

$$k_{X_{rt}} = \frac{\Phi_{rt}}{\Phi_{tt}} \tag{A.18}$$

Its magnitude is therefore always smaller than one. A negative value means that the field passes through the loop in the opposite direction, which merely changes the signs.

Figure A.7 shows the calculated coupling factor $k_{X_{rt}}$ as a function of the distance g. Clearly, the magnetic coupling between two conductor loops according to (A.18)

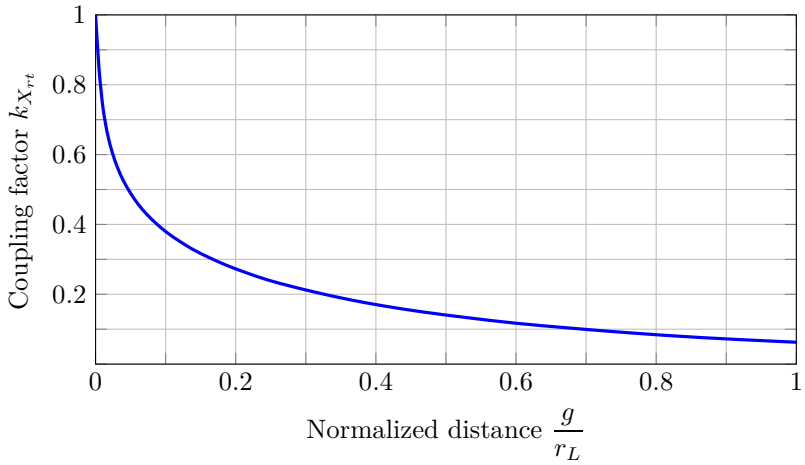

Figure A.7.: *Coupling factor $k_{X_{rt}}$ between two identical conductor loops versus axial distance g*

decreases very rapidly with increasing axial distance in the z direction.

The voltage induced in the second conductor loop can likewise be determined according to (A.13). Here, too, an inductance can be defined that describes the proportional relationship between the current flowing in the transmitter loop and the voltage induced in the receiver loop:

$$M_{rt} = \frac{N_r \Phi_{rt}}{I_t}\bigg|_{N=1} = \int_0^{2\pi} \int_0^{r_L - \frac{d}{2}} \vec{B} \circ \hat{n}\, r_{\mathrm{d}\vec{B}}\, \mathrm{d}r_{\mathrm{d}\vec{B}} \mathrm{d}\varphi \bigg|_{z_{\mathrm{d}\vec{B}}=g} \tag{A.19}$$

This is called the mutual inductance M_{rt}. According to (A.19), and analogous to (A.15), a voltage induced in the conductor loop can be determined by

$$v_{rt}(t) = M_{rt} \frac{\mathrm{d}i_t(t)}{\mathrm{d}t} \tag{A.20}$$

[59] also gives an approximation for the mutual inductance. Unlike (A.16), however, it is only a rough approximation for large distances between the conductor loops and should only be used for distances of $g \gg 0.2 r_L$. Even then, deviations of up to 30% are possible.

If a load is connected to the receiver loop, a current flows in it as well. According to (A.11), this current also generates a magnetic flux Φ_{rr}, which, according to Lenz's law, opposes the generating flux Φ_{rt} and thus weakens the total flux in the second conductor loop. In addition, similar to Figure A.6, part of the flux Φ_{rr} also penetrates the transmitter loop, weakening the field there as well. Analogous to (A.14), (A.17), (A.18), (A.19), and (A.20), L_r, $k_{X_{tr}}$, M_{tr}, and v_{tr} can be described, and an energy consideration [57] shows that the mutual inductances M_{rt} and M_{tr} are equal.

The two coupling factors $k_{X_{rt}}$ and $k_{X_{tr}}$ are generally not identical. When energy is transferred, current flows in both conductor loops simultaneously. It is therefore helpful to define an overall coupling factor k_X:

$$k_X = \sqrt{k_{X_{rt}} k_{X_{tr}}} \tag{A.21}$$

In this simple arrangement with identical conductor loops, symmetry requires the two coupling factors $k_{X_{rt}}$ and $k_{X_{tr}}$ to be equal. With the mutual inductance M from (A.19), the self-inductances L_t and L_r from (A.14), and $M_{tr} = M_{rt} = M$, (A.21) yields

$$k_X = \frac{M}{\sqrt{L_t L_r}}\,. \tag{A.22}$$

In summary, the magnetic coupling can be described as follows. An injected direct current I_t generates a static magnetic flux according to (A.11). According to (A.12), this

static flux cannot induce any voltages in stationary conductor loops. A time-varying current $i_t(t)$, in the quasi-static approximation, generates a proportional magnetic flux, likewise given by (A.11). This time-varying flux does cause induction.

The varying flux induces the voltage $v_{tt}(t)$ in the transmitter loop according to (A.15). At the same time, the magnetic flux induces the voltage $v_{rt}(t)$ in the receiver loop according to (A.20). For an injected current, these two voltages are independent of any load connected to the receiver loop. If the receiver loop is loaded, a current $i_r(t)$ flows. In addition to the load, this current depends on the inductance of the receiver loop and on the induced voltage $v_{rt}(t)$. According to (A.11), the current generates a magnetic flux that opposes the generating flux. This flux in turn induces a voltage both in the receiver loop, $v_{rr}(t)$, and in the transmitter loop, $v_{tr}(t)$. These two voltages oppose the voltages $v_{tt}(t)$ and $v_{rt}(t)$. Figure 3.14 shows the positions of the voltages for a general transmission system in the gyrator equivalent circuit.

Knowing these voltages, the terminal voltages of the two conductor loops can be determined by

$$v_t(t) = v_{tt}(t) - v_{tr}(t) = L_t \frac{\mathrm{d}i_t(t)}{\mathrm{d}t} - M \frac{\mathrm{d}i_r(t)}{\mathrm{d}t} \tag{A.23}$$

$$v_r(t) = v_{rt}(t) - v_{rr}(t) = M \frac{\mathrm{d}i_t(t)}{\mathrm{d}t} - L_r \frac{\mathrm{d}i_r(t)}{\mathrm{d}t} \tag{A.24}$$

This pair of equations is referred to as the lossless transformer equations. Here, the passive sign convention was chosen for the transmitter loop and the active (generator) sign convention for the receiver loop. This agrees with the directions of the induced voltages and of the currents. The literature often uses an alternative representation in which the passive sign convention is chosen for both the transmitter and the receiver loop. In this case, the subtractions in (A.23) and (A.24) each become additions. Note that the receiver current is then negative when a load is connected.

In the frequency domain, using complex amplitudes, the lossless transformer equations (A.23) and (A.24) can be written directly as

$$\begin{bmatrix} \boldsymbol{V}_t \\ \boldsymbol{V}_r \end{bmatrix} = \begin{bmatrix} j\omega L_t & -j\omega M \\ j\omega M & -j\omega L_r \end{bmatrix} \begin{bmatrix} \boldsymbol{I}_t \\ \boldsymbol{I}_r \end{bmatrix} \tag{A.25}$$

This system of equations already has the form of the desired impedance matrix (3.3).

So far, losses have been neglected; they are considered in the following section.

A.1.3. Losses

Losses arise in the resistances of the copper windings and, if present, in a core or shield in the form of hysteresis and eddy-current losses. They depend on the currents flowing.

A current in one conductor loop, with no current in the other, causes frequency-dependent copper and magnetization losses. In a conventional transformer, for example, an alternating current in one winding causes resistive losses that are frequency-dependent owing to the skin and proximity effects. The current also produces a magnetic flux, which causes frequency- and magnetization-dependent losses in the core. Furthermore, eddy currents are induced in any shields and in the second winding, which also contribute to the total losses. For the transmitter loop, for example, the sum of all these current-dependent losses can be represented by a loss resistance denoted R_{tt}. By the same reasoning, the loss resistance R_{rr} of the receiver loop can be introduced.

As with the total magnetic flux, the losses are also influenced by the simultaneous current flow in both coupled conductor loops. In a transformer, for example, a neighboring current may increase the resistance of a loop owing to the proximity effect. This increases the losses. A beneficial effect can occur in the core, for example: since the magnetic fluxes superimpose, the total core flux can decrease, depending on the current direction. This reduces the magnetization losses. Because of reciprocity, this interaction can be described by a common loss resistance R_{tr}.

Accordingly, the lossless model (A.25) can be extended to the general transformer equations

$$\begin{bmatrix} \boldsymbol{V}_t \\ \boldsymbol{V}_r \end{bmatrix} = \begin{bmatrix} R_{tt} + j\omega L_t & -(R_{tr} + j\omega M) \\ R_{tr} + j\omega M & -(R_{rr} + j\omega L_r) \end{bmatrix} \begin{bmatrix} \boldsymbol{I}_t \\ \boldsymbol{I}_r \end{bmatrix} \tag{A.26}$$

(A.26) is the desired impedance matrix, and the required coefficients can be read directly by comparison with (3.3). When describing air-core coils, the loss resistance R_{tr} can often be neglected. In individual cases, this can be checked by measurement according to Section B.1.

A.1.4. Impedance Matrix

The complete impedance model of the inductive coupling can be derived from the relationships shown. The following specifications refer to Figure A.2.

Parameter	Variable	Value
Loop radius	r_L	25.23 mm
Wire diameter	d	0.8 mm
Distance	g	1.5 mm

The two conductor loops are of identical design. Using (A.14), the two self-inductances L_t and L_r can therefore be calculated as

$$L_t = L_r = 132.62\,\text{nH} \tag{A.27}$$

The mutual inductance M can be calculated according to (A.19):

$$M = 90.05\,\text{nH}\ , \tag{A.28}$$

from which, according to (A.22), the overall magnetic coupling factor

$$k_X = 0.68 \tag{A.29}$$

can be calculated. From (A.27) and (A.28), at the specified frequency of 150 kHz, the three reactances

$$X_{tt} = X_{rr} = \omega L_t = 124.99\,\text{m}\Omega \tag{A.30}$$

and

$$X_{tr} = \omega M = 84.87\,\text{m}\Omega\ . \tag{A.31}$$

follow.

Since the loops are spaced well apart and each has only a single turn, proximity-effect losses can be neglected. Furthermore, there is neither a shield nor a core, so that the loss resistance R_{tr} can also be neglected according to Section A.1.3. Under these assumptions, only the resistive losses of the winding need to be taken into account. The frequency dependence of these losses is then limited to the skin effect, which can be approximated using the well-known skin depth [60]

$$\delta(\omega) = \sqrt{\frac{2\rho}{\omega\mu}} \tag{A.32}$$

With this skin depth, the resistance of a circular loop made of a cylindrical conductor is

$$R(\omega) = \begin{cases} 2\dfrac{\rho\, r_L}{\delta(\omega)d - \delta(\omega)^2} & \text{for } 2\delta(\omega) < r_L \\ 8\dfrac{\rho\, r_L}{d^2} & \text{otherwise} \end{cases}\ . \tag{A.33}$$

The litz wire used for the practical implementation of the winding consists of 30 insulated strands with a strand diameter of 0.1 mm. With this strand diameter, the

resistance can be regarded as frequency-independent up to approximately 1.8 MHz. According to (A.33), with the resistivity of copper $\rho = 0.0178\,\Omega\,\mathrm{mm}^2/\mathrm{m}$ [60], at the frequency of interest

$$R_{tt} = R_{rr} = 12\,\mathrm{m}\Omega\ . \tag{A.34}$$

All quantities are now known. The impedance matrix is

$$\mathcal{Z}_I = \begin{bmatrix} 12\,\mathrm{m}\Omega + j124.99\,\mathrm{m}\Omega & -j84.87\,\mathrm{m}\Omega \\ j84.87\,\mathrm{m}\Omega & -\left(12\,\mathrm{m}\Omega + j124.99\,\mathrm{m}\Omega\right) \end{bmatrix}\ . \tag{A.35}$$

(A.35) provides the inductive example used in Chapters 3 and 4. Note, however, that it is valid only at the fixed frequency of 150 kHz.

A.2. Capacitive System

This section derives the impedance matrix of a capacitive power transfer system. Unlike

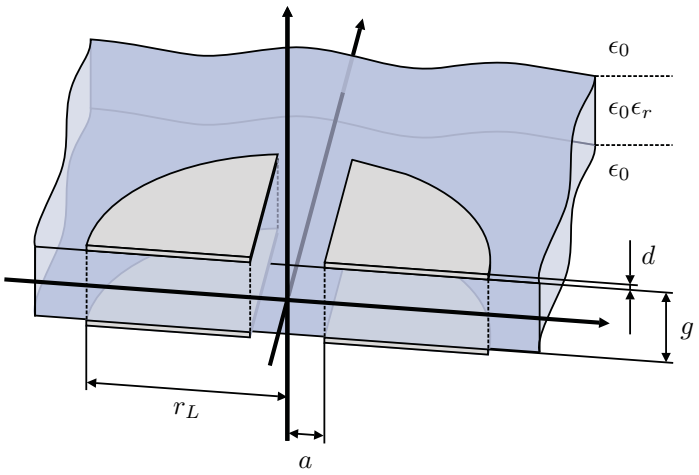

Figure A.8.: *Example system for capacitive coupling*

inductive power transfer, capacitive power transfer takes place not in a solenoidal field but in an irrotational field with sources, i.e., a quasi-electrostatic field. Consequently, the transfer requires a closed circuit consisting of a forward and a return path. This path is realized by two separate electrodes on each side. Figure A.8 shows the defined system. A complete illustration is shown in Figure A.1(b) on page 87. Both the transmitter and the receiver have two copper electrodes shaped as circular segments. In the nominal case, these electrodes overlap exactly. For easier handling, the electrodes are mounted on an FR4 substrate, which at the same time serves as the dielectric between transmitter and receiver.

The connection between transmitter and receiver can be interpreted as two coupling capacitors, C_{c_1} and C_{c_2}, in the forward and return conductors, respectively. In addition to these two capacitors, there is a parasitic capacitive coupling C_{lt} between the two transmitter-side electrodes. The same applies to the receiver-side electrodes with C_{lr}. These two capacitors are referred to below as leakage capacitors. This leads to the model in Figure A.9.

The four capacitors in Figure A.9 are lossy. In general, a series loss resistance can be assigned to each of them. It is already apparent that the leakage capacitors will have a significant influence on the efficiency of the power transfer. If these capacitors are neglected, the transfer quality factor of the transmission system according to Section 3.1.1 tends toward infinity with increasing load resistance, as is usual for a simple series connection. According to (3.26), the possible efficiency then tends toward one.

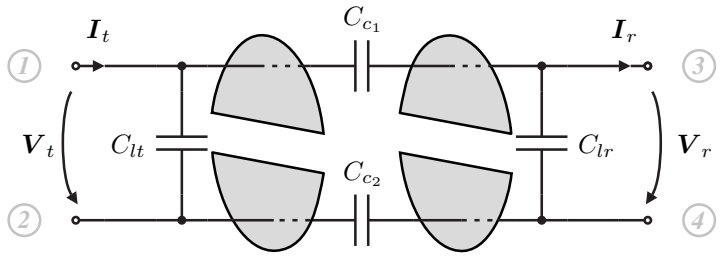

Figure A.9.: *First model of the capacitive coupling*

The four capacitors and their loss resistances are determined next, using a method presented in [61]: specific short-circuit configurations of the two-port are used to determine the capacitances analytically or by measurement. To illustrate the short circuits, the terminals in Figure A.9 are numbered. The method relies on the geometric symmetry of the chosen arrangement. For example, when terminals 1 and 2 as well as terminals 3 and 4 are short-circuited, the parallel connection of the capacitors C_{c_1} and C_{c_2} is accessible from outside. Since the setup is symmetric and the transmitter- and receiver-side electrodes are identical, the two capacitors are also equal. Consequently, the parallel connection also yields the individual capacitances. An equivalent method was presented in [19].

A.2.1. Coupling Capacitors

Figure A.10 shows one of the two coupling capacitors in gray. Because of the geometric symmetry, the second one, drawn dashed, has the same value. After simultaneously

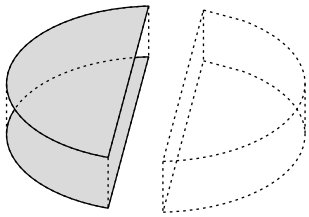

Figure A.10.: *Position of the coupling capacitor C_{c_1}. The identical capacitor C_{c_2} is drawn dashed.*

short-circuiting terminals 1 and 2 as well as terminals 3 and 4 in Figure A.9, the coupling capacitors C_{c_1} and C_{c_2} become accessible for measurement. In this case, the leakage capacitors C_{lt} and C_{lr} are short-circuited and the coupling capacitors are connected in parallel.

Since the ratio of the total electrode area to the edge region is very large, fringing effects have only a minor influence on the total capacitance. Neglecting them, the simple ge-

ometry allows the externally measurable capacitance in this short-circuit configuration to be determined directly from the well-known parallel-plate formula

$$C_{12|34} = C_{c_1} \parallel C_{c_2} = 2\epsilon_0\epsilon_r \frac{1}{g}\left(r_L^2 \arccos\left(\frac{a}{r_L}\right) - a\sqrt{r_L^2 - a^2}\right) \tag{A.36}$$

The expression in parentheses is the area of the circular-segment electrode according to [58]. The subscript indicates that terminals 1 and 2 as well as terminals 3 and 4 are short-circuited.

A.2.2. Leakage Capacitors

The leakage capacitors between the electrodes are derived using conformal mapping [62, 63, 64, 65]. Conformal mapping transforms the original geometry in the $\boldsymbol{z}$ plane into a corresponding geometry in a newly defined $\boldsymbol{w}$ plane that is easier to analyze. This is illustrated schematically in Figure A.11. Since capacitance is invariant under

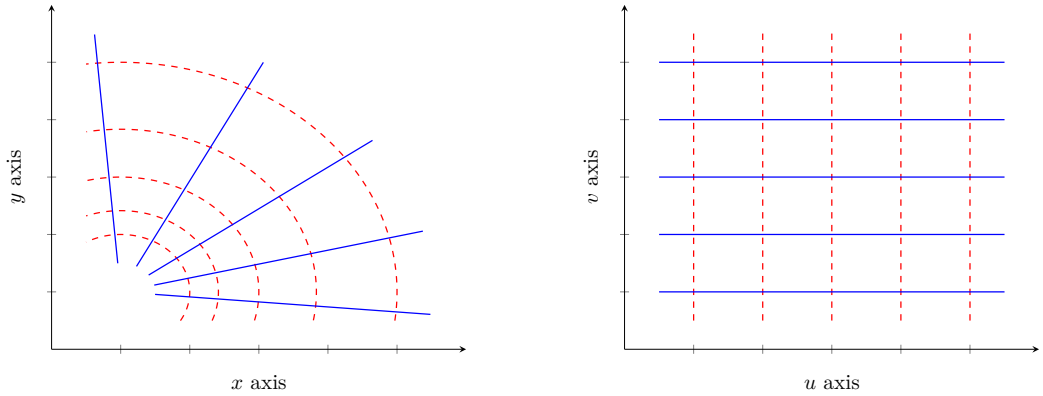

(a) Original geometry in the $\boldsymbol{z}$ plane (b) Mapped geometry in the $\boldsymbol{w}$ plane

Figure A.11.: *Difficult-to-analyze original geometry and its simplified mapping*

conformal mapping, it can be determined in either plane. If the capacitance between two electrodes of the original geometry is difficult to obtain, conformal mapping is therefore a suitable approach: it converts the original geometry into a structure whose capacitance is easier to calculate [63]. This simplified structure is usually a parallel-plate capacitor.

Since the method is restricted to two-dimensional problems, the planes in Figure A.11 can be represented in the complex plane $\mathbb{C}$. For an arbitrary point in the two planes,

$$\boldsymbol{z} = x + jy \tag{A.37}$$

$$\boldsymbol{w} = u + jv\ . \tag{A.38}$$

In many cases, the two-dimensional result must then be converted to the actual three-dimensional geometry.

Conformality means that the mapping function is analytic (complex differentiable), which preserves angles. If Figure A.11(a) is interpreted as a representation of potential and stream functions, conformal mapping makes it possible to map an inhomogeneous field in $\boldsymbol{z}$ onto a homogeneous field in $\boldsymbol{w}$. Because angles are preserved, the orthogonality between potential and stream functions is maintained after the mapping.

Conformal mapping can only be applied to planar field problems that are free of sources and vortices. Because of the necessary conversion to the three-dimensional geometry, the results presented here are only approximations. Near the edges in particular, the finite element method yields more accurate results, but it often lacks the direct link between theoretical analysis and practical setup.

According to [61], the parallel connection of the two leakage capacitors C_{lt} and C_{lr} is accessible by simultaneously short-circuiting terminals 1 and 3 as well as terminals 2 and 4 in Figure A.9:

$$C_{13|24} = C_{lt} \parallel C_{lr} \ . \tag{A.39}$$

The coupling capacitors are short-circuited. As a result, each pair of opposing electrodes in Figure A.10 is at the same potential. Assuming that the region between these electrodes is then also at approximately the same potential, the volume enclosed by the short-circuited electrodes can be regarded as an equipotential body. This is shown in Figure A.12, which depicts a cross section through the two equipotential bodies shaded in gray.

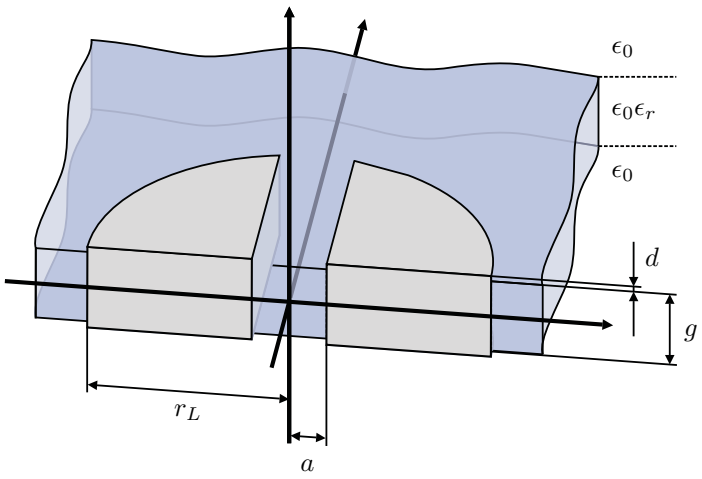

Figure A.12.: *Equipotential bodies in different dielectrics*

Figure A.12 further shows that the two symmetric bodies are embedded in an environment of different dielectrics. For the conformal-mapping analysis, the capacitance

between the bodies must therefore be calculated as two partial capacitors in parallel. The first of these partial capacitors is the surface leakage capacitor $C_{13|24P}$, which lies entirely outside the substrate. In Figure A.12, one half of this capacitor lies above and the other half below the equipotential bodies shown, in the region with permittivity $\epsilon = \epsilon_0$. The second, lossy partial capacitor is called the lateral leakage capacitor $C_{13|24S}$ and lies entirely within the substrate, where the permittivity is $\epsilon = \epsilon_0\epsilon_r$. Their positions are shown again in Figures A.13(a) and A.16(a).

Surface Leakage Capacitor

Figure A.13(a) shows two electrodes of the surface leakage capacitor. They bound the upper region of the two equipotential bodies described above. The lower boundary of the equipotential bodies is drawn dashed and is formed by the two remaining electrodes. Since the upper and lower electrodes are short-circuited in this analysis and the region between them is treated separately, each upper and lower electrode pair can be combined into a single electrode. The result is a surface capacitor according to Figure A.13(b).



(a) Position of the upper surface leakage capacitor

(b) Combination of the upper and lower surface leakage capacitors

Figure A.13.: *Position of the surface leakage capacitor and combination*

If the electrodes shown in Figure A.13(b) are approximated by two infinitely extended half-planes at $y = 0$, separated by a distance of $2a$ symmetrically about the y axis, the field can be described by a trigonometric mapping. In this case, following [65], the mapping function

$$\boldsymbol{z}(\boldsymbol{w}) = a\cos(\boldsymbol{w}) \tag{A.40}$$

is used. Alternative trigonometric mappings can be found, for example, in [61] or [63]. (A.40) maps the two half-planes in $\boldsymbol{z}$ onto an infinitely extended parallel-plate capacitor in $\boldsymbol{w}$. Figure A.14 A.14(a) shows the field of the two half-planes, and Figure A.14 A.14(b) that of the parallel-plate capacitor. The arrows on the electrodes indicate that they extend to infinity in the corresponding direction.

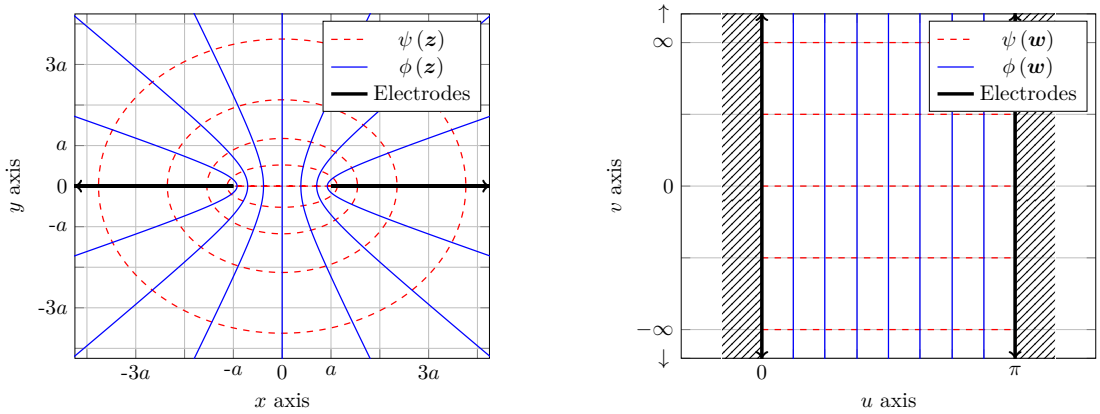

(a) Field of the surface leakage capacitor in $\boldsymbol{z}$

(b) Field of the surface leakage capacitor in $\boldsymbol{w}$

Figure A.14.: *Field plot of the surface leakage capacitor*

The domain is

$$D_{\boldsymbol{w}} \coloneqq \left\{(u,v) \in \mathbb{R}^2 \,|\, 0 \leq u \leq \pi\right\} \ . \tag{A.41}$$

Figure A.14(b) shows the familiar equipotential lines ϕ of the parallel-plate capacitor and the stream function ψ orthogonal to them. Here, an equipotential line can be drawn as $\boldsymbol{w}(u_c, v)$, where u_c is an arbitrary constant subject to (A.41). A scaling factor establishes the relationship between the position in $\boldsymbol{w}$ and the actual voltage. Assuming that the left plate is at potential ϕ_0 and the right plate at potential ϕ_1, then, with (A.38), the potential at any position between the two plates is given by the linear relationship

$$\phi(\boldsymbol{w}) = \underbrace{\frac{\phi_1 - \phi_0}{\pi}}_{\text{scaling factor}} u = \frac{\phi_1 - \phi_0}{\pi} \operatorname{Re} \boldsymbol{w} \tag{A.42}$$

Alternatively, following [65], the scaling factor can be determined by integrating the one-dimensional Laplace equation and then comparing coefficients. This is confirmed by [63], according to which the scaling factor of a parallel-plate capacitor always equals the potential difference divided by the plate spacing.

With the same scaling factor, the stream function, analogous to (A.42), is

$$\psi(\boldsymbol{w}) = \frac{\phi_1 - \phi_0}{\pi} v = \frac{\phi_1 - \phi_0}{\pi} \operatorname{Im} \boldsymbol{w} \ . \tag{A.43}$$

Once the scaling factor and the stream function are known, the surface charge per unit length in the z direction between two points on surfaces of constant potential can be determined from the difference of the stream function, according to [65]. Here, z is

the three-dimensional coordinate, not the complex variable $\boldsymbol{z}$ according to (A.37), and points into the page in Figure A.14(a):

$$q'_F \, \mathrm{d}z = \epsilon \left(\psi(\boldsymbol{w}_1) - \psi(\boldsymbol{w}_2) \right) \, \mathrm{d}z \; . \tag{A.44}$$

From (A.40) and (A.37) it follows directly that

$$\boldsymbol{w}(\boldsymbol{z}) = \arccos\left(\frac{\boldsymbol{z}}{a}\right) \; , \tag{A.45}$$

which, substituted together with (A.43) into (A.44), yields

$$q'_F \, \mathrm{d}z = \epsilon \frac{\phi_1 - \phi_0}{\pi} \left[\mathrm{Im}\left(\arccos\left(\frac{\boldsymbol{z}_1}{a}\right)\right) - \mathrm{Im}\left(\arccos\left(\frac{\boldsymbol{z}_2}{a}\right)\right)\right] \, \mathrm{d}z \tag{A.46}$$

Figure A.14(a) shows that the two half-planes, each at constant potential, are located at $y = 0$. The goal is to calculate the surface charge between a point on the left half-plane and the corresponding point, mirrored about the y axis, on the right half-plane. With these specifications and the identity $\arccos(-x) = \pi - \arccos(x)$ [58], (A.46) can be rearranged with (A.37) to

$$q'_F \, \mathrm{d}z = 2\epsilon \frac{\phi_1 - \phi_0}{\pi} \, \mathrm{Im}\left(\arccos\left(\frac{x}{a}\right)\right) \, \mathrm{d}z \tag{A.47}$$

To determine the capacitance between the actual electrodes, (A.47) must be integrated over the entire area of one electrode and divided by the potential difference. This requires a two-dimensional integration in the xz plane, taking into account the position-dependent width of the electrode in the z direction. This width equals half the chord of a circular segment and can be calculated according to [58] by

$$z_e(x) = \sqrt{r_L^2 - x^2} \tag{A.48}$$

The area to be integrated and (A.48) are shown in part in Figure A.15.

From (A.47) and (A.48), the surface capacitance is

$$C_{13|24P} = \int_a^{r_L} \int_{-z_e(x)}^{z_e(x)} \frac{\mathrm{d}}{\mathrm{d}x} q'_F \, \mathrm{d}z \, \mathrm{d}x = \frac{4\epsilon}{\pi} \int_a^{r_L} \frac{\sqrt{r_L^2 - x^2}}{\sqrt{x^2 - a^2}} \, \mathrm{d}x \, . \tag{A.49}$$

Calculating (A.49) requires an elliptic integral. Following [61], approximating the electrode width (A.48) by

$$z_e(x) \approx r_L - \frac{x^3}{r_L^2} \tag{A.50}$$

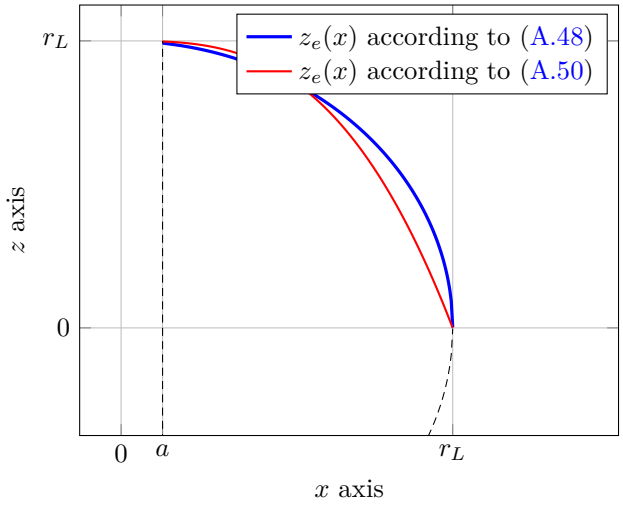

Figure A.15.: *Integration over the electrode area*

and further assuming that $r_L \gg a$, (A.49) can be approximated by the function

$$C_{13|24P} \approx \frac{4\epsilon r_L}{\pi}\left[\ln(4r_L) - \ln(2a) - \frac{1}{3}\right] \tag{A.51}$$

Figure A.15 shows that the approximation of the electrode width (A.50) agrees well with the actual electrode edge (A.48), particularly in the region of the gap. The difference increases only farther away from the gap, where the larger electrode spacing makes the contribution to the total capacitance small, so the deviation has only a minor effect on the overall result. Consequently, the error of (A.51) compared to the actual surface capacitance (A.49) is also small.

Lateral Leakage Capacitor

The lateral leakage capacitor is shown in Figure A.16(a). It lies entirely within the substrate. A suitable mapping function would simplify the calculation here as well, but none is known, and deriving one is difficult because of the rounded edges. The geometry must therefore be simplified.

Figure A.16(a) suggests that most of the total lateral leakage capacitance results from the two inner, closely spaced facing surfaces of the two equipotential bodies, and that the outer quarter-circle regions contribute little. This justifies an approximation by two right-angled edges according to Figure A.16(b), for which a mapping function can be derived using the Schwarz-Christoffel polygon mapping [63, 64].

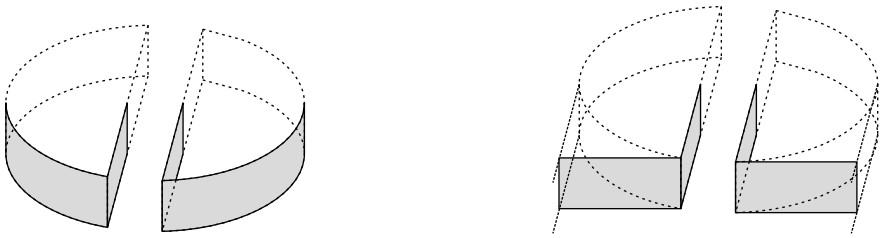

(a) Lateral leakage capacitor

(b) Approximation of the lateral leakage capacitor

Figure A.16.: *Position of the lateral leakage capacitor and chosen approximation*

In this thesis, as in the cited literature, the mapping function is derived via three different planes. As before, the original geometry is described in the $\boldsymbol{z}$ plane. This plane can be transformed onto the real t axis of an intermediate plane by

$$\boldsymbol{z}(t) = A \int \prod (t - t_i)^{-\frac{\alpha_1}{\pi}} \, \mathrm{d}t + B \tag{A.52}$$

In a third step, (A.52) is mapped onto the upper half of the auxiliary $\boldsymbol{w}$ plane by homogenization. The field there is homogeneous and can again be described by a parallel-plate capacitor.

The right-angled approximation is shown in Figure A.17. The two electrodes are positioned symmetrically about the axis in the $\boldsymbol{z}$ plane, with the approximated outer region defined at $y = 0$. Here, too, the arrows on the electrodes indicate that they extend to infinity.

The Schwarz-Christoffel polygon mapping assumes that a polygon consisting of several straight segments encloses a connected region. Adjacent segments meet at a vertex characterized by an angle. A vertex can also lie at infinity, in which case its angle is referred to as an exterior angle. This makes it possible to interpret the two separate electrodes in Figure A.17 as a polygon closed at infinity. For this purpose, all angles of the polygon in Figure A.17 are labeled. The angles α_0 and α_2 are exterior angles. They close the polygon at infinity and thus establish the virtual connection between the two electrodes, which are generally at different potentials. In a second step, this polygon is traversed in the mathematically positive direction, starting at α_0, and mapped onto the real t axis of the intermediate plane. One complete traversal in $\boldsymbol{z}$ corresponds to an increase from $t = -\infty$ to $t = \infty$ on the t axis.

For a polygon with only three vertices, the positions of the vertices on the t axis can be chosen freely. For four vertices, this is generally not the case: only three positions can be chosen freely, and the fourth follows from the geometry and the choices already made. This is where the symmetric placement of the coordinate axes in $\boldsymbol{z}$ (Figure A.17) pays

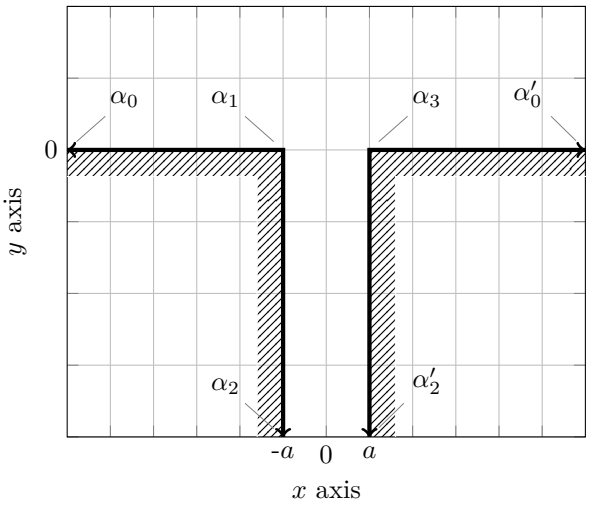

Figure A.17.: *Approximation of the lateral leakage capacitor by two right-angled electrodes, shown in the $\boldsymbol{z}$ plane*

off. This symmetry is preserved in the intermediate plane, so that, after an arbitrary choice of the first three positions, the symmetric fourth position follows as well.

According to [63], it is convenient to place the two potential jumps α_0 and α_2 on the t axis at $t = -\infty$ or $t = \infty$ and at $t = 0$, respectively. α_1 is placed arbitrarily at $t = -1$. As described above, owing to the axial symmetry, this definition also fixes the position of α_3 at $t = 1$. Figure A.18 shows the intermediate plane.

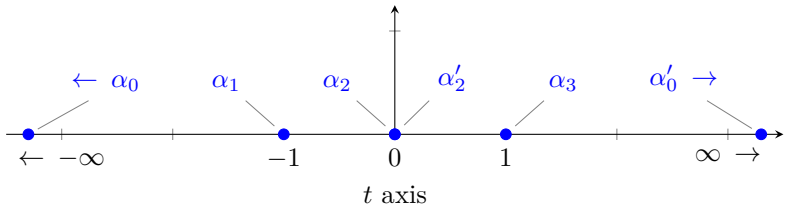

Figure A.18.: *Intermediate plane with the polygon angles placed on the t axis*

From Figures A.17 and A.18, using (A.52), the mapping from the $\boldsymbol{z}$ plane to t can be given. With $\alpha_0 = 2\pi$, $\alpha_1 = -\pi/2$, $\alpha_2 = \pi$, and $\alpha_3 = -\pi/2$,

$$\boldsymbol{z}(t) = A \int \frac{(t+1)^{\frac{1}{2}}\,(t-1)^{\frac{1}{2}}}{t}\,\mathrm{d}t + B\,, \tag{A.53}$$

from which, after indefinite integration,

$$\boldsymbol{z}(t) = A\left[\sqrt{t-1}\sqrt{t+1} - 2\arctan\left(\frac{\sqrt{t-1}}{\sqrt{t+1}}\right)\right] + B \tag{A.54}$$

can be calculated. The constants A and B are not yet known. Intuitively, these constants rotate the polygon, so far described only by its angles, into its actual orientation and scale it to its actual size. They can usually be derived from the representation in $\boldsymbol{z}$ (Figure A.17 on page 110). For example, substituting the positions of the inner angles α_1 and α_3 of the intermediate plane into (A.54) and using

$$\lim_{x\to\infty} \arctan x = \pi/2 \tag{A.55}$$

immediately yields

$$\boldsymbol{z}(1) = B \tag{A.56}$$

$$\boldsymbol{z}(-1) = B - \pi A\,. \tag{A.57}$$

Since the two angles were placed on the y axis in the $\boldsymbol{z}$ plane and their x positions correspond to plus and minus half the distance a between the two electrodes, (A.56) yields

$$B = a\,, \tag{A.58}$$

which, substituted into (A.57), gives the second constant

$$A = \frac{2a}{\pi} \tag{A.59}$$

The mapping from the $\boldsymbol{z}$ plane to the intermediate plane is thus known and can be carried over to the final $\boldsymbol{w}$ plane by homogenization. Assuming that the two electrodes of the parallel-plate capacitor in the $\boldsymbol{w}$ plane are separated by a distance of π, homogenization according to [63] only requires replacing t in (A.54) by

$$t \coloneqq e^{\boldsymbol{z}} \tag{A.60}$$

Thus, analogous to (A.40), the mapping of the $\boldsymbol{w}$ plane into the $\boldsymbol{z}$ plane is given, with (A.54), (A.58), (A.59), and (A.60), by

$$\boldsymbol{z}(\boldsymbol{w}) = \frac{2a}{\pi}\left[\sqrt{e^{\boldsymbol{w}}-1}\sqrt{e^{\boldsymbol{w}}+1} - 2\arctan\left(\frac{\sqrt{e^{\boldsymbol{w}}-1}}{\sqrt{e^{\boldsymbol{w}}+1}}\right)\right] + a\,. \tag{A.61}$$

Here, too, the domain is

$$D_{\boldsymbol{w}} \coloneqq \left\{(u,v) \in \mathbb{R}^2 \,|\, 0 \le v \le \pi\right\} \tag{A.62}$$

Figure A.19 shows the parallel-plate capacitor and the mapping found. The equipotential lines and stream lines drawn between the electrodes of the parallel-plate capacitor in Figure A.19(b) are equidistant and were transferred to the $\boldsymbol{z}$ plane using (A.61). There, the spacing of the stream lines confirms the assumption made above and that most of the capacitance is determined by the gap rather than by the outer region.

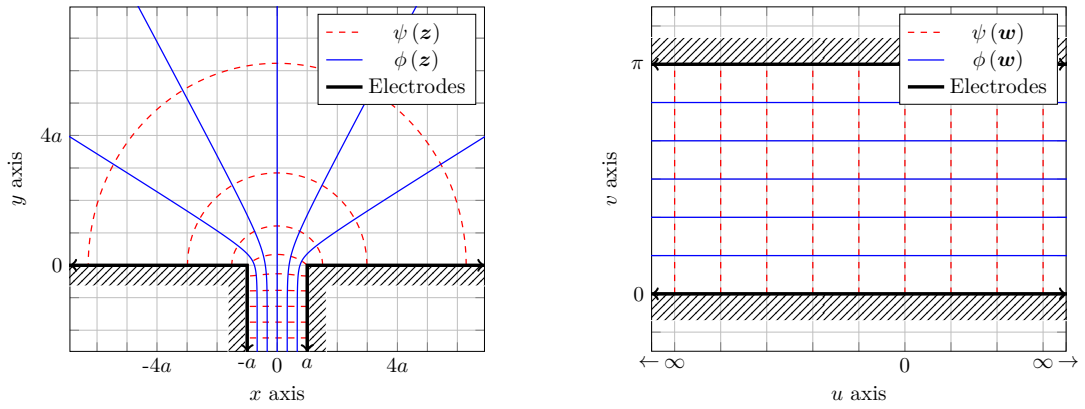

(a) Field of the lateral leakage capacitor in $\boldsymbol{z}$

(b) Field of the lateral leakage capacitor in $\boldsymbol{w}$

Figure A.19.: *Field plot of the lateral leakage capacitor*

In principle, the surface charge and the capacitance can again be calculated with (A.44). The difficulty here, however, is that, unlike (A.40) and (A.45), no inverse function of (A.61) can be given. A numerical evaluation in $\boldsymbol{w}$ is therefore unavoidable.

The two electrodes of the parallel-plate capacitor are located at $v = 0$ and $v = \pi$. To determine the capacitance, the spatial dimensions of the actual electrodes in the $\boldsymbol{z}$ plane must now be transferred to the $\boldsymbol{w}$ plane. It can be shown that the angles α_1 and α_3 of Figure A.17 are located at $u = 0$ in the $\boldsymbol{w}$ plane. The electrodes are symmetric about the y axis. Consequently, only the positive value u_p and the negative value u_n according to Figure A.20 need to be found to describe the electrodes. The corresponding points according to (A.61) and (A.38) are marked there.

By geometric comparison with Figure A.12 on page 104 and Figure A.16 on page 109, the two equations

$$\operatorname{Re} \boldsymbol{z}(u_p) = r_L \tag{A.63}$$

$$\operatorname{Im} \boldsymbol{z}(u_n) = z_e(a) \tag{A.64}$$

must be solved numerically for the right electrode in Figure A.20, where $z_e(a)$ is half the width of the electrode at the air gap according to the circular segment (A.48). With u_p and u_n known, the desired capacitance follows from the simple parallel-plate formula:

$$C_{13|24S} = \epsilon \frac{(u_p - u_n)\, g}{\pi} \,. \tag{A.65}$$

An approximation can be given here as well. The gap between the equipotential bodies is approximated as a simple parallel-plate capacitor without fringing effects, and the

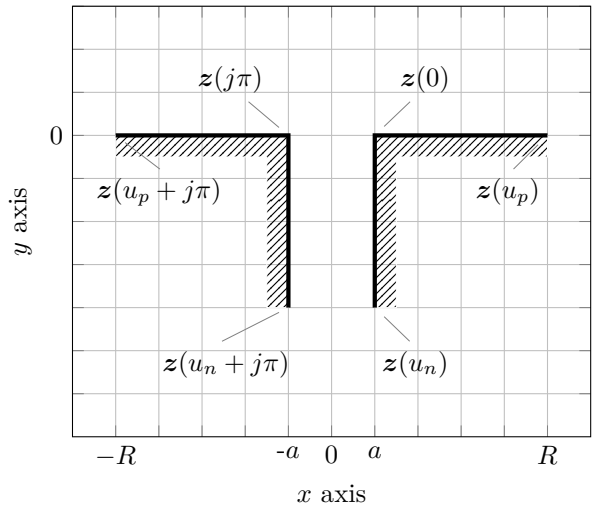

Figure A.20.: *Correspondence of the vertices in $\boldsymbol{z}$ to the $\boldsymbol{w}$ plane*

region outside it as a surface leakage capacitor according to Section A.2.2. With (A.47) and (A.48), and analogous to (A.49), this yields

$$\begin{aligned} C_{13|24S} &\approx \epsilon \frac{z_e(a) g}{a} + \int_a^{r_L} \int_0^g \frac{\mathrm{d}}{\mathrm{d}x} q'_F \,\mathrm{d}z \,\mathrm{d}x \\ &\approx \epsilon\, g \left[\frac{z_e(a)}{a} + \frac{2}{\pi} \ln\left(r_L + \sqrt{r_L^2 - a^2} \right) - \frac{2}{\pi} \ln(a) \right] . \end{aligned} \tag{A.66}$$

In the lossless case, the leakage capacitances follow directly from the parallel connection of $\frac{1}{2}C_{13|24p}$ and $\frac{1}{2}C_{13|24S}$ according to (A.49) and (A.65). Since these two capacitors have different dielectrics, however, in the lossy case they can only be combined once their respective loss resistances are taken into account.

A.2.3. Losses

The loss resistance of a capacitor can be determined from the dissipation factor of the respective dielectric. In general, for a series loss resistance of a capacitor C,

$$ESR = \frac{DF}{\omega C} , \tag{A.67}$$

from which the impedance of the capacitor in series with its loss resistance is

$$\boldsymbol{Z} = \frac{1}{\omega C} (DF - j) \tag{A.68}$$

An admittance description is often convenient as well; from (A.68) it follows directly that

$$\boldsymbol{Y} = \frac{\omega C}{DF - j} \,. \tag{A.69}$$

A.2.4. Impedance Matrix

To determine the capacitors and the loss resistances, the relative permittivity ϵ_r and the dissipation factor DF of the FR4 substrate used must be known. [66] determined both as functions of frequency and temperature; the values at 300 K and 150 kHz are used here.

With (A.36), (A.49), and (A.65), all capacitances required for the impedance matrix are known. The following values apply, referring to Figure A.8 on page 101; the radius and the transmitter-receiver distance are the same as for the inductive system.

Parameter	Variable	Value
Outer radius of the electrodes	r_L	25.23 mm
Electrode thickness	d	35 µm
Half the distance between electrodes	a	1.984 mm
Distance	g	1.5 mm
Relative permittivity	ϵ_r	5.52
Dissipation factor	DF	0.014

With these values, (A.36) yields the capacitance of the short-circuited coupling capacitors:

$$C_{12|34} = 58.643\,\text{pF} \,. \tag{A.70}$$

For the short-circuited leakage capacitors $C_{13|24}$, (A.49) yields the capacitance of the surface leakage capacitor

$$C_{13|24P} = 0.816\,\text{pF} \tag{A.71}$$

and (A.65) the capacitance of the lateral leakage capacitor

$$C_{13|24S} = 1.083\,\text{pF} \tag{A.72}$$

Since the transmitter- and receiver-side electrodes are identical, the capacitances can be assigned as in Figure A.21, i.e., without the short-circuit configurations from Sections A.2.1 and A.2.2. There are several ways to convert this lossless model into a lossy impedance matrix. Here, an admittance matrix is used as an intermediate step: the

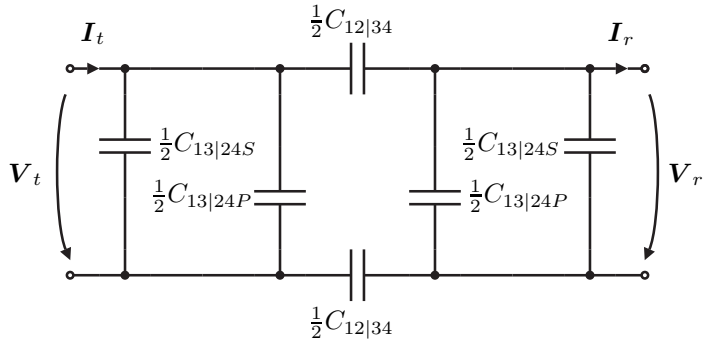

Figure A.21.: *Lossless equivalent circuit of the capacitive coupling*

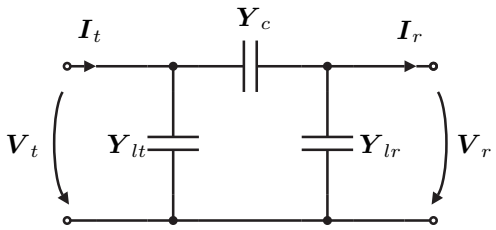

Figure A.22.: Π *model of the capacitive coupling*

general Π admittance model in Figure A.22 is defined first, and its admittances are then determined by comparison with Figure A.21.

The comparison shows that the admittances $\boldsymbol{Y}_{lt}$ and $\boldsymbol{Y}_{lr}$ can each be regarded as the parallel connection of the capacitors $\frac{1}{2}C_{13|24P}$ and $\frac{1}{2}C_{13|24S}$. Note that the two capacitors have different dielectrics: the surface leakage capacitor lies outside the substrate and the lateral leakage capacitor entirely within it. Consequently, losses occur only in the lateral leakage capacitor. Taking the dissipation factor into account according to (A.69), at a frequency of 150 kHz,

$$\boldsymbol{Y}_{lt} = \boldsymbol{Y}_{lr} = \frac{\omega}{2}\left(\frac{C_{13|24P}}{-j} + \frac{C_{13|24S}}{DF - j}\right) = 7.14\,\text{nS} + j894.63\,\text{nS}\,. \tag{A.73}$$

In the two-port view, the series admittance $\boldsymbol{Y}_c$ can be regarded as the series connection of the two remaining lossy capacitors, each with capacitance $\frac{1}{2}C_{12|34}$. The total capacitance is therefore halved again. The admittance is therefore

$$\boldsymbol{Y}_c = \frac{\omega}{4}\frac{C_{12|34}}{DF - j} = 193.41\,\text{nS} + j13.82\,\mu\text{S}\,. \tag{A.74}$$

According to [46], with (A.73) and (A.74), the admittance matrix of the Π structure

in Figure A.22 is given by

$$\mathcal{Y}_K = \begin{bmatrix} Y_{lt} + Y_c & -Y_c \\ Y_c & -(Y_{lr} + Y_c) \end{bmatrix} \tag{A.75}$$

This admittance matrix can be transformed into an impedance matrix according to [46]:

$$\mathcal{Z}_K = \frac{1}{\frac{1}{Y_{lt}} + \frac{1}{Y_c} + \frac{1}{Y_{lr}}} \begin{bmatrix} \frac{1}{Y_{lt}}\left(\frac{1}{Y_c} + \frac{1}{Y_{lr}}\right) & -\frac{1}{Y_{lt}Y_{lr}} \\ \frac{1}{Y_{lt}Y_{lr}} & -\frac{1}{Y_{lr}}\left(\frac{1}{Y_c} + \frac{1}{Y_{lt}}\right) \end{bmatrix} \tag{A.76}$$

from which, after substituting the values found, the desired impedance matrix

$$\mathcal{Z}_K = \begin{bmatrix} 4.71\,\mathrm{k\Omega} - j576.38\,\mathrm{k\Omega} & -(4.22\mathrm{k\Omega} - j541.33\,\mathrm{k\Omega}) \\ 4.22\mathrm{k\Omega} - j541.33\,\mathrm{k\Omega} & -(4.71\,\mathrm{k\Omega} - j576.38\,\mathrm{k\Omega}) \end{bmatrix} \tag{A.77}$$

can be calculated. An alternative derivation of (A.77) from Figure A.22 is possible with (B.22) and (B.4).

(A.77) provides the capacitive example used in Chapters 3 and 4. Like the inductive example, it is valid only at 150 kHz.

B. Two-Port Parameters

For more complex systems with one input port and one output port, network analysis with two-port parameters is convenient, as it allows the complete transfer characteristics to be derived systematically. The network to be described must have the following properties:

- At each port, the current entering one terminal must equal the current leaving the other terminal.
- The network must be linear. Nonlinear components may need to be linearized.
- The network must be stable. In this context, this means that the two-port must not contain any independent sources. Sources controlled by internal voltages or currents, however, are permissible.
- All currents and voltages are sinusoidal. This does not restrict the signal waveform, since any periodic signal can be represented by a Fourier series.

If these conditions are met, every two-port can be fully described in the frequency domain by two input quantities, two output quantities, and two linear equations. A detailed treatment of two-port theory can be found in [67, 32], and a concise summary in [46].

Depending on which quantities are chosen as inputs and outputs, different representations can be derived. This thesis uses the impedance matrix ($\mathcal{Z}$) and the chain matrix ($\mathcal{A}$). The advantage of the chain matrix is that the matrix of a cascade of networks is simply the product of the individual matrices [32]. The impedance matrix, on the other hand, is often more intuitive and has the same form as the familiar transformer equations.

Figure B.1 shows a general two-port with the reference directions of voltages and currents chosen here. The bold type indicates that the quantities are described by complex amplitudes. Unlike the usual practice in communications engineering, the passive (load) sign convention is used at port 1 and the active (generator) sign convention at port 2. In power electronics, this convention simplifies the interconnection of several two-ports, and the current directions shown usually coincide with the physical direction of power flow.

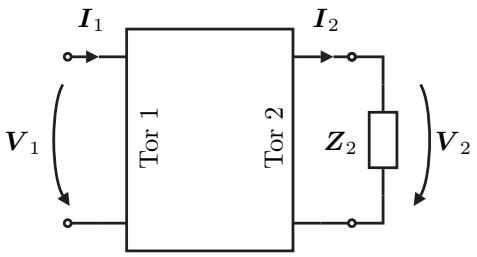

Figure B.1.: *Reference directions for the loaded two-port*

Because of this convention, the transfer functions and the conversions between representations differ from those in the cited literature [46, 32, 67].

For a system described by an impedance matrix, the system of equations

$$\begin{bmatrix} \boldsymbol{V}_1 \\ \boldsymbol{V}_2 \end{bmatrix} = \underbrace{\begin{bmatrix} \boldsymbol{z}_{1,1} & \boldsymbol{z}_{1,2} \\ \boldsymbol{z}_{2,1} & \boldsymbol{z}_{2,2} \end{bmatrix}}_{\text{Impedance matrix } \mathcal{Z}} \begin{bmatrix} \boldsymbol{I}_1 \\ \boldsymbol{I}_2 \end{bmatrix} . \tag{B.1}$$

applies. In chain-matrix form, (B.1) can be written equivalently as

$$\begin{bmatrix} \boldsymbol{V}_1 \\ \boldsymbol{I}_1 \end{bmatrix} = \underbrace{\begin{bmatrix} \boldsymbol{a}_{1,1} & \boldsymbol{a}_{1,2} \\ \boldsymbol{a}_{2,1} & \boldsymbol{a}_{2,2} \end{bmatrix}}_{\text{Chain matrix } \mathcal{A}} \begin{bmatrix} \boldsymbol{V}_2 \\ \boldsymbol{I}_2 \end{bmatrix} \tag{B.2}$$

The impedance matrix can be converted into a chain matrix by

$$\mathcal{A} = \begin{bmatrix} \boldsymbol{a}_{1,1} & \boldsymbol{a}_{1,2} \\ \boldsymbol{a}_{2,1} & \boldsymbol{a}_{2,2} \end{bmatrix} = \begin{bmatrix} \dfrac{\boldsymbol{z}_{1,1}}{\boldsymbol{z}_{2,1}} & -\dfrac{\det \mathcal{Z}}{\boldsymbol{z}_{2,1}} \\ \dfrac{1}{\boldsymbol{z}_{2,1}} & -\dfrac{\boldsymbol{z}_{2,2}}{\boldsymbol{z}_{2,1}} \end{bmatrix} \tag{B.3}$$

Conversely, the chain matrix is converted into an impedance matrix by

$$\mathcal{Z} = \begin{bmatrix} \boldsymbol{z}_{1,1} & \boldsymbol{z}_{1,2} \\ \boldsymbol{z}_{2,1} & \boldsymbol{z}_{2,2} \end{bmatrix} = \begin{bmatrix} \dfrac{\boldsymbol{a}_{1,1}}{\boldsymbol{a}_{2,1}} & -\dfrac{\det \mathcal{A}}{\boldsymbol{a}_{2,1}} \\ \dfrac{1}{\boldsymbol{a}_{2,1}} & -\dfrac{\boldsymbol{a}_{2,2}}{\boldsymbol{a}_{2,1}} \end{bmatrix} \tag{B.4}$$

With (B.1) and (B.2), the voltage transfer function according to Figure B.1 is

$$\boldsymbol{H}_v = \frac{\boldsymbol{Z}_2 \boldsymbol{z}_{2,1}}{\boldsymbol{Z}_2 \boldsymbol{z}_{1,1} - \det \mathcal{Z}} = \frac{\boldsymbol{Z}_2}{\boldsymbol{a}_{1,1} \boldsymbol{Z}_2 + \boldsymbol{a}_{1,2}} \tag{B.5}$$

and the current transfer function is

$$\boldsymbol{H}_i = \frac{\boldsymbol{I}_r}{\boldsymbol{I}_t} = \frac{\boldsymbol{z}_{2,1}}{\boldsymbol{Z}_2 - \boldsymbol{z}_{2,2}} = \frac{1}{\boldsymbol{a}_{2,1}\boldsymbol{Z}_2 + \boldsymbol{a}_{2,2}} \,. \tag{B.6}$$

The literature often also defines a power transfer function that relates the output apparent power S_2 to the input apparent power S_1. It is given by

$$\boldsymbol{H}_p = \frac{\boldsymbol{S}_2}{\boldsymbol{S}_1} = \boldsymbol{H}_v \boldsymbol{H}_i^* \,. \tag{B.7}$$

This requires the complex conjugate of the current transfer function. According to (B.6), the transfer impedance is given by

$$\boldsymbol{Z}_{tf} = \frac{\boldsymbol{V}_2}{\boldsymbol{I}_1} = \boldsymbol{H}_i \boldsymbol{Z}_2 = \frac{\boldsymbol{z}_{2,1}\boldsymbol{Z}_2}{\boldsymbol{Z}_2 - \boldsymbol{z}_{2,2}} = \frac{\boldsymbol{Z}_2}{\boldsymbol{a}_{2,1}\boldsymbol{Z}_2 + \boldsymbol{a}_{2,2}} \,. \tag{B.8}$$

Using (B.5), the transfer admittance can be determined as

$$\boldsymbol{Y}_{tf} = \frac{\boldsymbol{I}_2}{\boldsymbol{V}_1} = \boldsymbol{H}_v \frac{1}{\boldsymbol{Z}_2} = \frac{\boldsymbol{z}_{2,1}}{\boldsymbol{z}_{1,1}\boldsymbol{Z}_2 - \det\boldsymbol{\mathcal{Z}}} = \frac{1}{\boldsymbol{a}_{1,1}\boldsymbol{Z}_2 + \boldsymbol{a}_{1,2}} \tag{B.9}$$

Another characteristic quantity is the input impedance $\boldsymbol{Z}_1$. Like the transfer impedance and the transfer admittance, it can be determined from the voltage and current transfer functions:

$$\boldsymbol{Z}_1 = \frac{\boldsymbol{V}_1}{\boldsymbol{I}_1} = \frac{\boldsymbol{H}_i}{\boldsymbol{H}_v}\boldsymbol{Z}_2 = \frac{\boldsymbol{z}_{1,1}\boldsymbol{Z}_2 - \det\boldsymbol{\mathcal{Z}}}{\boldsymbol{Z}_2 - \boldsymbol{z}_{2,2}} = \frac{\boldsymbol{a}_{1,1}\boldsymbol{Z}_2 + \boldsymbol{a}_{1,2}}{\boldsymbol{a}_{2,1}\boldsymbol{Z}_2 + \boldsymbol{a}_{2,2}} \,. \tag{B.10}$$

The efficiency describes the ratio of output to input active power. With the load impedance $\boldsymbol{Z}_2$, it can be calculated using (B.6) and (B.10) by

$$\eta = \frac{|\boldsymbol{I}_2|^2 R_2}{|\boldsymbol{I}_1|^2 R_1} = |\boldsymbol{H}_i|^2 \frac{R_2}{R_1} \tag{B.11}$$

where, according to $\boldsymbol{Z} = R + jX$, R_1 and R_2 denote the real parts of $\boldsymbol{Z}_1$ and $\boldsymbol{Z}_2$, respectively.

The power factor is the ratio of active to apparent input power. Canceling the input current in this ratio gives, with (B.10),

$$\lambda = \frac{R_1}{|\boldsymbol{Z}_1|} \tag{B.12}$$

It characterizes the load seen by the source. A low power factor, for example, means that the source must be sized for a significant reactive current.

In a two-port, there is generally a coupling between the input and output ports. A coupling factor can be defined, which according to [68] is given by

$$\boldsymbol{k} = \sqrt{\frac{\boldsymbol{z}_{1,2}\boldsymbol{z}_{2,1}}{\boldsymbol{z}_{1,1}\boldsymbol{z}_{2,2}}} = \sqrt{1 - \frac{\boldsymbol{a}_{1,2}\boldsymbol{a}_{2,1}}{\boldsymbol{a}_{1,1}\boldsymbol{a}_{2,2}}} \tag{B.13}$$

Note again that the sign of the output current $\boldsymbol{I}_2$ is reversed compared with the usual convention in communications engineering, and that (B.3)–(B.10) are valid only in this case.

B.1. Measurement of the Two-Port Parameters

Several measurement methods exist. The method presented here generalizes one used in [32] to characterize lossless inductive coupling.

First, choose reference terminals for the input and output ports, i.e., label an upper and a lower terminal at each port. The equivalent circuit in Figure 3.2 shows that, with the output port open, an impedance of

$$\boldsymbol{Z}_{1_O} = \boldsymbol{Z}_{11} - \boldsymbol{Z}_{12} + \boldsymbol{Z}_{12} = \boldsymbol{Z}_{11} \tag{B.14}$$

can be measured at the input port. The same applies to the output port when the input port is open: the open-circuit impedance $\boldsymbol{Z}'_{2_O}$, and thus $\boldsymbol{Z}_{22}$, can be measured. These open-circuit measurements directly give two of the three impedances in the equivalent circuit of Figure 3.2.

The third impedance, $\boldsymbol{Z}_{12}$, can be determined by two further impedance measurements. For this purpose, one terminal of the input port is connected to one of the two terminals of the output port, and the impedance between the two remaining terminals is measured. This is illustrated in Figure B.2.

In the first case, Figure B.2(a), the net current through the impedance $\boldsymbol{Z}_{12}$ is zero. At the open terminals, the impedance

$$\boldsymbol{Z}_A = \boldsymbol{Z}_{11} + \boldsymbol{Z}_{22} - 2\boldsymbol{Z}_{12} \tag{B.15}$$

can be measured. In the second case, Figure B.2(b), the input current flows through the impedance $\boldsymbol{Z}_{12}$ twice, which doubles the voltage across this impedance. At the open terminals, an impedance of

$$\boldsymbol{Z}_B = \boldsymbol{Z}_{11} + \boldsymbol{Z}_{22} + 2\boldsymbol{Z}_{12} \tag{B.16}$$

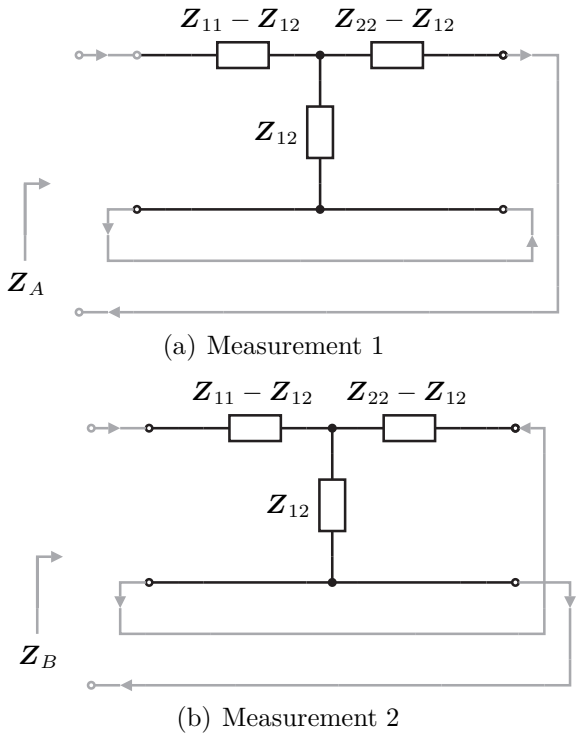

(a) Measurement 1

(b) Measurement 2

Figure B.2.: *Measurement of two impedances to determine* $\boldsymbol{Z}_{12}$

can be measured. Subtracting the two measurements (B.15) and (B.16) yields

$$\boldsymbol{Z}_{12} = \frac{\boldsymbol{Z}_B - \boldsymbol{Z}_A}{4} \tag{B.17}$$

If the two-port transfers power with an alternating quantity, the polarity of the output port is often of secondary importance. If it is not needed, a simpler method can be used: in addition to the two open-circuit measurements according to (B.14), a measurement of the input impedance with the output port short-circuited is sufficient. In this configuration, the input impedance is

$$\boldsymbol{Z}_{1_S} = \boldsymbol{Z}_{11} - \boldsymbol{Z}_{12} + \left(\frac{1}{\boldsymbol{Z}_{12}} + \frac{1}{\boldsymbol{Z}_{22} - \boldsymbol{Z}_{12}} \right)^{-1} . \tag{B.18}$$

From (B.14) and (B.18), the impedance $\boldsymbol{Z}_{12}$ can be derived. It is given by

$$\boldsymbol{Z}_{12} = \pm \sqrt{\boldsymbol{Z}_{2_O} \left(\boldsymbol{Z}_{1_O} - \boldsymbol{Z}_{1_S} \right)} . \tag{B.19}$$

With this simplified method, the sign of $\boldsymbol{Z}_{12}$ is unknown and must be chosen. Depending on the choice, the phase relationship between input and output ports may be off by π, which reflects the unknown polarity of the output port.

B.2. Synthesis of the Reciprocal System Matrix

If the system matrix is reciprocal [69], the relationship $\boldsymbol{z}_{1,2} = -\boldsymbol{z}_{2,1}$ holds for (B.1). A reciprocal system is therefore fully described by three impedances. This section shows how a practical network with identical terminal behavior can be derived from a known impedance matrix $\mathcal{Z}_{12}$ or chain matrix $\mathcal{A}_{12}$. This is shown for a T network and a Π network, each consisting of three impedances.

B.2.1. T Network

The T network is shown in Figure B.3. According to [46], its chain matrix is

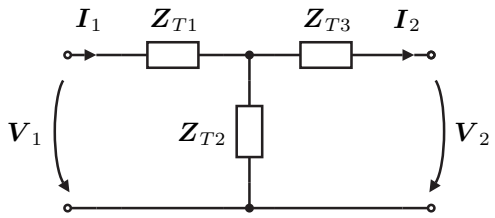

Figure B.3.: *General T network*

$$\mathcal{A}_T = \begin{bmatrix} 1 + \dfrac{\boldsymbol{Z}_{T1}}{\boldsymbol{Z}_{T2}} & \boldsymbol{Z}_{T1} + \boldsymbol{Z}_{T3} + \dfrac{\boldsymbol{Z}_{T1}\boldsymbol{Z}_{T3}}{\boldsymbol{Z}_{T2}} \\ \dfrac{1}{\boldsymbol{Z}_{T2}} & 1 + \dfrac{\boldsymbol{Z}_{T3}}{\boldsymbol{Z}_{T2}} \end{bmatrix}, \tag{B.20}$$

from which, by comparing coefficients with (B.2), the three impedances $\boldsymbol{Z}_{T1}$ to $\boldsymbol{Z}_{T3}$ can be determined directly as functions of a general chain matrix $\mathcal{A}$. For compactness, they are combined into a vector $\vec{\boldsymbol{Z}}_T$. Furthermore, using (B.3), the corresponding impedances can also be calculated as functions of an impedance matrix $\mathcal{Z}$. In summary,

$$\vec{\boldsymbol{Z}}_T = \begin{bmatrix} \boldsymbol{Z}_{T1} \\ \boldsymbol{Z}_{T2} \\ \boldsymbol{Z}_{T3} \end{bmatrix} = \frac{1}{\boldsymbol{a}_{2,1}} \begin{bmatrix} \boldsymbol{a}_{1,1} - 1 \\ 1 \\ \boldsymbol{a}_{2,2} - 1 \end{bmatrix} = \begin{bmatrix} \boldsymbol{z}_{1,1} + \boldsymbol{z}_{1,2} \\ -\boldsymbol{z}_{1,2} \\ \boldsymbol{z}_{1,2} - \boldsymbol{z}_{2,2} \end{bmatrix}. \tag{B.21}$$

B.2.2. Π Network

The Π network is shown in Figure B.4. According to [46], its chain matrix is

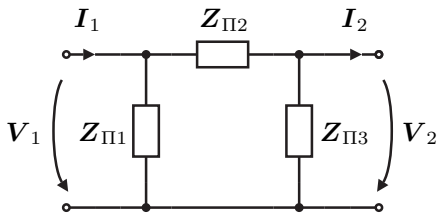

Figure B.4.: *General* Π *network*

$$\mathcal{A}_\Pi = \begin{bmatrix} 1 + \dfrac{\boldsymbol{Z}_{\Pi 2}}{\boldsymbol{Z}_{\Pi 3}} & \boldsymbol{Z}_{\Pi 2} \\ \dfrac{1}{\boldsymbol{Z}_{\Pi 1}} + \dfrac{1}{\boldsymbol{Z}_{\Pi 3}} + \dfrac{\boldsymbol{Z}_{\Pi 2}}{\boldsymbol{Z}_{\Pi 1}\boldsymbol{Z}_{\Pi 3}} & 1 + \dfrac{\boldsymbol{Z}_{\Pi 2}}{\boldsymbol{Z}_{\Pi 1}} \end{bmatrix} . \tag{B.22}$$

As in Section B.2.1, a vector can be given here that determines the impedances $\boldsymbol{Z}_{\Pi 1}$ to $\boldsymbol{Z}_{\Pi 3}$ from a known impedance or chain matrix:

$$\vec{\boldsymbol{Z}}_\Pi = \begin{bmatrix} \boldsymbol{Z}_{\Pi 1} \\ \boldsymbol{Z}_{\Pi 2} \\ \boldsymbol{Z}_{\Pi 3} \end{bmatrix} = \boldsymbol{a}_{1,2} \begin{bmatrix} \dfrac{1}{\boldsymbol{a}_{2,2} - 1} \\ 1 \\ \dfrac{1}{\boldsymbol{a}_{1,1} - 1} \end{bmatrix} = \det \mathcal{Z} \begin{bmatrix} \dfrac{1}{\boldsymbol{z}_{2,2} - \boldsymbol{z}_{1,2}} \\ \dfrac{1}{\boldsymbol{z}_{1,2}} \\ -\dfrac{1}{\boldsymbol{z}_{1,1} + \boldsymbol{z}_{1,2}} \end{bmatrix} . \tag{B.23}$$

With (B.23), the impedances of the Π network are known. In some cases, a direct conversion of the vector $\vec{\boldsymbol{Z}}_\Pi$ into the vector of the T network $\vec{\boldsymbol{Z}}_T$, or vice versa, is of interest. This is possible with

$$\vec{\boldsymbol{Z}}_\Pi = \boldsymbol{T}\vec{\boldsymbol{Z}}_T \tag{B.24}$$

$$\vec{\boldsymbol{Z}}_T = \boldsymbol{T}^{-1}\vec{\boldsymbol{Z}}_\Pi \tag{B.25}$$

where

$$\boldsymbol{T} = \boldsymbol{a}_{1,2}\boldsymbol{a}_{2,1} \begin{bmatrix} \dfrac{1}{(\boldsymbol{a}_{1,1}-1)(\boldsymbol{a}_{2,2}-1)} & 0 & 0 \\ 0 & 1 & 0 \\ 0 & 0 & \dfrac{1}{(\boldsymbol{a}_{1,1}-1)(\boldsymbol{a}_{2,2}-1)} \end{bmatrix}$$

$$= -\frac{\det \mathcal{Z}}{\boldsymbol{z}_{1,2}^2} \begin{bmatrix} \dfrac{1}{\left(\dfrac{\boldsymbol{z}_{1,1}}{\boldsymbol{z}_{1,2}}+1\right)\left(1-\dfrac{\boldsymbol{z}_{2,2}}{\boldsymbol{z}_{1,2}}\right)} & 0 & 0 \\ 0 & 1 & 0 \\ 0 & 0 & \dfrac{1}{\left(\dfrac{\boldsymbol{z}_{1,1}}{\boldsymbol{z}_{1,2}}+1\right)\left(1-\dfrac{\boldsymbol{z}_{2,2}}{\boldsymbol{z}_{1,2}}\right)} \end{bmatrix} \tag{B.26}$$

List of Figures

1.1 Nikola Tesla in front of a coil, photographer unknown (public domain), image source: *www. teslasociety. com* 11

2.1 Γ_1 equivalent circuit of the lossless transformer equations 16
2.2 Normalized magnitude of the input apparent power (2.4) as a function of the coupling factor k_X and the normalized load resistance 17
2.3 Example resonant circuitry of the lossless transmission system 18
2.4 Further example resonant circuitry of the lossless transmission system . 20
2.5 Normalized magnitude of the voltage transfer function, plotted versus normalized frequency 20

3.1 Transmission system as a two-port loaded by the impedance Z_r 22
3.2 T impedance model 24
3.3 Loaded T impedance model 24
3.4 Efficiency versus transfer quality factor 29
3.5 Efficiency of two different transmission systems according to (3.14), plotted versus the variable real part of the load impedance Z_r 30
3.6 Maximum efficiency and efficiency at the band limit, plotted versus the transfer quality factor 32
3.7 Voltage source with series reactance 35
3.8 Current source with parallel reactance 36
3.9 T impedance model extended by an ideal transformer 37
3.10 Transformer with complex turns ratio 38
3.11 Relationship between input and output apparent power of the complex transformer 39
3.12 Equivalent circuits of the impedance model with complex transformer . 41
3.13 Comparison of ideal gyrator and complex gyrator 43
3.14 Equivalent circuit of the transmission system from the Z parameters (3.3) using the complex gyrator 45
3.15 Equivalent circuit of the transmission system according to Figure 3.14(a) with $R_{tr} = 0$, the load reactance $X_r = X_{r,\eta}$ according to (3.13), and the source reactance $X'_t = -X_t$ according to (3.51) 45
3.16 Application example for the inductive transmission system A.1 46
3.17 Application example for the capacitive transmission system A.2 47

3.18 Transmission system with four coupled coils, own illustration, adapted from [31] . . . 48
3.19 Circuit diagram of the transmission system with four coupled coils . . . 49
3.20 Optimized transmission system with 2 coupled coils . . . 50

4.1 Matching of source and load to an existing transmission system . . . 51
4.2 Voltage-fed transmission system, load impedance as series connection (3.21) . . . 53
4.3 Voltage-fed transmission system, load impedance as parallel connection (3.22) . . . 55
4.4 Current-fed transmission system, load impedance as series connection (3.21) . . . 56
4.5 Current-fed transmission system, load impedance as parallel connection (3.22) . . . 56
4.6 Matching the load to the given transmission system . . . 57
4.7 Network for transformer-based series load matching . . . 58
4.8 Load matching with a Π network . . . 59
4.9 Network for gyrator-based series load matching . . . 60
4.10 Load matching with a T network . . . 61
4.11 Network for transformer-based parallel load matching . . . 62
4.12 Network for gyrator-based parallel load matching . . . 63
4.13 Matching the source to the given transmission system . . . 65
4.14 Transformer-based voltage feed . . . 65
4.15 Source matching with a Π network . . . 66
4.16 Gyrator-based voltage feed . . . 67
4.17 Source matching with a T network . . . 68
4.18 Transformer-based current feed . . . 69
4.19 Gyrator-based current feed . . . 70
4.20 Shift of the efficiency curve caused by load matching, plotted versus a variable real part of the load impedance . . . 73
4.21 Application example of transmission system matching . . . 74
4.22 Application example of gyrator-based parallel load matching for the capacitive example system . . . 76
4.23 Application example of gyrator-based parallel load matching for the inductive example system . . . 76
4.24 Application example of transformer-based voltage feed for the capacitive example system . . . 78
4.25 Application example of gyrator-based current feed for the inductive example system . . . 79
4.26 Four-coil transmission system, own illustration, adapted from [31] . . . 79
4.27 Inductive model of the simplified transformer equations (4.72) . . . 80
4.28 Synthesis of the complex gyrator as a T network . . . 81

4.29 Transmission system with four coupled inductances (Figure 3.19) represented by three complex gyrators . . . 81

5.1 Possible control model . . . 84

A.1 Example systems for inductive and capacitive near-field coupling . . . 87
A.2 Example system for inductive coupling . . . 88
A.3 Conductor loop . . . 89
A.4 Calculation of the magnetic flux density using the Biot-Savart law in the r-φ plane . . . 90
A.5 Normalized vector field of a current-carrying conductor loop according to Biot-Savart . . . 92
A.6 Two magnetically coupled conductor loops . . . 95
A.7 Coupling factor $k_{X_{rt}}$ between two identical conductor loops versus axial distance g . . . 95
A.8 Example system for capacitive coupling . . . 101
A.9 First model of the capacitive coupling . . . 102
A.10 Position of the coupling capacitor C_{c_1} . . . 102
A.11 Difficult-to-analyze original geometry and its simplified mapping . . . 103
A.12 Equipotential bodies in different dielectrics . . . 104
A.13 Position of the upper surface leakage capacitor and combination . . . 105
A.14 Field plot of the surface leakage capacitor . . . 106
A.15 Integration over the electrode area . . . 108
A.16 Position of the lateral leakage capacitor and chosen approximation . . . 109
A.17 Approximation of the lateral leakage capacitor by two right-angled electrodes, shown in the $\boldsymbol{z}$ plane . . . 110
A.18 Placement of the polygon angles on the t axis . . . 110
A.19 Field plot of the lateral leakage capacitor . . . 112
A.20 Correspondence of the vertices in $\boldsymbol{z}$ to the $\boldsymbol{w}$ plane . . . 113
A.21 Lossless equivalent circuit of the capacitive coupling . . . 115
A.22 Π model of the capacitive coupling . . . 115

B.1 Reference directions for the loaded two-port . . . 118
B.2 Measurement of two impedances to determine $\boldsymbol{Z}_{12}$ . . . 121
B.3 General T network . . . 122
B.4 General Π network . . . 123

Bibliography

[1] Stephan M. Günther. *Wissenschaftler und Ethik - Thomas A. Edison & Nikola Tesla*. Seminar - Wissenschaftler und Ethik. Technische Universität München, 2009.

[2] Fritz Fraunberger. *Illustrierte Geschichte der Elektrizität*. Aulis Verlag Deubner & Co. KG, Prisma Verlag GmbH, 1985.

[3] Nikola Tesla. "System of transmission of electrical energy." Pat. US645576A. 1900.

[4] Nikola Tesla. "Art of transmitting electrical energy through the natural mediums." Pat. US787412. 1905.

[5] Jane Alcorn et al. "Nikola Tesla - Forgotten genius of electricity and his historical wardenclyffe laboratory." In: *Tesla Conference 2011 - Exploring Tesla's Technologies*. 2011.

[6] Jaime Garnica, Raul A. Chinga, and Lin Jenshan. "Wireless Power Transmission: From Far Field to Near Field." In: *Proceedings of the IEEE* 99 (2013), pp. 1–11.

[7] Tobias Häuser. *Geschichte der Herzschrittmachertherapie*. St. Jude Medical GmbH. 2008. URL: http://www.sjm.de/50-jahre-herzschrittmacher/aktionen.html (visited on 09/14/2013).

[8] Farouk Balouchi and Bob Gohn. *Research Report, Executive Summary: Wireless Power*. 2012.

[9] Warren L. Stutzman and Gary A. Thiele. *Antenna Theory and Design*. John Wiley & Sons, Inc., 2013.

[10] William C. Brown. "The History of Power Transmission by Radio Waves." In: *IEEE Transactions of Microwave Theory and Techniques* 32 (1984), pp. 1230–1242.

[11] Maurice G. L. Roes et al. "Acoustic Energy Transfer: A Review." In: *IEEE Transactions on Industrial Electronics* 60 (2013), pp. 242–248.

[12] Dryden Flight Research Center. *Beamed Laser Power For UAVs*. NASA - National Aeronautics and Space Administration. 2005. URL: http://www.nasa.gov/centers/dryden/pdf/120329main_FS-087-DFRC.pdf (visited on 09/14/2013).

[13] Thomas J. Nugent and Jordin T. Kare. *Laser Power for UAVs*. LaserMotive, LLC. 2010. URL: http://lasermotive.com/products/uav-power-links/ (visited on 09/14/2013).

[14] Thomas J. Nugent and Jordin T. Kare. "Laser power beaming for defense and security applications." In: *Unmanned Systems Technology XIII* 8045 (2011).

[15] Peter E. Glaser. "Method and Apparatus for Converting Solar Radiation to Electrical Power." Pat. US3781647. 1973.

[16] Takanori Narita et al. "The Development of Space Solar Power System Technologies." In: *Mitsubishi Heavy Industries Technical Review* 48 (2011), pp. 17–22. URL: http://www.mhi.co.jp/technology/review/pdf/e484/e484017.pdf (visited on 09/14/2013).

[17] Martin Buchholz et al. "RFID - Flächendeckende Lokalisierung von Objekten im Medizin- und Pflegeumfeld." In: *ISIS AutoID / RFID Special* 1-2011 (2011).

[18] Chao Liu and Aiguo Patrick Hu. "Steady State Analysis of a Capacitively Coupled Contactless Power Transfer System." In: *Energy Conversion Congress and Exposition* 2009 (2009), pp. 3233–3238.

[19] Chao Liu, Aiguo Patrick Hu, and Mickel Budhia. "A Generalized Coupling Model for Capacitive Power Transfer Systems." In: *IECON 2010 - Annual Conference on IEEE Industrial Electronics Society* 36 (2010), pp. 274–279.

[20] Nick de N. Donaldson and T. A. Perkins. "Analysis of resonant coupled coils in the design of radio frequency transcutaneous links." In: *Medical & Biological Engineering & Computing* 21 (1983), pp. 612–627.

[21] E. Abel and S.M. Third. "Contactless power transfer - An exercise in topology." In: *IEEE Transactions on Magnetics* 20 (1984), pp. 1813–1815.

[22] Dominik Huwig. "Inductively Coupled Power Transfer - Kontaktloser Leistungstransfer und synchrone Informationsübertragung zwischen Systemen schwacher induktiver Kopplung." Diplom (FH). Hochschule für Technik und Wirtschaft des Saarlandes, 2007.

[23] Stephan Horras. "Standardisierung induktiver Energieübertragung." In: *Elektronik wireless power congress* 2 (2013), pp. 49–50.

[24] Yoon Goo Kim and Sangwook Nam. "Analysis of Wireless Power Transfer Using Spherical Modes." In: *International Workshop on Antenna Technology* 8 (2012), pp. 165–168.

[25] Meysam Zargham and P. Glenn Gulak. “Maximum Achievable Efficiency in Near-Field Coupled Power-Transfer Systems.” In: *Transactions on Biomedical Circuits and Systems* 6 (2012), pp. 228–245.

[26] Rui-Feng Xue, Kuang-Wei Cheng, and Minkyu Je. “High-Efficiency Wireless Power Transfer for Biomedical Implants by Optimal Resonant Load Transformation.” In: *IEEE Transactions on Circuits and Systems I:* 60 (2013), pp. 867–874.

[27] E. Bou, E. Alarcon, and J. Gutierrez. “A Comparison of Analytical Models for Resonant Inductive Coupling Wireless Power Transfer.” In: *Electromagnetics Research Symposium Proceedings* 2012 (2012), pp. 689–693.

[28] Mehdi Kiani and Maysam Ghovanloo. “The Circuit Theory Behind Coupled-Mode Magnetic Resonance-Based Wireless Power Transmission.” In: *IEEE Transactions on Circuits and Systems* 59 (2012), pp. 2065–2074.

[29] Hermann A. Haus and Weiping Huang. “Coupled-Mode Theory.” In: *Proceedings of the IEEE* 79 (1991), pp. 1505–1518.

[30] Aristeidis Karalis, J.D. Joannopoulos, and Marin Soljačić. “Efficient wireless non-radiative mid-range energy transfer.” In: *Annals of Physics* 323 (2008), pp. 34–48.

[31] André Kurs. “Power Transfer Through Strongly Coupled Resonances.” Master of Science on Physics. Massachusetts Institute of Technology, 2007.

[32] Horst Wupper. *Elektronische Schaltungen 1 - Grundlagen, Analyse, Aufbau*. Springer Verlag, 1996.

[33] Richard Feldtkeller. *Theorie der Spulen und Übertrager*. S. Hirzel Verlag Stuttgart, 1971.

[34] Oskar H. Stielau and Grant Anthony Covic. “Design of loosely coupled inductive power transfer systems.” In: *International Conference on Power System Technology - POWERCON* 1 (2000), pp. 85–90.

[35] Chwei-Sen Wang, Grant Anthony Covic, and Oskar H. Stielau. “Power Transfer Capability and Bifurcation Phenomena of Loosely Coupled Inductive Power Transfer Systems.” In: *IEEE Transactions on Industrial Electronics* 51 (2004), pp. 148–157.

[36] Zhou Wenqi and Ma Hao. “Design Considerations of Compensation Topologies in ICPT System.” In: *Applied Power Electronics Conference - APEC* (2007), pp. 985–990.

[37] Robert W. Erickson and Dragan Maksimović. *Fundamentals of Power Electronics*. Vol. 2. Kluwer Academic publishers, 2004.

[38] Daniel Kürschner and Christian Rathge. "Contactless Energy Transmission Systems with Improved Coil Positioning Flexibility for High Power Applications." In: *Power Electronics Specialists Conference* 13 (2008), pp. 4326–4332.

[39] Jürgen Biela and Johann Walter Kolar. "Electromagnetic Integration of High Power Resonant Circuits Comprising High Leakage Inductance Transformers." In: *Power Electronics Specialists Conference* 35 (2004), pp. 4537–4545.

[40] Douglas C. Galbraith, Mani Soma, and Robert L. White. "A Wide-Band Efficient Inductive Transdermal Power and Data Link with Coupling Insensitive Gain." In: *Transactions on Biomedical Engineering* BME-34 (1987), pp. 265–275.

[41] Peter Wambsganß and Dominik Huwig. "Inductive power transmission system with stabilized output voltage using local primary-and secondary-side control." In: *Power Electronics and Motion Control Conference* 14 (2010), S15/1–S15/8.

[42] Jeroen de Boeij et al. "Contactless power supply for moving sensors and actuators in high-precision mechatronic systems with long-stroke power transfer capability in x-y plane." In: *Sensors and Actuators A: Physical* 148 (2008), pp. 319–328.

[43] Artur J. Moradewicz and Marian P. Kazmierkowski. "Resonant Converter Based Contactless Power Supply for Robots and Manipulators." In: *Journal of Automation, Mobile Robotics & Intelligent Systems* 2 (2008), pp. 20–25.

[44] Karl Küpfmüller, Wolfgang Mathis, and Albrecht Reibiger. *Theoretische Elektrotechnik - Eine Einführung*. Springer Verlag, 2005.

[45] Richard Feldtkeller. *Monographien der elektrischen Nachrichtentechnik, Band 2, Einführung in die Vierpoltheorie*. S. Hirzel Verlag Stuttgart, 1962.

[46] Gerhard Krucker. "Analoge Systeme 1 (ELA4) - 3. Netzwerke." In: Krucker Engineering - http://www.krucker.ch/, 2004. Chap. Netzwerke.

[47] Eberhard Waffenschmidt and Toine Staring. "Limitation of inductive power transfer for consumer applications." In: *European Conference on Power Electronics and Applications (EPE)* 13 (2009), pp. 1–10.

[48] Eberhard Waffenschmidt. "Wireless Power for Mobile Devices." In: *IEEE Telecommunications Energy Conference (INTELEC)* 33 (2011), pp. 1–9.

[49] Kamil A. Grajski, Ryan Tseng, and Chuck Wheatley. "Loosely-coupled wireless power transfer: Physics, circuits, standards." In: *IEEE International Memory Workshop* 2012 (2012), pp. 9–14.

[50] Bernard D.H. Tellegen. "The Gyrator, a new electric network element." In: *Philips Research Report* 3 (1948), pp. 81–101.

[51] Jin Huh et al. “Characterization of Novel Inductive Power Transfer Systems for On-Line Electric Vehicles.” In: *Applied Power Electronics Conference and Exposition (APEC)* 26 (2011), pp. 1975–1979.

[52] Anil Kumar RamRakhyani, Shahriar Mirabbasi, and Mu Chiao. “Design and optimization of resonance-based efficiency wireless power delivery systems for biomedical implants.” In: *IEEE Transactions on biomedical circuits and systems, Vol 5, No. 1*. IEEE. 2011.

[53] André Kurs et al. “Wireless Power Transfer via Strongly Coupled Magnetic Resonances.” In: *Science* 317 (2007), pp. 83–86.

[54] Chunbo Zhu et al. “Simulation and experimental analysis on wireless energy transfer based on magnetic resonances.” In: *Vehicle Power and Propulsion IEEE Conference - VPPC* 4 (2008), pp. 1–4.

[55] Dominik Huwig. “Verlustfreie Gleichrichtermodulation - Eingangsimpedanzmodulation am aktiven Brückengleichrichter zur unidirektionalen Datenübertragung in induktiv gekoppelten Systemen.” In: *Seminar: Elektrische Schaltungen*. FernUniversität Hagen, 2010.

[56] Eberhard Herter and Wolfgang Lörcher. *Nachrichtentechnik - Übertragung - Vermittlung - Verarbeitung*. Ed. by Walter Röcker. Carl Hanser Verlag GmbH & CO. KG, 2004.

[57] Otfried Georg. *Elektromagnetische Felder und Netzwerke - Anwendungen in Mathcad und PSpice*. Springer Verlag, 1999.

[58] Horst Stöcker. *Taschenbuch mathematischer Formeln und moderner Verfahren*. 4th ed. Verlag Harri Deutsch, 2003.

[59] Klaus Finkenzeller. *RFID Handbuch - Grundlagen und praktische Anwendungen von Transpondern, kontaktlosen Chipkarten und NFC*. 5th ed. Carl Hanser Verlag GmbH & CO. KG, 2008.

[60] Horst Stöcker. *Taschenbuch der Physik*. 5th ed. Verlag Harri Deutsch, 2004.

[61] Romanus Dyczij-Edlinger. “Handschriftliche Verfassung zur Kapazitätsberechnung mittels konformer Abbildung.” Theoretische Betrachtung sowie messtechnische Bewertung des vorgestellten kapazitiven Beispielsystems. Im Rahmen einer Zusammenarbeit von Prof. Dr. Romanus Dyczij-Edlinger erstellt. 2012.

[62] Hans Walser. *Konforme Abbildungen*. Eidgenössische Technische Hochschule (ETH) Zürich. Feb. 2002.

[63] Gottlieb Strassacker and Peter Strassacker. *Analytische und numerische Methoden der Feldberechnung*. 1st ed. B.G. Teubner Verlag, 1993.

[64] Gottlieb Strassacker and Roland Süße. *Rotation, Divergenz und Gradient - Einführung in die elektromagnetische Feldtheorie*. 6th ed. B.G. Teubner Verlag, 2006.

[65] Heino Henke. *Elektromagnetische Felder*. 3rd ed. Springer Verlag, 2007.

[66] Hua-Min Li et al. "Frequency and Temperature Dependence of the Dielectric Properties of a PCB Substrate for Advanced Packaging Applications." In: *Journal of the Korean Physical Society* 54.3 (2009), pp. 1096–1099.

[67] Wilfried Weißgerber. *Elektrotechnik für Ingenieure - Band 3 - Ausgleichsvorgänge, Fourieranalyse, Vierpoltheorie*. Friedrich Vieweg & Sohn Verlag, 2007.

[68] Frederick Emmons Terman. *Radio Engineering*. McGraw-Hill, 1954.

[69] Jörg Grabow. "Mechatronische Netzwerke." In: Ernst-Abbe-Fachhochschule Jena, 2011. Chap. Besondere Eigenschaften - Reziprozität.